

SUNFEST 2015

Summer Undergraduate Fellowships in Sensor Technologies

<http://www.seas.upenn.edu/sunfest/>



TECHNICAL REPORT
TR-CST AUG 2015
Center for Sensor Technologies
University of Pennsylvania
Philadelphia, PA 19104

Acknowledgement

This material is based upon work supported by the National Science Foundation under Grant No. 1359107.

Disclaimer

Any opinions, findings, and conclusions or recommendations expressed in this material are those of the author(s) and do not necessarily reflect the views of the National Science Foundation.



SUNFEST 2015
**SUMMER UNDERGRADUATE FELLOWSHIP IN SENSOR
TECHNOLOGIES**

Sponsored by the National Science Foundation (Award no. 1062672)

From May 30 through August 8, 2015 ten students participated in the SUNFEST program, which is organized by the Center for Sensor Technologies of the School of Engineering and Applied Science at the University of Pennsylvania. This unique “Summer Experience for Undergraduates in Sensor Technologies” program was initiated in 1986 and has grown considerably in size. It is now recognized as one of the most successful summer programs for undergraduates in the country. I would like to express my sincere gratitude to the National Science Foundation for their continued support since 1987 for this REU Site.

The purpose of the SUNFEST program is to provide bright, motivated undergraduate students with the opportunity to become involved in active research projects under the supervision of a faculty member and his graduate student(s). The general area of research concentrates on sensor technologies and includes projects such as materials and technology for sensors, nanotechnology and microstructures, smart imagers, sensors for biomedical applications and robotics. By providing the students with hands-on experience and integrating them with a larger research group where they can work together with other students, the program intends to guide them in their career choices. By exposing the students to the world of research, we hope they will be more inclined to go on for advanced degrees in science and engineering, as many have done.

The students participated in a variety of hands-on workshops in order to give them the tools to do first-rate research or enhance their communication skills. These included “Ethics in Science and Engineering”, “Information Retrieval and Evaluation”, “Applying to Graduate School”, “Poster Presentations”, and “Writing Technical Reports”. Students also had plenty of opportunity for social interactions among themselves or with faculty and graduate student advisors.

As we did last year, group of judges selected the top project and two honorable mentions. The projects were selected based on the technical quality of the results, the quality of the poster and the slide presentation, and answering questions. The choices were very hard since all projects were excellent. The first prize went to Samantha Burns for her project, "Preparation of a Mechanochromic System using Liquid Crystal Dispersed in Polymer" under the supervision of Professor Shu Yang. The two honorable mentions went to Tim Linscott for his project, "Cross-CUT Interference Present in Timing Extraction" with Professor Andre DeHon; and to Eleanor Tursman for her project, "Geometric Stereo Increases Accuracy of Depth Estimations for an Unmanned Air Vehicle with a Small Baseline Stereo System" under the supervision of Camillo J. Taylor.

This booklet contains reports from this year’s projects, the quality of which testifies to the high level of research and commitment by these students and their supervisors. I would like to express my sincere thanks to the students for their enthusiastic participation; the help of the faculty members, graduate students and support staff is very much appreciated. I would also like to thank Colleen Kennedy, Joshua Taton, Sid Deliwala, Jessica Leon, Douglas McGee, Lilian Wu, Susan Margulies and the ESE staff for their invaluable help in making this program run smoothly.

Jan Van der Spiegel, Director

FINAL REPORT

2015 SUMMER UNDERGRADUATE FELLOWSHIP IN SENSOR TECHNOLOGIES

Sponsored by the National Science Foundation

<http://www.seas.upenn.edu/sunfest/alumni-projects-15.php>

TABLE OF CONTENTS

LIST OF STUDENT PARTICIPANTS

Caffe Framework on the Jetson TK1: Using Deep Learning for Real Time Object Detection	1-3
<i>Christopher Alicea-Nieves (Computer Engineering) – University of Puerto Rico</i> <i>Advisor: Dr. Camillo J. Taylor</i>	
Preparation of a Mechanochromic System using Liquid Crystal Dispersed in Polymer	4-7
<i>Samantha Burns (Materials Science) – University of Pennsylvania</i> <i>Advisor: Dr. Shu Yang</i>	
Exercising <i>Caenorhabditis elegans</i>	8-11
<i>Hannah Corcos (Mechanical Engineering) – University of Maryland</i> <i>Advisor: Dr. Haim Bau</i>	
Watts App: An Energy Analytics and Demand-Response Advisor Tool	12-17
<i>Jennifer Santiago Gonzalez (Electrical Engineering) – Case Western Reserve University</i> <i>Advisors: Dr. Rahul Mangharam</i>	
Hearing Loss: Piezo-polymers Nano-fibers for Bio-medical Applications	18-29
<i>Jamie Mario Gutierrez (Physics) – North Park University</i> <i>Advisor: Dr. Jorge Santiago</i>	
Graphene-Boron Nitride Heterostructures: A platform for the synthesis of the nanotransistor	30-40
<i>Alexander Hunt IV (Materials Science) – University of Pennsylvania</i> <i>Advisor: Dr. A.T. Charlie Johnson</i>	
Design of a Wireless Power Transfer System for Wireless Sensor Networks in Biomedical Applications	41-45
<i>Timothy Kindervatter (Electrical Engineering) – College of New Jersey</i> <i>Advisor: Dr. Jan Van der Spiegel, Milin Zhang</i>	
Cross-CUT Interference Present in Timing Extraction	46-50
<i>Timothy Linscott (Electrical Engineering) – Seattle University</i> <i>Advisor: Dr. Andre DeHon</i>	

Photo-Actuation: Determining the Effect of Blue Light on the Actuation of Micro-Beads by Serratia <i>Erica Sadler (Bio-Engineering) – Cornell University</i> <i>Advisors: Dr. Vijay Kumar</i>	51-54
Geometric Stereo Increases Accuracy of Depth Estimations for an Unmanned A Vehicle with a Small Baseline Stereo System <i>Eleanor Tursman (Physics) – Grinnell College</i> <i>Advisor: Dr. Camillo J. Taylor</i>	55-61
Piezoelectric Polyvinylidene Fluoride Nanofibers <i>Jerrell Walker (Electrical Engineering) – University of Pennsylvania</i> <i>Advisor: Dr. Jorge Santiago</i>	62-66

**LIST OF STUDENT PARTICIPANTS
IN THE SUNFEST PROGRAM SINCE 1986**

Summer 2015

Christopher Alicea-Nieves	University of Puerto Rico
Samantha Burns (Winner, Best Presentation & Poster Award)	University of Pennsylvania
Hannah Corcos	University of Maryland
Santiago Gonazalez	Case Western Reserve University
Mario Gutierrez	North Park University
Alexander Hunt IV	University of Pennsylvania
Timothy Kindervatter	College of New Jersey
Timothy Linscott (Honorable Mention)	Seattle University
Erica Sadler	Cornell University
Eleanor Tursman (Honorable Mention)	Grinnell College
Jerrell Walker	University of Pennsylvania

Summer 2014

Justin Aird	Hampton College
Porscha Baines	Lincoln University
Antonio Basukoski	Columbia University
Jennifer Bourlier	University of Michigan at Dearborn
Jamie Johnson (Honorable Mention)	Broward College
Marcus Pan (Honorable Mention)	University of Pennsylvania
Golden Rockefeller	University of Delaware
Abel Rodriguez	The George Washington University
Jacob Sacks (Winner, Best Presentation & Poster Award)	The University of Texas at Austin
Jordan White	Hampton College

Summer 2013

George Chen (Winner, Best Presentation & Poster Award)	Johns Hopkins University
Cedric Destin	Temple University
Rodolfo Finocchi	Johns Hopkins University
Ty'Quish Keyes	Morehouse College
Andrew Knight	Norfolk State University
Samantha Muñoz	Vanderbilt University
Gedeon Nyengele (Honorable Mention)	Georgia Perimeter College
Quentin Morales-Perryman	Hampton University
Gabriela Romero (Honorable Mention)	Worcester Polytechnic Institute
Basheer Subei	University of Illinois at Chicago

Summer 2012

Larry Jason Allen	University of the District of Columbia
Karl Bayer	Columbia University
Thomas Belatti	Villanova University
Carlos Biao (Winner, Best Presentation & Poster Award)	Prince George's County Community College
Matt Biggers	University of North Carolina
Stephanie Diaz	Birmingham University
Xavier Hanson-Lerma	University of Florida
Sezan Hessou	Penn State University
William Marshall (Honorable Mention)	Lehigh University
Blake McMillian	Hampton University
Ugonna Ohiri	University of Maryland
Anish Raghavan	Trinity College Dublin
Megan Schmidt (Honorable Mention)	University of Missouri

Summer 2011

Adeboye A. Adejare Jr.	University of the Sciences in Philadelphia
Jason Allen	University of the District of Columbia
Crystal Batts	Winston-Salem University
Matthew Hale	University of Pennsylvania
Syrena Huynh (Honorable Mention)	North Carolina State University
Monroe Kennedy	University of Maryland
Nyeemah Kennedy	Pennsylvania State University
Adam Lowery	Cornell University
Peter Malamas	John Hopkins University
Piyush Poddar (Honorable Mention)	John Hopkins University
Daniel J. Preston (Winner, Best Presentation Award)	The University of Alabama
James Reszczenski	Virginia Polytechnic Institute and State University
Ziwei Zhong	Purdue University

Summer 2010

Jason C. Carter	Morgan State University
Carlos Torres Casiano	University of Puerto Rico, at Mayagüez
Nathalia Garcia Acosta (Honorable Mention)	Temple University
Brian Helfer (Winner, Best Project & Presentation Award)	University of Connecticut
Sarena Horava	University of Massachusetts Amherst
Brett Kuprel	University of Michigan
Logan Osgood-Jacobs (Honorable Mention)	Swarthmore College

Sriram Radkrishnan
Johary Rivera
Jennifer L. Smith
Noah Tovares

University of Pennsylvania
University of Puerto Rico, Río Piedras Campus
North Carolina State University
Occidental College

Hank Bink
Allison Connolly
Phillip Dupree
Katherine Gerasimowicz
Willie Gonzalez
Sarah Koehler
Linda McLaughlin
Ieva Narkeviciute
Jeffrey Perreira
Andrew Townley
Desiree Velazquez
Valerie Walters

Summer 2009

Lafayette College
Johns Hopkins University
Columbia University
University of Pennsylvania
Univ. of Puerto Rico, Mayaguez
Cornell University
Community College of Philadelphia
Univ. of Massachusetts Amherst
Lehigh University
University of Pennsylvania
Univ. of Puerto Rico at Humacao)
Virginia Polytechnic Institute and State
University

Summer 2008

Clarence Agbi
Uchenna Anyanwu
Christopher Baldassano
Alta Berger
Ramon Luis Figueroa
David Joffe
Erika Martinez
Alexei Matyushov
Kamruzzaman Rony
Anil Venkatesh
Emily Wible

Yale University
San Jose State University
Princeton University
George Washington University
University of Puerto Rico
Carnegie Mellon University
University of Puerto Rico
Arizona State University
Stony Brook University
University of Pennsylvania
University of Pennsylvania

Summer 2007

Mulutsga Bereketab
Sonia A. Bhaskar
Patrick Duggan
Nataliya Kilevskaya
Ryan Li
Viktor L. Orekhov
Andrew Potter
Pamela Tsing

Virginia Polytechnic Institute
Princeton University
Providence College
University of Florida
Case Western Reserve University
Tennessee Technological University
Brown University
University of Pennsylvania

Victor Uriarte
Adriane Wotawa-Bergen
Arellys Rosado Gomez

Florida International University
University at Buffalo
University of Puerto Rico

Summer 2006

Sam Burden
Jose M. Castillo Colon
Alexsandra Fridshtand
Shakera Guess
Journee Isip
Nathan Lazarus
Armand O'Donnell
William Peeples
Raúl Pérez Martínez
Helen Schwerdt
Xiaoning Yuan

University of Washington
University of Puerto Rico
Lehigh University
Lincoln University
Columbia University
University of Pennsylvania
University of Pennsylvania
Lincoln University
University of Puerto Rico
Johns Hopkins University
Duke University

Summer 2005

Robert Callan
David Cohen
Louie Huang
Roman Geykhman
An Nguyen
Olga Paley
Miguel Perez Tolentino
Ebenge Usip
Adam Wang
Kejia Wu

University of Pennsylvania
University of California at Berkeley
University of Puerto Rico
University of Southern California
University of Texas, Austin
University of Pennsylvania

Summer 2004

Benjamin Bau
Alexander H.Chang
Seth Charlip-Blumlein
Ling Dong
David Jamison
Dominique Low
Emmanuel U. Onyegam
J. Miguel Ortigosa
William Rivera
Matthew Saucedo
Olivia Tsai

Massachusetts Institute of Technology
University of Pennsylvania
University of Pennsylvania
University of Rochester
Johns Hopkins University
University of Pennsylvania
University of Texas, Dallas
Florida Atlantic University
University of Puerto Rico, Mayaguez
Texas A&M University, Kingsville
Carnegie Mellon University

Summer 2003

Emily Blem
Brian Corwin
Vinayak Deshpande
Nicole DiLello
Jennifer Geinzer
Jonathan Goulet
Mpitulo Kala-Lufulwabo
Emery Ku
Greg Kuperman
Linda Lamptey
Prasheel Lillaney
Enrique Rojas

Swarthmore College
University of Pennsylvania
University of Virginia
Princeton University
University of Pittsburgh
University of Pennsylvania
University of Pittsburgh
Swarthmore College
University of Pennsylvania
University of Pennsylvania
University of Pennsylvania
University of Pennsylvania

Summer 2002

Christopher Bremer
Aslan Ettehadien
April Harper
Catherine Lachance
Adrian Lau
Cynthia Moreno
Yao Hua Ooi
Amber Sallerson
Jiong Shen
Kamela Watson
John Zelena

Colorado School of Mines
Morgan State University
Hampton University
University of Pennsylvania
University of Pennsylvania
University of Miami
University of Pennsylvania
University of Maryland/Baltimore
University of California-Berkeley
Cornell University
Wilkes University

Summer 2001

Gregory Barlow
Yale Chang
Luo Chen
Karla Conn
Charisma Edwards
EunSik Kim
Mary Kutteruf
Vito Sabella
William Sacks
Santiago Serrano
Kiran Thadani
Dorci Lee Torres

North Carolina State University
University of Pennsylvania
University of Rochester
University of Kentucky
Clark Atlanta University
University of Pennsylvania
Bryn Mawr College
University of Pennsylvania
Williams College
Drexel University
University of Pennsylvania
University of Puerto Rico

Summer 2000

Lauren Berryman
Salme DeAnna Burns
Frederick Diaz
Hector Dimas
Xiomara Feliciano
Jason Gillman
Tamara Knutsen
Heather Marandola
Charlotte Martinez
Julie Neiling
Shiva Portonova

University of Pennsylvania
University of Pennsylvania
University of Pennsylvania (AMPS)
University of Pennsylvania (AMPS)
University of Turabo (Puerto Rico)
University of Pennsylvania
Harvard University
Swarthmore College
University of Pennsylvania
University of Evansville, Indiana
University of Pennsylvania

Summer 1999

David Auerbach
Darnel Degand
Hector E. Dimas
Ian Gelfand
Jason Gillman
Jolymar Gonzalez
Kapil Kedia
Patrick Lu
Catherine Reynoso
Philip Schwartz

Swarthmore College
University of Pennsylvania
University of Pennsylvania
University of Pennsylvania
University of Pennsylvania
University of Puerto Rico
University of Pennsylvania
Princeton University
Hampton University
University of Pennsylvania

Summer 1998

Tarem Ozair Ahmed
Jeffrey Berman
Alexis Diaz
Clara E. Dimas
David Friedman
Christin Lundgren
Heather Anne Lynch
Sancho Pinto
Andrew Utada
Edain (Eddie) Velazquez

Middlebury University
University of Pennsylvania
Turabo University, Puerto Rico
University of Pennsylvania
University of Pennsylvania
Bucknell University
Villanova University
University of Pennsylvania
Emory University
University of Pennsylvania

Summer 1997

Francis Chew
Gavin Haentjens
Ali Hussain
Timothy Moulton
Joseph Murray
O'Neil Palmer
Kelum Pinnaduwege

University of Pennsylvania
University of Pennsylvania
University of Pennsylvania
University of Pennsylvania
Oklahoma University
University of Pennsylvania
University of Pennsylvania

John Rieffel
Juan Carlos Saez

Swarthmore College
University of Puerto Rico, Cayey

Rachel Branson
Corinne Bright
Alison Davis
Rachel Green
George Koch
Sandro Molina
Brian Tyrrell
Joshua Vatsky
Eric Ward

Summer 1996

Lincoln University
Swarthmore College
Harvard University
Lincoln University
University of Pennsylvania
University of Puerto Rico-Cayey
University of Pennsylvania
University of Pennsylvania
Lincoln University

Maya Lynne Avent
Tyson S. Clark
Ryan Peter Di Sabella
Osvaldo L. Figueroa
Colleen P. Halfpenny
Brandeis Marquette
Andreas Olofsson
Benjamin A. Santos
Kwame Ulmer

Summer 1995

Lincoln University
Utah State University
University of Pittsburgh
University of Puerto Rico-Humacao
Georgetown University
Johns Hopkins
University of Pennsylvania
University of Puerto Rico-Mayaguez
Lincoln University

Alyssa Apsel
Everton Gibson
Jennifer Healy-McKinney
Peter Jacobs
Sang Yoon Lee
Paul Longo
Laura Sivitz
Zachary Walton

Summer 1994

Swarthmore College
Temple University
Widener University
Swarthmore College
University of Pennsylvania
University of Pennsylvania
Bryn Mawr College
Harvard University

Adam Cole
James Collins
Brandon Collings
Alex Garcia
Todd Kerner
Naomi Takahashi
Christopher Rothey
Michael Thompson
Kara Ko
David Williams

Summer 1993

Swarthmore College
University of Pennsylvania
Hamilton University
University of Puerto Rico
Haverford College
University of Pennsylvania
University of Pennsylvania
University of Pennsylvania
University of Pennsylvania
Cornell University

Vassil Shtonov

University of Pennsylvania

James Collins
Tabbatha Dobbins
Robert G. Hathaway
Jason Kinner
Brenelly Lozada
P. Mark Montana
Dominic Napolitano
Marie Rocelie Santiago

Summer 1992

University of Pennsylvania
Lincoln University
University of Pennsylvania
University of Pennsylvania
University of Puerto Rico
University of Pennsylvania
University of Pennsylvania
Cayey University College

Gwendolyn Baretto
Jaimie Castro
James Collins
Philip Chen
Sanath Fernando
Zaven Kalayjian
Patrick Montana
Mahesh Prakriya
Sean Slepner
Min Xiao

Summer 1991

Swarthmore College
University of Puerto Rico
University of Pennsylvania
Temple University
University of Pennsylvania
University of Pennsylvania

Angel Diaz
David Feenan
Jacques Ip Yam
Zaven Kalayjian
Jill Kawalec
Karl Kennedy
Jinsoo Kim
Colleen McCloskey
Faisal Mian
Elizabeth Penadés

Summer 1990

University of Puerto Rico
University of Pennsylvania
University of Pennsylvania
University of Pennsylvania
University of Pennsylvania
Geneva
University of Pennsylvania
Temple University
University of Pennsylvania
University of Pennsylvania

Peter Kinget
Chris Gerdes
Zuhair Khan
Reuven Meth
Steven Powell
Aldo Salzberg
Ari M. Solow
Arel Weisberg

Summer 1989

Katholiek University of Leuven
University of Pennsylvania
University of Pennsylvania
Temple University
University of Pennsylvania
University of Puerto Rico
University of Maryland
University of Pennsylvania

Jane Xin

University of Pennsylvania

Summer 1988

Lixin Cao
Adnan Choudhury
D. Alicea-Rosario
Chris Donham
Angela Lee
Donald Smith
Tracey Wolfsdorf
Chai Wah Wu
Lisa Jones

University of Pennsylvania
University of Pennsylvania
University of Puerto Rico
University of Pennsylvania
University of Pennsylvania
Geneva
Northwestern University
Lehigh University
University of Pennsylvania

Summer 1987

Salman Ahsan
Joseph Dao
Frank DiMeo
Brian Fletcher
Marc Loinaz
Rudy Rivera
Wolfram Urbanek
Philip Avelino
Lisa Jones

University of Pennsylvania
University of Puerto Rico
University of Pennsylvania
University of Pennsylvania
University of Pennsylvania

Summer 1986

Lisa Yost
Greg Kreider
Mark Helsel

University of Pennsylvania
University of Pennsylvania
University of Pennsylvania

Caffe Framework on the Jetson TK1: Using Deep Learning for Real Time Object Detection

Christopher Alicea-Nieves (University of Puerto Rico at Mayaguez, Computer Engineering,
SUNFEST Fellow)

Dr. Camillo J. Taylor, Computer and Information Science, University of Pennsylvania

Abstract— Deep Neural Networks are an approach to using state-of-the-art machine learning algorithms in order to improve the applications of the computer vision field. These neural networks are complex mathematical models which can be trained to identify certain objects within a frame, and some of them are also able to identify where on the image is the object that they identified. This technical report focuses on presenting the implementation of a deep neural network on a low-power embedded computer system, specifically the NVIDIA Jetson TK1, in order to run convolutions in real-time for object detection. This can be achieved by implementing Fast R-CNN—a state-of-the-art model for convolutions—in the machine learning framework called Caffe.

Index Terms—caffe; convolutions; Jetson; machine learning; neural networks.

I. INTRODUCTION

Computer vision is a field of computation that has experienced a steady growth of popularity over the past few years because of all the useful applications that have been and are being developed. From counting cars to recognizing people's faces, Computer vision is a powerful tool that has not yet reached its maximum potential. In the past few years, since the ImageNet Large Scale Visual Recognition Challenge 2012 (ILSVRC) [2], the integration of Deep Learning algorithms based on convolutions has been an increasingly popular approach for various tasks, like object detection and labeling. That has been a motivation for developing approaches that make use of Graphic Processing Units (GPUs), since they excel at running these computations. In order to achieve real-time implementation on our system, we must explore the most memory-efficient methods and train networks specifically for the tasks we wish to achieve. We are using the NVIDIA Jetson TK1 because it is a low-power system equipped with a dedicated GPU.

II. BACKGROUND

2.1 Deep Neural Networks

A Convolutional Neural Network is based on different layers that look for features in an image. Regions with Convolutional Neural Networks (R-CNN) [6] are a variation of the regular CNNs. They first analyze the frame and propose different regions for different objects, and then proceed to run the CNN on each separate region. This model is more accurate in the PASCAL VOC [3], which is another dataset challenge but for object detection, hence the reason why we will be using it. The region proposal process is very expensive; it is a computational bottleneck in running R-CNNs. Fast-Regions with Convolutional Networks (Fast R-CNNs) [7] are designed to avoid this bottleneck and speed up the process of running convolutions using this network architecture. Most of the pre-trained models are very big because they were trained for large-scale datasets, resulting in a slower performance for a real-time implementation. To achieve real-time performance, we will have to create our own model based on this architecture and train it on the specific categories that we will need.

2.2 Caffe Framework

Caffe [1] is a modular machine learning framework, which means that it is open source and modifiable. It provides access to state-of-the-art deep learning algorithms in order to develop, train, and test models. The framework is based on a convolutional architecture because it has been the leading state-of-the-art deep architecture for image processing. These Convolutional Neural Networks (CNNs) are being used to train models in order to detect objects and label them, besides other implementations like gender recognition and age estimation. One of the challenges with the use of these CNNs is that they require significant computational power. There are many approaches that use variations of the CNNs in order to achieve better performance. We will be exploring these approaches and implement them on the Jetson TK1.

2.3 The datasets

- **ImageNet Large Scale Visual Recognition Challenge (LSVRC)**

ImageNet [2] is a database of hundreds of thousands of pictures labeled in over a thousand categories. This challenge serves as a benchmark for testing different Deep Learning algorithms, especially those based on CNNs. The challenge is simple, ImageNet gives the company/researcher access to a set of 50,000 images used to train the model, and then that model is deployed to analyze and label 1.2 million images that it has never seen before. The labels are then analyzed and two results are used to describe the efficiency of the model: the accuracy, and the error rate. This challenge is not the only one, but it is the most commonly used for comparison purposes. The mission is to promote the development of better algorithms, techniques, and models to achieve increasingly better performance. The main issue is that most of these methods are designed to run on super-computers, making them very difficult to implement in real-time applications.

- **The Pattern Analysis, Statistical Modelling and Computational Learning Visual Object Classes Challenge (Pascal VOC)**

The PASCAL VOC [3] is another database of thousands of images. The main detection challenge consists of 20 categories of labeling and detection, which not only means being able to recognize what is in the frame, but also where it is. This is the main difference between ImageNet and PASCAL. The datasets of training images and validation images are accessible to use for research purposes through the development kits, which include the training images with their annotation files, and testing images.

2.4 Implementation with the Jetson TK1

We are using the NVIDIA Jetson TK1 embedded computer system. It is a low-power computer system, and our interest is to use it for mobile applications. The goal is to deploy a trained model using Caffe that will analyze the frames from a camera as they are being captured, and detect and localize the object(s) within the frame. The advantage of using CNNs for this task is that it is more flexible and intelligent.

III. RELATED WORK

Besides Convolutional Neural Networks, which have been at the vanguard of object classification and detection in the past few years, there are other approaches to object detection, DeformablePartModels(DPMs) [10] being one of those approaches. DPMs have a wide variety of implementations using different techniques, for example Histogram of Orientated Gradients (HOG) [14], or the recent Generalized Sparselet Models[13]. We are using Fast R-CNN, which is based on R-CNNs, which is not the only convolutional network structure. Other CNN models are based on Very Deep Convolutional Networks for Large-Scale Visual Recognition[11], commonly known as the Visual Geometry

R-CNN: Region-based Convolutional Network

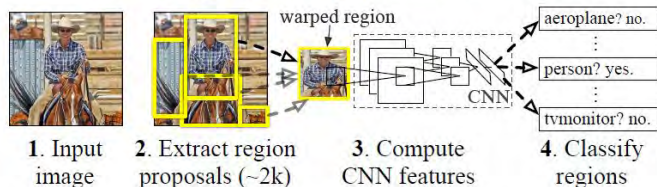


Figure 1: Object Detection System based on Regions with Convolutional Neural Networks [6]. The system takes an input image, and proceeds to extract region proposals for it. Afterwards, it processes the proposed regions in to the Convolutional Neural Network for classification and localization.

Group (VGG) networks, and the DeepPyramid DPM described in [12].

IV. EXPERIMENTAL RESULTS

Caffe [1] is an open source framework for machine learning algorithms. It is used to design, train, and test models on various applications. This framework was installed on the Jetson TK1 for deploying in real-time applications. We are using the Jetson TK1 because the chip (TK1) has a CUDA-based GPU—unlike any other low power embedded system—enabling us to run the computations in it to achieve faster performance. In order to have an effective application, we must follow three steps. The first step involves the design and training of a model for deployment. The second is writing the application to feed frames from the windows USB webcam that we were using. Once achieved, we proceed to the third step which is benchmarking the frames per second (fps) in which the application is able to perform, and the latency of the process—the amount of time required for processing a single frame.

4.1 Design and training

For this implementation, we tested the performance of a pre-trained network. When training a model based on the architecture described by Girshick [6] we must pre-compute the object proposals on the dataset. The most common method of doing this is to use Selective Search [8], which is based on MATLAB. We can use Fast R-CNN [7] to train CNNs in the PASCAL VOC [3] dataset. The model that we tested was the CaffeNet, which is a variation of the AlexNet model presented by Krizhevsky [5], fine-tuned on the PASCAL dataset.

4.2 Real-time Frame Capture

In order to do this we wrote a simple python application that feeds the frames to the CaffeNet model. After the model runs the convolutions, labels the object, and localizes it, it outputs the resulting frame. This model has the capability to label and localize within the frame, any object in the 20 categories of the PASCAL VOC Challenge [3], including people and chairs. The code is written to detect persons only, for testing purposes.

4.3 Results

The performance of the CaffeNet model can be

benchmarked by analyzing the amount of frames-per-second (fps) displayed in the output window and the latency, or the amount required to process a single frame. This model has a performance of <1 frame/second, roughly speaking. For the latency, it takes an average of 3.5 seconds to 4 seconds to process every single frame and display it in the output window.

V. DISCUSSION AND CONCLUSION

The continuous work by various computer scientists and mathematicians on Deep Neural Networks opens many opportunities for implementing these new networks on real-time applications for object detection. These new designs are efficient and more accurate at detecting objects, which means that they are able to do it faster. Our objective is to implement these deep learning networks on low-power systems, like the Jetson TK1, and use them in real-time applications for various applications, especially object detection. The results will show that it is possible to achieve near real-time performance and accurate object detection using deep learning networks. With the continuous development of new networks and models, the performance will increase, and it will open the opportunity to develop new applications.

This project is in a work-in-progress state, and as we keep moving forward, new and more efficient methods are being developed. The current performance is pretty impressive for a system like the Jetson TK1. Most of these deep learning models are used on high-end computers with state-of-the-art GPUs to analyze images in a fraction of a second. Nonetheless, the current performance has room for many improvements in order to achieve better performance. The system is currently running a pre-trained CaffeNet model, fine-tuned on the PASCAL VOC dataset. Although it is relatively small, the CaffeNet model was trained on the 1000-category of the ImageNet Challenge. It has a lot of data, parameters and labels which result in a bigger network that contains many categories that we will not be using. CaffeNet is based on AlexNet [5], which runs CNNs, not R-CNNs, being R-CNNs better for object detection.



Figure 2: Person detection: On the top row of the image appears the input frame of the USB Camera. On the lower row appears the frame after being processed by the convolutional network. This detection is for “person”. There can be multiple people in the frame detected at once.

Our future goals include designing a network based on the Fast R-CNN detector, and training that network on the INRIA [4] Person dataset to create a person/civilian detector. Also, we can create our own dataset using the ImageNet dataset with their annotations. We can pre-compute object proposals using Selective Search or other methods available like Learning Object Proposals (LPO) [9], and use this to train our own Fast R-CNN detector on a custom set of categories that fit our specific requirements.

ACKNOWLEDGMENT

The authors would like to acknowledge the support of the National Science Foundation, through NSF REU grant no. 1062672.

REFERENCES

- [1] Y. Jia, E. Shelhamer, J. Donahue, S. Karayev, J. Long, R. Girshick, S. Guadarrama, and T. Darrell, “Caffe: Convolutional architecture for fast feature embedding.”, arXiv:1408.5093, 2014.
- [2] J. Deng, W. Dong, R. Socher, L.-J. Li, K. Li and L. Fei-Fei, “ImageNet: A Large-Scale Hierarchical Image Database”, IEEE Computer Vision and Pattern Recognition (CVPR), 2009.
- [3] Everingham, M., Van Gool, L., Williams, C. K., Winn, J., & Zisserman, A., “The Pascal Visual Object Classes (VOC) Challenge”, International journal of computer vision, vol. 88, no 2, p. 303-338, 2010.
- [4] N. Dalal, and B. Triggs, “INRIA person dataset, 2011-04-10”, <http://pascal.inrialpes.fr/data/human>, 2005.
- [5] A. Krizhevsky, I. Sutskever, and G. Hinton, “ImageNet classification with deep convolutional neural networks”, NIPS, 2012.
- [6] R. Girshick, J. Donahue, T. Darrell, and J. Malik, “Rich feature hierarchies for accurate object detection and semantic segmentation”, CVPR, 2014.
- [7] R. Girshick. “Fast R-CNN,” arXiv e-prints, vol. arXiv:1504.08083v1 [cs.CV], 2015.
- [8] J. R. Uijlings, K. E. van de Sande, T. Gevers, and A.W. Smeulders, “Selective search for object recognition”, IJCV, 2013.
- [9] P. Krähenbühl, and V. Koltun, “Learning to Propose Objects”, CVPR, 2015.
- [10] R. J. López-Sastre, T. Tuytelaars, and S. Savarese, “Deformable part models revisited: A performance evaluation for object category pose estimation”, Computer Vision Workshops (ICCV Workshops), IEEE International Conference, 2011.
- [11] K. Simonyan, and A. Zisserman, “Very deep convolutional networks for large-scale image recognition”, arXiv preprint arXiv:1409.1556, 2014.
- [12] R. Girshick, F. Iandola, T. Darrell, and J. Malik, “Deformable part models are convolutional neural networks”, arXiv preprint arXiv:1409.5403, 2014.
- [13] H. O. Song, R. Girshick, S. Zickler, C. Geyer, P. Felzenszwalb, and T. Darrell, “Generalized Sparselet Models for Real-Time Multiclass Object Recognition”, Pattern Analysis and Machine Intelligence, IEEE Transactions on, 37(5), 1001-1012, 2015.
- [14] N. Dalal, and B. Triggs, “Histograms of oriented gradients for human detection”, IEEE Computer Vision and Pattern Recognition (CVPR), 2005.

Preparation of a Mechanochromic Elastomer using Liquid Crystal Dispersed in Polymer

Samantha Burns (University of Pennsylvania, Materials Engineering and Statistics), *SUNFEST Fellow*

Dr. Shu Yang, Materials Science and Engineering

Abstract— We have designed an inexpensive and sensitive mechanochromic system. Our system is prepared by a simple emulsion procedure of nematic liquid crystal in polydimethylsiloxane (PDMS). The resulting polymer dispersed liquid crystal (PDLC) exhibits a transmission change of 50% as a response to strain. Here we characterize the morphological, optical, and mechanical factors behind this transmission change. Understanding this mechanochromic behavior is essential for developing precise and reliable methods to tune a material's optical properties. We propose a new model that illustrates how mechanical strain modifies the polymer-liquid crystal interface and the nematic director fluctuation within the liquid crystal droplets. We propose that both of these factors play critical roles for the transmission change in PDLC samples. This work lays a new foundation for developing innovative mechanochromic devices, including smart windows and biomedical pressure sensors.

Index Terms—elastomer, liquid crystal, mechanochromism, optics, PDLC, sensor

I. INTRODUCTION

Many types of living systems use optical tools to communicate with each other, control their surroundings, and sense changes in their environments. The cuttlefish, for example, use elastic pigment sacs called chromatophores to quickly camouflage themselves and evade potential predators. Muscles surrounding these sacs contract and induce a change of color [4]. This mechanism is considered a mechanochromic system because it uses a mechanical stimulus to evoke an optical response. Mechanochromic systems are promising solutions to modern problems, such as energy conservation and biomedical sensing. For example, a smart window would conserve heating and cooling energy if it could control sunlight transmission by contracting and expanding its glass panes [1]. In addition, effective compressive bandages are being developed to visually indicate when an effective amount of pressure is applied to a patient [2]. Despite a wealth of mechanochromic research, we do not see many of these systems implemented commercially [6]. Barriers, such as cost and complex preparation methods, have limited mechanochromic applications. We aim to develop an inexpensive and simple method to prepare a mechanochromic system that requires low mechanical energy and enables a high level of optical control.

To this end, we have designed a polymer dispersed liquid

crystal (PDLC) system. Liquid crystal adopts properties from liquid matter and crystal solid matter [3]. We use a nematic liquid crystal, which consist of nanosized rods that flow like a liquid but are uniformly oriented with a director [9]. Dispersing liquid crystal droplets in a polymer allows researchers to utilize the unique optical properties of liquid crystal while harnessing the mechanical properties of a polymer [3]. To create an inexpensive and sensitive system, we use a low concentration of liquid crystal immersed in soft polydimethylsiloxane (PDMS). Our system changes from opaque to transparent upon compression. In the following sections, we describe the mechanical, optical, and morphological mechanisms underlying this mechanochromic response.

II. BACKGROUND

PDLC has been extensively studied in the past thirty years due to its unique optical properties. In its traditional, “swiss cheese” morphology, very small spherical liquid crystal droplets are suspended in a polymer matrix [7]. In this state, the refractive index of the liquid crystal does not match that of the polymer, causing light to scatter and the material to appear opaque. When the material undergoes stress, the droplets become increasingly oblate and the liquid crystal refractive index changes to match that of the polymer [3]. Deformation can be caused mechanically by shear, stretch, or compression; or electrically, such as putting a voltage across the material [7]. On the macro scale, these subtle deformations cause the material to change from opaque to transparent, making PDLC an intriguing material for window, display, and sensor applications.

Current mechanochromic techniques include: rearrangement of bonds, dye-dispersed systems, and photonic gels [8]. A PDLC-based mechanochromic device would most generally resemble the dye-dispersed system. In such a system, organic or organometallic small molecule dyes change their optical properties upon grinding, smearing, or pressing. The dyes form aggregates (in this case, liquid crystal clusters into droplets) when dispersed in an elastomeric matrix and these aggregates are deformed upon straining the matrix [8]. Key hurdles in current mechanochromic research include increasing the predictability and precision of optical changes and optimizing the amount of color or transmission change of a material with minimal mechanical strain [6]. In this paper, we discuss a simply designed PDLC material and demonstrate key properties that address how PDLC can be tuned to increase predictable optical changes and enhance mechanochromic sensitivity.

III. EXPERIMENTAL DETAILS

A. Materials

The PDLC samples in the subsequent experiments consisted of nematic 4-Cyano-4'-pentylbiphenyl (5CB) liquid crystal dispersions (Kingston Chemicals Ltd.). Dow Corning Sylgard 184 elastomer kit was used for preparing PDMS.

B. Fabrication of Mechanochromic PDLC Samples

Dow Corning Sylgard 184 silicone elastomer and curing agent were mixed at a weight ratio 30:1. 5CB was added to the solution at 5 wt% and the mixture was mechanically stirred for one minute. After degassing, the mixture was cast in a 25×15×1 mm glass curing cell and the thickness of the sample was controlled at ~ 1 mm. The sample was then cured at 120 °C for 20 minutes.

C. Characterization

Scattering spectra and transmission at various strains and angles were collected from a USB400 fiber optical spectrometer (Ocean Optics) with a custom-built compressor and an angle-resolved stage.

Optical images were obtained by optical microscopy (BX 1, Olympus) using polarizing condensers. Large droplet optical samples were created by preparing 30:1 Dow Corning Sylgard 184 silicone elastomer and curing agent. After degassing, the sample was cast in a petri dish. 1 μ L 5CB droplets were pipetted into the elastomer and stirred slowly for 10 seconds. The sample was cured at 65°C overnight. SEM images were taken by the Scanning Electron Microscope (JEOL 7500) at 5kV.

Mechanical PDMS samples were prepared by mixing elastomer and curing agent at 10:1, 20:1, 30:1, 40:1 and 50:1 weight ratios. Each sample was cured at 65°C overnight and cut into 30×7×1 mm films. Mechanical testing of PDMS samples at different curing agent ratios was completed using Instron tensile testing with a crosshead speed of 1 mm/min.

IV. EXPERIMENTAL RESULTS AND DISCUSSION

The following three subsections describe the mechanical, morphological, and optical characterization of our system.

A. Curing Agent Effect on Mechanical Sensitivity

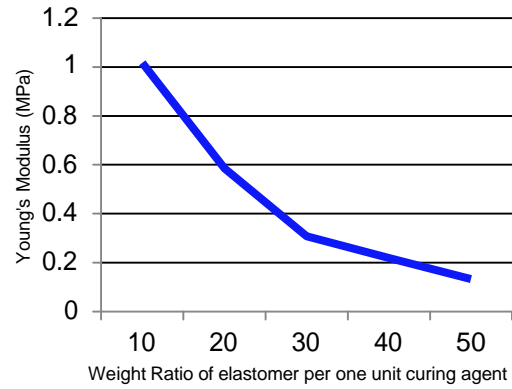
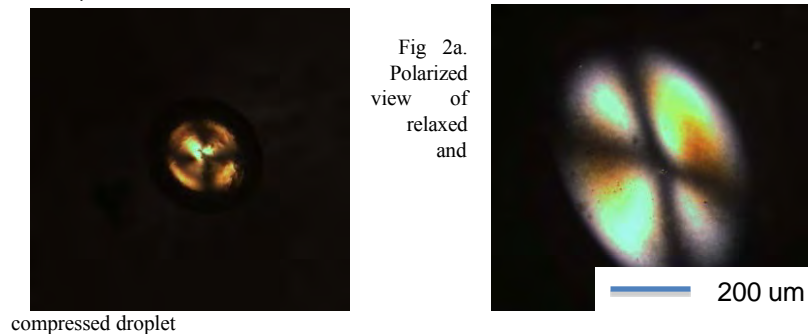


Fig 1. Young's Modulus versus Elastomer-Curing Agent Ratio

In a mechanochromic PDLC system, liquid crystal droplets are deformed by changing the shape of the elastomeric matrix that contains them. The Young's modulus is a measure for how sensitive a material will be to deform. The modulus for each PDMS sample was found by calculating the linear slope of the stress versus strain relationship from Instron testing. Fig 1 demonstrates the relationship between the Young's modulus of PDMS and the amount of curing agent used. A sample with a high elastomer ratio, such as a 50:1 mix, will have a lower Young's modulus. Using less curing agent consequently limits the amount of cross-linking that will occur during the curing process and result in more flexible elastomeric matrices. The rate of change for the Young's modulus of a sample becomes more stable as the elastomer ratio increases. Therefore, a higher elastomer ratio, such as a 30:1 or 40:1 mix, could be used in sample preparation to make systems with reliable mechanical flexibility. For our mechanochromic system, a high elastomer ratio is desirable for producing a flexible matrix with predictable deformation behavior.

B. Morphological Droplet Response to Stress

ImageJ software was used to analyze the size distribution of liquid crystal droplets in the mechanochromic films. Optical imaging of a 20:1 elastomer with 5% liquid crystal showed a mildly uniform distribution of droplets with a mean diameter of 5.1 μ m with a standard deviation of 1.84.



Optical imaging in Fig 2a show the radial configuration of 5CB liquid crystal droplets in the PDMS. Radial droplets result from homeotropic, or perpendicular, anchoring of nematic rods to the PDMS interface. A central defect results from the nematic director fluctuations that point toward the center of the spherical droplet. As the large droplet sample

was compressed, the cross-sectional area of the droplet expands biaxially.

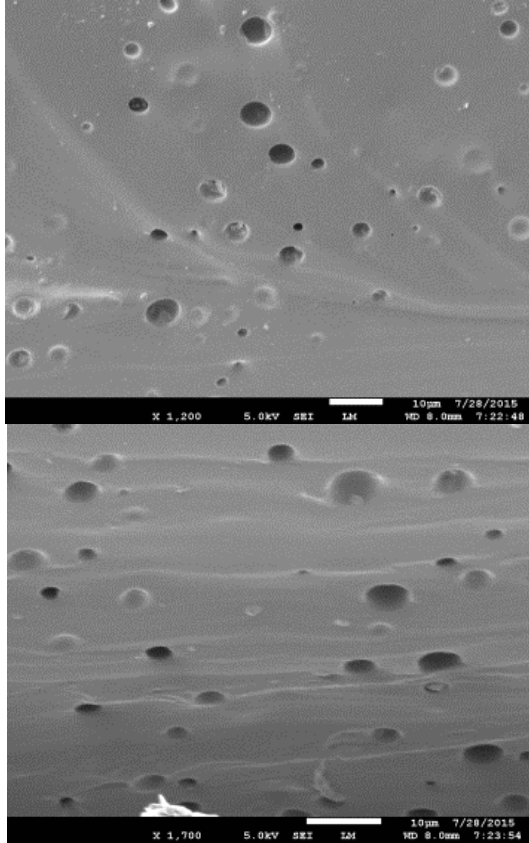


Fig 2b. SEM images of relaxed and compressed matrix

SEM images in Fig 2b depict a cross section view of the elastomeric matrix after liquid crystal was washed out of the sample with acetone. The relaxed sample shows circular cross sections of the droplets, indicating spherical three-dimensional shapes. As compression is applied, the droplets become oblate. As compression increases, the top of the droplet becomes flatter and its sides become more sharply curved. These new boundary conditions may inhibit homeotropic anchoring and change the liquid crystal morphology within the droplet.

C. Mechanochromic Modulation of Light

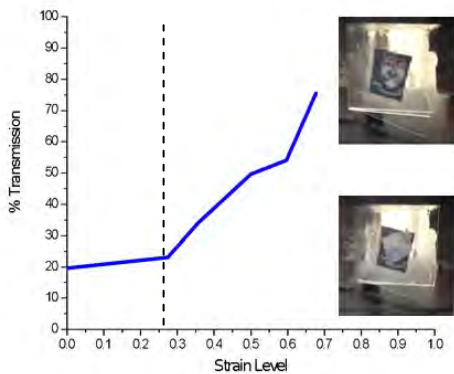


Fig 3a. Transmission versus Strain for 5% 5CB sample

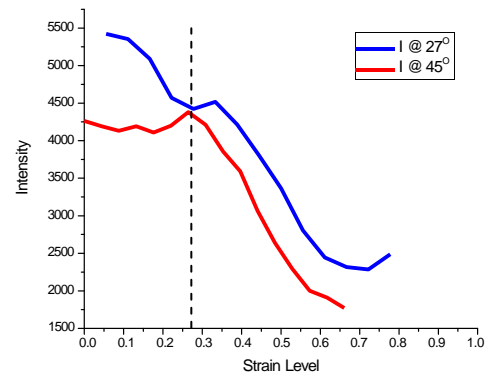


Fig 3b. Backscattering versus Strain for 5% 5CB sample

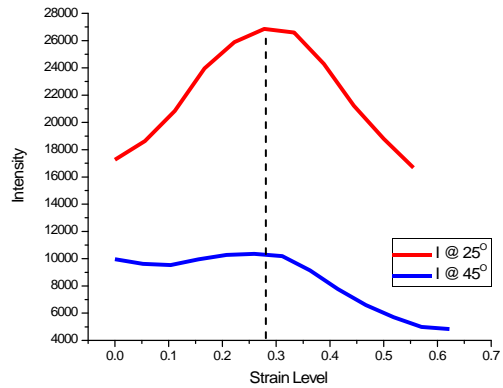


Fig 3c. Front Scattering versus Strain for 5% 5CB sample



(A) Undeformed, radial (B) Deformed, radial (C) Deformed, no defect present
Fig 3d. Cycle of morphology change for droplets

Our mechanochromic PDLC sample exhibit an absolute change of 50% transmission between its relaxed state and stressed state, as seen in Fig 3a. The change in transmission is not uniform; it has two discrete slopes. This suggests that two distinct processes are contributing to transmission change.

These two processes are also observed in Fig 3b and 3c. When the sample experiences strain levels less than 30%, back scattering is constant and frontscattering increases. After 30% strain, both backscattering and frontscattering decrease.

As seen in Fig 3d, compressive force can have two effects on a liquid crystal droplet. By changing the shape of the elastomeric voids, the elastomer-liquid crystal interface is altered. This changes the refractive index of the droplet, from its ordinary to extraordinary values. However, at a certain degree of compression, it is possible to reorient the director of nematic liquid crystal fluctuations. As the aspect ratio of the compressed droplet increased along the major axis, it becomes more difficult for rods to perpendicularly anchor to the droplet boundary. This suggests that a change in nematic director fluctuations at a particular strain level could contribute to an increase transmission and a decrease in light scattering. The data suggests that the change in droplet shape and the change in nematic order contribute to two distinct changes in transmission and light scattering.

V. CONCLUSION

In this paper, we discussed a procedure for preparing a new mechanochromic PDLC film. Using a low concentration of liquid crystal decreases the cost of production for such samples and makes this technology more viable for commercialization. Also, our results show that large changes in transmission can be obtained by compressing the PDLC film by less than a millimeter. This level of mechanical sensitivity also makes this system viable for many commercial applications.

In addition, our characterization of the mechanical, optical, and morphological behavior of liquid crystal droplets in the elastomer matrix demonstrated a more in-depth picture of how transmittance and scattering can be tuned. Changes in the shape of the liquid crystal droplet will modestly increase transmission and increase frontscattering. However, changes in nematic director fluctuations will sharply increase transmission while decreasing scattering. These mechanisms can be harnessed to create precise mechanochromic controls and sensors.

ACKNOWLEDGMENT

I would like to acknowledge the support of the National Science Foundation, through NSF REU grant no. 1062672.

I would like to thank postdoctorate fellow Dengteng Ge and doctoral candidate Yu Xia, at the University of Pennsylvania, with whom I collaborated extensively with on this project. I would also like to thank Dr. Shu Yang, of the University of Pennsylvania, for allowing me to work as a part of her research team and for her help and guidance on this project throughout the summer. In addition, I would like to thank Dr. Jan Van der Spiegel of the University of Pennsylvania for his encouragement and support of me and all the other SUNFEST students.

REFERENCES

- [1] Baetens, Ruben, Bjørn Petter Jelle, and Arild Gustavsen. "Properties, Requirements and Possibilities of Smart Windows for Dynamic Daylight and Solar Energy Control in Buildings: A State-of-the-art Review." *Solar Energy Materials and Solar Cells* 94.2 (2010): 87-105.
- [2] Compression Bandage Having an Integrated Strain Gauge. Patent.
- [3] Cairns, Darran R., Guy M. Genin, Amy J. Wagoner, Clyde L. Briant, and Gregory P. Crawford. "Amplified Strain-rate Dependence of Deformation in Polymer-dispersed Liquid-crystal Materials." *Applied Physics Letters Appl. Phys. Lett.* 75.13 (1999): 1872.
- [4] Chan, Edwin P., and Edwin L. Thomas. "Mechanochromic Photonic Gels." *Advanced Materials* 25 (2013): 3934-3947.
- [5] Deravi, L. F., A. P. Magyar, S. P. Sheehy, G. R. R. Bell, L. M. Mathger, S. L. Senft, T. J. Wardill, W. S. Lane, A. M. Kuzirian, R. T. Hanlon, E. L. Hu, and K. K. Parker. "The Structure-function Relationships of a Natural Nanoscale Photonic Device in Cuttlefish Chromatophores." *Journal of The Royal Society Interface* 11.93 (2014): 20130942.
- [6] Jiang, Ying. "An Outlook Review: Mechanochromic Materials and Their Potential for Biological and Healthcare Applications." *Materials Science and Engineering* 45 (2014): 682-89.
- [7] Korner, W., H. Scheller, A. Beck, and J. Fricke. "PDLC Films for Control of Light Transmission." *Journal of Physics D: Applied Physics J. Phys. D: Appl. Phys.* 27.10 (1994): 2145-151.
- [8] Pucci, Andrea, and Giacomo Ruggeri. "Mechanochromic Polymer Blends." *Journal of Material Chemistry* 21 (2011): 8282-291.

- [9] Whitmer, Jonathan K., Xiaoguang Wang, Frederic Mondiot, Daniel S. Miller, Nicholas L. Abbott, and Juan J. De Pablo. "Nematic-Field-Driven Positioning of Particles in Liquid Crystal Droplets." *Phys. Rev. Lett. Physical Review Letters* 111.22 (2013).

Exercising *Caenorhabditis elegans*

Hannah Corcos (University of Maryland Baltimore County, Mechanical Eng.), *SUNFEST Fellow*

Haim Bau PhD, Mechanical Engineering and Applied Mechanics

Abstract— Muscles deteriorate with age, restricting mobility. It is thought that regular exercise can lessen the rate of muscle deterioration, but it is not known if it affects longevity. Using the nematode *Caenorhabditis elegans*, we wish to determine a relationship between exercise and the aging process. To do this, we need to find a way to induce the animals to exercise. A method of exercising *C. elegans* was identified by exposing them to a fluid flow. Without food, the *C. elegans* maintained a constant low activity level until the external flow reached a threshold velocity. Once this threshold velocity was exceeded, the *C. elegans* assumed a heightened activity level. The effect of food on the activity level was also examined. In the presence of food, the animals' activity level declined since they were not actively searching for sustenance. Lastly, using different strains with mutated sensory neurons, it was determined that an elevated activity level is caused by the animals' cilia. This opens the way find how exercise affects mobility level as a function of age and longevity.

I. INTRODUCTION

Caenorhabditis elegans have been studied since 1974 when Sydney Brenner proposed using the nematode to study the nervous system [1]. Since then, *C. elegans* have been studied extensively. They are a model organism often used in medical research due to their small size, transparency, short life cycle, low number of neurons, and availability [2]. Genetically, there is little difference between generations because they are hermaphrodites [3]. These characteristics make *C. elegans* ideal for controlled experiments.

C. elegans move with an undulatory motion, but they have two distinct movements: crawling on a surface and swimming in fluid [4]. They move faster in fluid than on a surface. It is hypothesized that introducing the nematodes to a fluid flow will increase their activity level, hence exercising them. This would enable one to compare the aging process with two different populations, one that has been exercised and one that has not. It is also thought the touch sensory neurons are what cause this heightened level of activity.

II. BACKGROUND

i. Genetics

Much has been learned about genetics through studying *C. elegans*, including their complete genome sequence [5]. With this knowledge, scientists have been able to identify the genetic

causes of mutations and also create mutated strains that focus on a particular set of genes [6]. *C. elegans* have 302 neurons making their nervous systems much easier to study than other model organisms. There are many mutant strains of *C. elegans* that alter their nervous system [7]. This allows us to see the effects of different neurons.

ii. N2

The N2 strain, commonly known as wild-type, is the genetic baseline for *C. elegans*. They are of the same genetic structure as the *C. elegans* that live in the soil, but they are grown on petri dishes in a lab. Mutant strains are often compared to N2 to see the effects of different genes [8].

iii. Strains

MEC-3 CB1338

C. elegans have six mechanosensory neurons that detect touch [9]. The *mec-3* gene causes these touch receptors not to function so the nematode can no longer detect its surroundings [10].

MEC-4 TU253

The *mec-4* strain is similar to the *mec-3* strain, but rather than the mechanosensory neurons being suppressed, they degenerate over time [11].

OSM-6 PR881

Like the mechanosensory neurons, *C. elegans* also have chemosensory neurons which respond to chemical stimulation. At the ends of these neurons there are cilia, small hair-like structures that are used to detect their environment [12]. Studies have shown that cilia deficient *C. elegans* cannot swim and try to crawl through the fluid [13]. The *osm-6* strain mutates the worm's sensory cilia so the worm's mechanosensory and chemosensory behaviors are altered [14].

CHE-2 CB1033

The *che-2* strain is similar to the *osm-6* strain since the cilia are also altered. In the *che-2* strain, however, the cilia are shorter than they normally are. This also alters the behaviors mediated by

the mechanosensory and chemosensory neurons [15].

TAX-4 PR678

The *tax-4* strain is also deficient in chemosensory behaviors, but they still respond to mechanosensory stimulation. They have no response to temperature change as the other strains of *C. elegans* do [16].

III. MATERIALS AND METHODS

Set-up

A microfluidic device made of 1/8 inch acrylic was used in this experiment. The device consisted of circular holding chambers for the *C. elegans* and conduits to allow fluid to flow through. The fluid used was Nematode Growth Media (NGM) which is a common fluid environment used in studies of *C. elegans*. All worms used in this experiment were picked at the fourth larvae state the day before use to ensure they would all be at the same age. They were placed into the holding chambers, each of which had a conduit going through it. Each conduit was connected to plastic tubing which connected to a syringe. The flow was introduced to the system and kept constant by a multi-barrel syringe pump.

Exercising *C. elegans*

First, a method of exercising *C. elegans* was determined. Worms put in the NGM buffer move at a higher rate than those not in liquid, but this is not considered exercising. The hypothesis tested was that exposing *C. elegans* to a fluid flow would increase their activity level. Wild-type *C. elegans* were loaded into the holding chambers and allowed to acclimate for 30 minutes with no fluid flow. At the end of the 30 minutes, the flow started and a recording of the worms began. Data was recorded for the next three hours. Trials were first done with fluid flows at 0, 25, 50, and 100 $\mu\text{L/hr}$. After analyzing this data, four more trials were added at 8, 17, 33, and 42 $\mu\text{L/hr}$. The data was analyzed in one minute intervals at the beginning of each hour, and each trial lasted for three hours. Six worms experienced the flows for each trial, and each worm was analyzed individually for each time interval. The average number of body bends was then found for each fluid velocity

Food

No food was used while determining a method of exercise. This does not affect the results short term, but after a few hours, the worms will begin to starve. For a long term experiment, there will have to be food in the holding chambers so the *C. elegans* can survive. LG buffer was inoculated with *E. coli* bacteria and would then spend overnight in an incubating shaker. The next day, 15mL of the LG buffer would be spun in a centrifuge to separate the bacteria from the buffer, and then the bacteria would be washed with NGM. The bacteria would then be suspended in 6.5mL of NGM creating a food mixture concentrated approximately two-fold. Using the same conditions as without the food, trials were run at

velocities 0, 25, 50, and 100 $\mu\text{L/hr}$ for the same time intervals as above.

Sensory Neurons

After determining it is possible to exercise *C. elegans* with a fluid flow, the next step was to determine what caused the worms to have a heightened activity level. To do this, different mutant strains were tested against wild-type. It was hypothesized that the nematode's mechanosensory neurons are responsible for the heightened activity level. To test this, half of the holding chambers in the device contained *mec-3* and the other half contained wild-type. This increased accuracy, as the only variable was the different strains. Using the same time intervals as above, the nematodes were tested at 0 and 50 $\mu\text{L/hr}$. The same set up was used for the *mec-4*, *osm-6*, *che-2*, and *tax-4* strains.

IV. EXPERIMENTAL RESULTS

Exercising *C. elegans*

Introducing *C. elegans* to a fluid flow did increase their activity level. There was not a large increase from 0-25 $\mu\text{L/hr}$ and there was little difference from 50-100 $\mu\text{L/hr}$, but there was a big jump from 25-50 $\mu\text{L/hr}$ (see Figure 1). This shows there exists a threshold flow rate below which *C. elegans* maintain one level of activity and above which they maintain an elevated level of activity. Since the fluid flow increased the activity level, this is a method of controlled exercising of *C. elegans*.

Food

The activity level was fairly consistent for each flow rate immediately after putting the *C. elegans* into the microfluidic device. The activity level change occurred after letting them settle into the new environment for a short period of time. Adding food into the system drastically slowed the movements of the *C. elegans* (see Figure 2). Within the three hour period, the activity level went from highly active to barely active at all. This is due to the worms eating the food. As seen in Figure 2, the higher flow rates caused the number of body bends to decline faster than at the slower flow rates. A possible reason for the decline in motion is because they were not starved so they did not have to maintain an elevated activity level to search for food. This could indicate the *C. elegans* were not exercising in the presence of food. Using the same set-up and the same food concentration, another experiment was done to determine if *C. elegans* exercise in the presence of food. This time, the *C. elegans* put into the holding chambers did not experience a flow for two hours and then experienced a flow of 50 $\mu\text{L/hr}$ for the next two hours. After two hours with no flow, the worms had slowed to the point where they were barely moving. When the flow began, the activity level increased, though not by as much as when there was no food present. This shows that *C. elegans* will exercise in the presence of food.

Sensory Neurons

MEC

The data from the tests with *mec-3* and *mec-4* did not support the hypothesis. Both the *mec* and wild-type's activity level increased in the presence of a fluid flow which shows there is little or no connection between the mechanosensory neurons and the activity level.

TAX-4

The activity level of the *tax-4* strain increased with the fluid flow, more so than the wild-type or *mec* strains. This shows there could be a connection between either chemosensory neurons or temperature detection and exercise, but there is no definitive evidence there is.

OSM-6 and CHE-2

Unlike the other strains tested, *osm-6* and *che-2* did not have an elevated activity level when exposed to the fluid flow. Their activity level decreased with time indicating that they did not exercise. This shows the cilia are a possible cause of exercise.

Figure 3 shows the percent difference of the activity levels between 0 and 50 $\mu\text{L/hr}$ for the different strains. For example, the number of body bends of N2 *C. elegans* increased by slightly over 20% when it experienced the fluid flow.

V. DISCUSSION AND CONCLUSION

Introducing *C. elegans* to a fluid flow was determined to be an efficient method of exercise both in the presence and the absence of food. It was found there exists a threshold velocity below which the worms maintain a constant level of activity and above which they maintain an elevated level of activity. This leads the way to age related experiments. It can be seen if exercise extends the lifespan of *C. elegans* and if exercised worms maintain a higher mobility rate as they age. Though before longer term experiments can be done, the device should be re-designed so that the conduits are large enough to allow for the eggs to flow out of the holding chambers while still containing the adult worms. Otherwise, the holding chambers would become overcrowded which would not be ideal. By testing different strains of *C. elegans*, it was also determined that cilia causes *C. elegans* to exercise rather than the mechanosensory or chemosensory neurons. This can lead to further experiments with motion and cilia in areas such as propulsive power. It can be determined if the strains with mutated cilia have a weaker propulsive power which could be why they cannot exercise.

Appendix

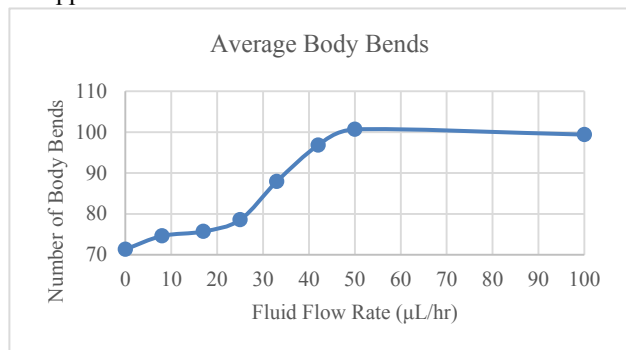


Figure 1: This graphs shows the average number of body bends per flow rate. It can be seen that the number of body bends increases with flow rate only until reaching a certain point. After this point, the number of body bends remains constant.

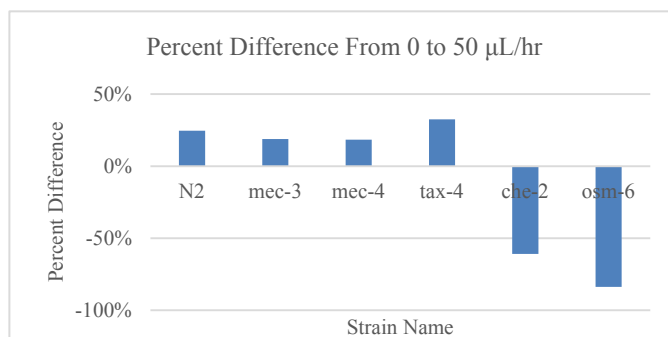
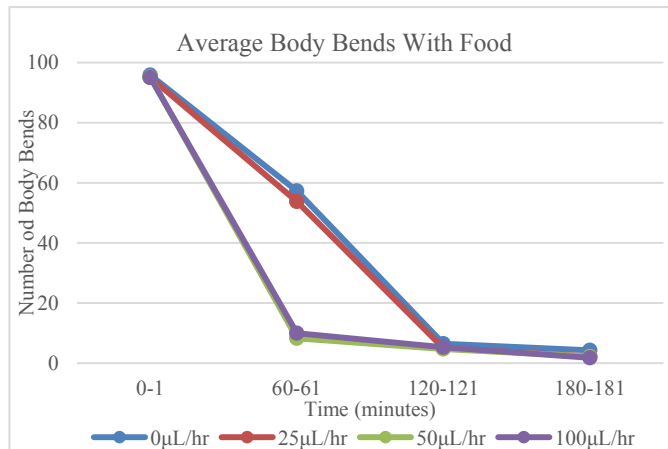


Figure 2: *C. elegans* experiencing higher flow rates had a faster decline in activity level.

Figure 1: Percent increase or decrease of the number of body bends after adding flow

I would like to thank David Raizen MD-PhD, with whom I collaborated extensively with on this project. I would also like to thank Haim Bau PhD for allowing me to work as a part of his research team and for his help and guidance on this project throughout the summer. I would like to acknowledge the support of the National Science Foundation, through NSF REU grant no. 1062672.

REFERENCES AND FOOTNOTES

1. S. Brenner, Genetics, 1974, 77, 71–94.
2. Titus Kaletta, Michael O. Hengartner (2006) Finding function in novel targets: *C. elegans* as a model organism. Nature Reviews Drug Discovery 5, 387-399.
3. L. Byerly, R.C. Cassada, R.L. Russell (1976) The life cycle of the nematode *Caenorhabditis elegans*: Wild-type growth and reproduction.
4. Stefano Berri, Jordan H. Boyle, Manlio Tassieri, Ian A. Hope, Netta Cohen (2009) Forward locomotion of the nematode *C. elegans* is achieved through modulation of a single gait.
5. LaDeana W. Hillier, Alan Coulson, John I. Murray, Zhirong Bao, John E. Sulston, Robert H. Waterston (2005) Genomic in *C. elegans*: So many genes, such a little worm.
6. David Fay. Genetic mapping and manipulation: Introduction and Basics.
7. J.G. White, E. Southgate, J.N. Thomson, S. Brenner (1986) The Structure of the nervous system of the nematode *Caenorhabditis elegans*.

8. Gems D, Riddle DL (2000) Defining wild-type life span in *Caenorhabditis elegans*.
9. Miriam B. Goodman, Glen G. Ernstrom, Dattananda S. Chelur, Robert O'Hagan, C. Andrea Yao, Martin Chalfie (2002) MEC-2 regulates *C. elegans* DEG/ENaC channels needed for mechanosensation. *Nature* 415, 1039-1042.
10. Jeffrey C. Way, Martin Chalfie (1988) *mec-3*, a homeobox-containing gene that specifies differentiation of the touch receptor neurons in *C. elegans*.
11. Monica Driscoll, Martin Chalfie (1991) The *mec-4* gene is a member of a family of *Caenorhabditis elegans* genes that can mutate to induce neuronal degeneration.
12. Peter N. Inglis, Guangshuo Ou, Michel R. Leroux, Jonathan M. Scholey (2006) The sensory cilia of *Caenorhabditis elegans*.
13. Pierce-Shimomura JT, Chen BL, Mun JJ, Ho R, Sarkis R, McIntire SL (2008) Genetic analysis of crawling and swimming locomotory patterns in *C. elegans*.
14. Joan Collet, Caroline A. Spike, Erik A. Lundquist, Jocelyn E. Shaw, Robert K. Herman (1998) Analysis of *osm-6*, a gene that affects sensory cilium structure and sensory neuron function in *Caenorhabditis elegans*.
15. M. Fujiwara, T. Ishihara, I. Katsura (1999) A novel WD40 protein, CHE-2, acts cell-autonomously in the formation of *C. elegans* sensory cilia.
16. Hidetoshi Komatsu, Ikue Mori, Jeong-Seop Rhee, Norio Akaike, Yasumi Ohshima (1996) Mutations in a cyclic nucleotide-gated channel lead to abnormal thermosensation and chemosensation in *C. elegans*.

Watts App: An Energy Analytics and Demand-Response Advisor Tool

Santiago Gonzalez, Case Western Reserve University, Electrical Engineering, *SUNFEST Fellow*

Dr. Rahul Mangharam, Electrical and Systems Engineering

Abstract— Real-time electricity pricing and demand response has become a clean, reliable and cost-effective way of reducing peak demand on the electricity grid. Annual revenues to end-users from demand response markets are more than \$700 million, making demand response the largest virtual generator in use [6]. DR-Advisor, an open source software tool created at the University of Pennsylvania, acts as a recommender system for building’s facilities manager. Using historical data from a building, DR-Advisor uses data-driven models to suggest suitable control actions to meet the desired load curtailment during demand response events. Using data sets from several buildings on the University of Pennsylvania’s campus, we enhance the capability of DR-Advisor by adding plug-ins for data-preprocessing and energy analytics.

I. INTRODUCTION

Wholesale electricity markets in the United States all use some form of real-time locational marginal pricing, where prices are calculated based on the operating conditions of the electricity grid. During intervals of high electricity consumption or peak demand, electricity prices increase substantially, making power consumption both inefficient and extremely cost intensive for end-use customers. Figure-1 shows an example of the volatility in real-time pricing from the New England independent system operator. The nominal price of electricity starts out at \$25/MWh but increases to \$800/MWh on July 20th, 2015 [5]. In an effort to reduce peak power consumption and decrease electricity costs, customers have begun to depend on demand response (DR). DR programs involve a voluntary response of a building to real-time price signal. In such programs, end-users receive a notification from the utility requesting a reduction in their electricity load during periods of peak demand. Customers curtail power consumption during a predetermined amount of time and as a result receive a

financial reward [2]. To be able to take advantage of real-time pricing and DR programs, the consumers must monitor electricity prices and be flexible in the ways they choose to use electricity. The challenge for large buildings lies in evaluating and taking control decision at fast time scales. Buildings are complex systems with many interconnected subsystems operating independently of each other. HVAC systems, chillers systems and lighting systems all operate independently of each other, making it difficult to analyze and synthesize to effect of any control action on system behavior.

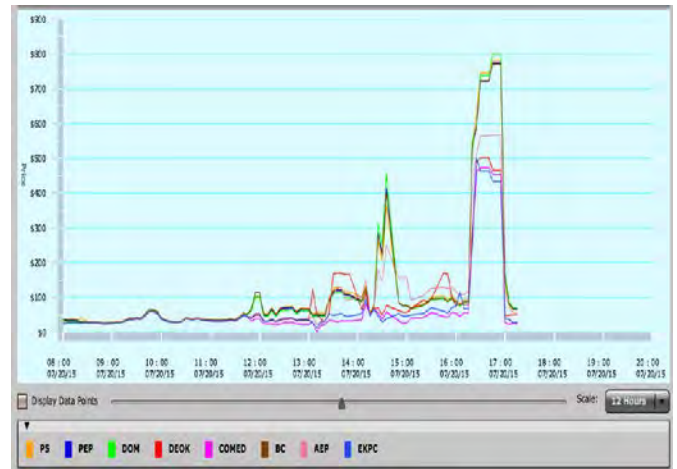


Figure 1- Real time electricity prices from New England ISO during 07/20/2015

DR-advisor uses regression tree-based algorithms to predict power consumption of large-scale commercial buildings in real time. These models are then used to create suitable control and scheduling strategies to meet the desired curtailment during a DR event. The problem is that data-driven model predictive accuracy depends of the quality of the data used for training the model. Building management systems consist of thousands of sensors embedded in the systems that control the internal environment, which often break or go offline causing noisy data. My work this summer consisted of creating a framework for data preprocessing which takes historical data files from any Penn building processes them to create suitable structure for training of data-

driven model. Processing includes outlier removal and interpolation. I also developed the capability to perform energy analytics on regression trees. This was the first step in designing a query system for the facilities managers. I then evaluated my contributions with data sets containing power consumption data for buildings on the University of Pennsylvania campus.

II. BACKGROUND

Electricity generators and utility companies use real-time locational marginal pricing, making electricity costs exceptionally sensitive to human behavior and extreme weather conditions. This translates into electricity prices dozens of times more expensive for end-users. For instance, at the University of Pennsylvania, the nominal rate of \$30/MWh increased to \$817/MWh during a hot summer day in 2011, a 27-fold increase. The five most expensive days cost \$1.47 million, accounting for 5.1% of the total bill [1].

2011 Hourly Real Time Mkt prices based on Locational Marginal Pricing (LMP) for PECO by PJM

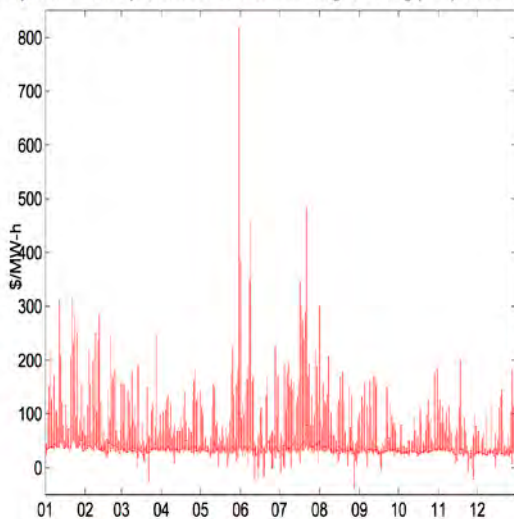


Figure 2: 2011 Hourly Real Time Market prices based on Location Marginal Pricing for PECO by PJM

In order to make effective use of DR programs, end users must be able to both predict power consumption and take appropriate actions in real time. Currently, rule-based and model-based strategies are the two most common approaches to responding to DR events. In rule-based strategies, curtailment is met through the implementation a pre-programmed plan. Although simple, the rule-based approach does not account for historical building or weather data. Rule-based strategies also lack any predictability capabilities. Model-based strategies rely on mathematically modeling a building and its equipment. The models are used to predict power

consumption and to synthesize control strategies [3]. Buildings are complex systems with a large number of individual components that interact in a convoluted manner, making the creation of high fidelity models both time and cost intensive. In addition, complex models involve many factors that hinder the facility manager's ability to interpret and synthesize data in a meaningful manner.

DR-advisor uses a regression tree-based algorithm, whose innate characteristics make it a suitable strategy to meet the challenges that DR events pose. Below, I outline some of the unique advantages which make regression trees suitable for solving the challenges of demand response [4].

- Fast computation times
- Handle a lot of variables
- Robust to missing data and outliers
- Very easily interpretable

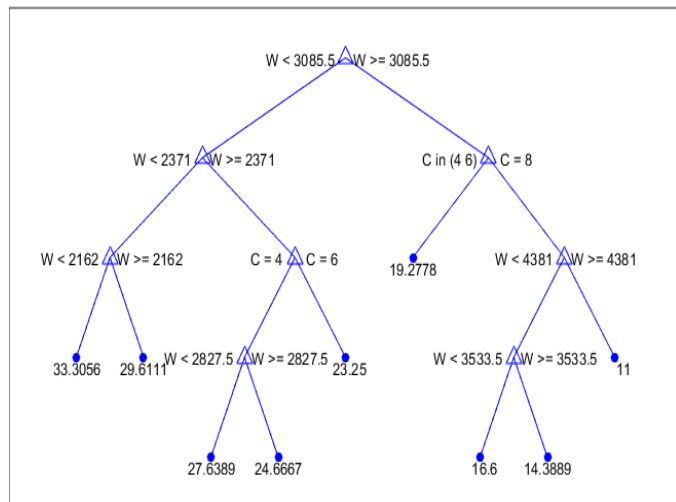


Figure 3: Regression Tree created by fitrtree method in MATLAB

A. Data Description:

Each regression tree needs to be trained on time-stamped historical data. I worked with data for nine buildings on the University of Pennsylvania Campus. The buildings that were included were Annenberg Center, Annenberg School, Clinical Research Building, College Hall, David Rittenhouse Laboratory, Goddard Labs, Huntsman Hall, and Vance Hall. Each building had comma separated value (CSV) files with weather, schedule and building data. The data included information for approximately 18 months at a resolution

of 1 hour time-steps. The CSV files consisted of 17 columns with proxy variables that included year, month, day of month, hour of day, building area and occupancy, weather variables including outside air temperature, dew point, relative humidity, incident solar radiation, wind speed, gusts speed, wind direction, heating and cooling degree days, and the power consumption in kW.

For some of the buildings, up to 25% of the data was either missing or considered an outlier. Instead of discarding valuable data, the goal was to create a plug-in for DR-Advisor that would remove outliers, and interpolate over missing data to improve model accuracy.

III. CASE STUDY

I will use College Hall to present a comprehensive case study. College Hall was the first building on the West Philadelphia campus and currently home of the President, Provost, School of Arts and Sciences, the Department of History and the Undergraduate Admissions Office. College Hall has 6 floors with a total gross area of 110,266 square feet. The CSV file for College Hall had historical data starting on the July 18th, 2013 and ending on February 4th, 2015.



Figure 4: College Hall

A. Pre-Processing

Using the MATLAB statistics and machine learning toolbox, I created scripts for each of the buildings that contained functions for the importation, outlier removal, and interpolation of data. The script imported the data by parsing the CSV file and assigning each of the columns to a variable. Predictor features were assigned to X and the power consumption values assigned to Y. I then created a function that calculated the mean (\bar{x}) and the

standard deviation (σ) of Y.

$$\sigma = \sqrt{\frac{\sum(x-\bar{x})^2}{n}} \quad \bar{x} = \frac{\sum x_i}{n}$$

Data samples that were two standard deviations away from the mean were deemed outliers and removed from.

B. Interpolation

For the interpolation of data, we had to make several assumptions in attempt to characterize missing data. For non-proxy variables and power consumption values, we took values of zero to be missing data. For power consumption values, the assumption is justified by the observation that under normal operating conditions, any occupied building will always be consuming power. For non-proxy variables, we found that zeros could indicate both missing and actual values. In the case of missing value, the interpolation would act as intended. In the case that we interpolated over actual zero values, it was expected that neighboring values would be close to zero, since weather data exhibits linear behavior at high resolutions. Therefore, the interpolated value tended to be close to zero. Overall, we found that interpolation of non-proxy variables led to higher model accuracy. Interpolation was not applied to proxy variables, because it was not possible to distinguish in between missing data and samples that had values of zero.

After testing several interpolation methods, we found linear interpolation to be the most effective in handling long strings of missing values. I used the interp1 method from MATLAB, in which the interpolated value at a query point is based on linear interpolation of the values at neighboring grid points in each respective dimension. The equation is outlined below, where (x, y) is the query point to be interpolated and (x_0, y_0) (x_1, y_1) are the neighboring data samples.

$$y = y_0 + (y_1 - y_0) \frac{x - x_0}{x_1 - x_0}$$

Power consumption training data for College Hall before and after outlier removal and interpolation is shown in Figure 4.

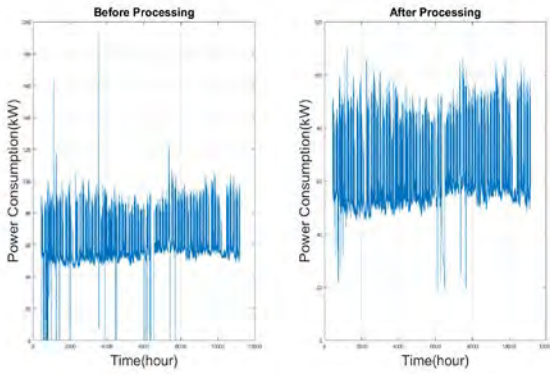


Figure 5: Left: College Hall Power Consumption before Processing. Right: College Hall Power Consumption after Processing

IV. RESULTS

The metric for prediction accuracy was the normalized root mean square error (NRMSE). NRMSE is the RMSE divided by the mean of the data. The RMSE represents the sample standard deviation for the difference between predicted values and observed values. To test the efficacy of outlier removal and interpolation, I trained models for all of the buildings with both raw data and pre-processed data. I then calculated and compared NRMSE values for models trained with both the raw and processed data. The NRMSE values are shown in Table-1.

Regressions trees tend to have high variance and may sometimes over fit the data. It is a tradeoff to be paid for estimating a simple model. In order to grow more stable trees, DR-Advisor uses several ensemble methods. The effects of pre-processing were evaluated on the following algorithms: single regression tree, k-fold cross-validated trees, and random forests.

DRL	Single Tree	13.12	11.80
	Cross-Validated Tree	9.93	10.57
	Random Forest	8.60	8.99
Goddard Labs	Single Tree	25.99	16.41
	Cross-Validated Tree	25.49	16.14
	Random Forest	17.73	15.55
Vagelos Labs	Single Tree	68.87	44.28
	Cross-Validated Tree	68.15	43.98
	Random Forest	68.38	43.18
Annenberg School	Single Tree	23.76	22.84
	Cross-Validated Tree	21.94	21.84
	Random Forest	19.91	19.88
Fisher and Duhring Wings	Single Tree	43.58	31.40
	Cross-Validated Tree	39.09	26.97
	Random Forest	34.77	23.61
CRB	Single Tree	19.36	5.20
	Cross-Validated Tree	10.61	4.54
	Random Forest	8.04	3.34
Annenberg Center	Single Tree	29.31	29.46
	Cross-Validated Tree	28.49	27.81
	Random Forest	27.88	28.05

Table 1: NRMSE values for buildings on the Penn Campus

Building	Method	Before Processing NRMSE %	After Processing NRMSE %
College Hall	Single Tree	21.84	14.05
	Cross-Validated Tree	17.39	11.50
	Random Forest	12.27	11.23
Vance Hall	Single Tree	17.49	14.04
	Cross-Validated Tree	14.24	11.01
	Random Forest	10.39	9.26

Outlier removal and interpolation made significant improvements to the prediction accuracy of the models. College Hall saw an improvement of 35.7% for the single tree, 33.9% for the Cross Validated Tree, and 8.5% for the random forest. Figure-4 shows prediction for each algorithm compared to the ground truth both raw and processed data.

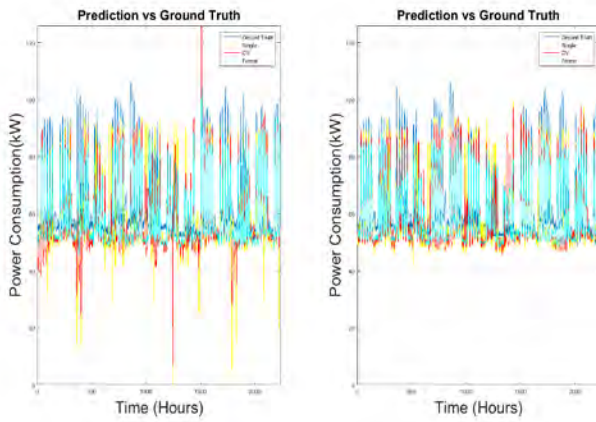


Figure 6: Left: College Hall Power Consumption Prediction with Raw Data. Right: College Hall Power Consumption Data with Processed Data.

It is important to note that proxy variables are important predictor of building power consumption. This is because they capture repeated patterns of occupancy and building operation. Figure-5 shows the importance of each of the predictor variables. Since neither outlier removal nor interpolation were performed on proxy variables, improvements were not quite as effective as they might have been had proxy variables been able to be processed.

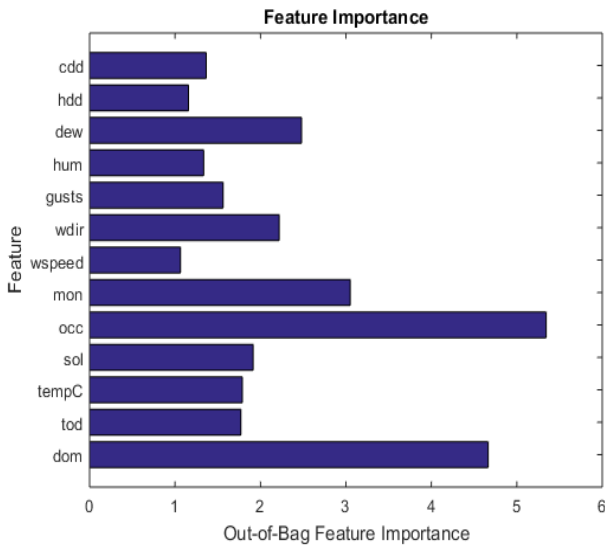


Figure 7: Feature Importance for training College Hall model

A. Filtering of Model Predictions:

Demand Response advisor uses the fitree MATLAB method to grow the regression trees. The fitree method works by recursively partitioning the feature space into a set of rectangles and then fitting a simple model in each

one. The fitree method starts by considering input data and all possible binary splits on every predictor, and then selecting a split based on the best optimization criterion. It then repeats recursively until it meets a stopping criterion. Stopping criteria is met under two circumstances. The first condition is when the mean squared error (MSE) for the observed response in the node drops below some predetermined threshold. The second circumstance is when there are fewer than the minimum amount of observations in the node. The minimum amount of observations is predetermined by the user. A node that fits the stopping criteria is called a leaf node. Although a 1 data point-per-leaf minimum requirement can be assigned as the stopping criterion, a very large tree might over fit the data. Therefore, leaf nodes tend to have a set of data points within the partitioned space. By querying the data samples within each partitioned space, we can get insights into building behavior at selected levels of power consumption.

B. Procedure:

We find all the leaf nodes that lie within a user-specified power consumption range. We then find the data points that lie within each of the leaves. The value of each feature is extracted from each data sample and added to a data structure that groups together values for equivalent features for all of the data points within the specified range.

For the College Hall data, we split power consumption data into 10 different bins of equal width. We then grouped all of the data samples that lied within each bin. Figure-6 shows the average prediction of each leaf.

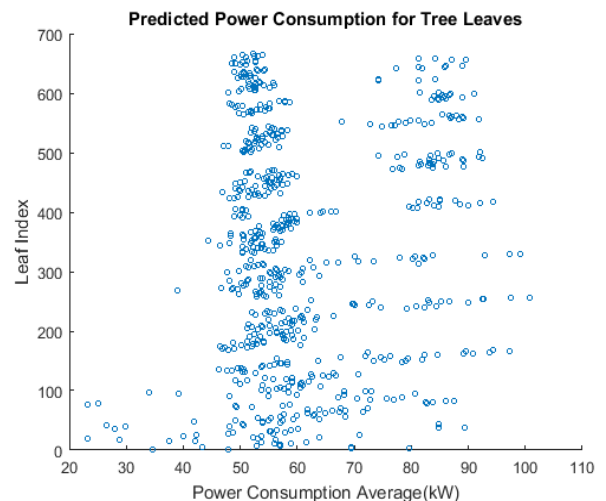


Figure 8: Plot of Power Consumption Averages for Leaf Nodes in College Hall

For each of the bins, we calculated the confidence interval and support. Confidence interval and support give insight into the frequency and certainty in which the building will consume a specific amount of power. We also use it to find any rare events, occasions in which an event has less support but higher confidence.

Figures with boxplots for each of the non-proxy predictor features were displayed. Each figure contained a boxplot for each of the bins. The boxplots provide the ability for users to see the distribution for each feature at a given power consumption. For example, the user could find under which temperature conditions the building would consume 90-100 kW of power. Figure-7 shows temperature feature distribution at each bin. For proxy variables, the three most frequently occurring values were calculated. The user can calculate, for example, what

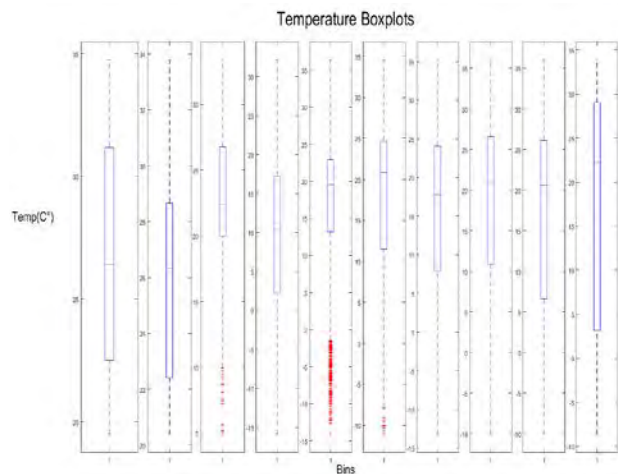


Figure 9: Boxplots of Temperature for each of the Bins in the College Hall Data.

V. CONCLUSION

Electricity costs are the single largest component of a large commercial and industrial building’s operating budget. For such consumers, buying and reacting to real-time electricity prices is not as simple as paying a flat-rate monthly bill. Their power consumption demands are sensitive to both human behavior and weather conditions. DR- Advisor, a software tool that acts as a recommender system for the building’s facilities manager, provides suitable control actions to meet the desired load curtailment while maintaining operations and maximizing the economic reward. We show that by preprocessing the incoming data, we dramatically

improve the performance and accuracy of the models used by DR-Advisor. We also show that by querying the regression trees we make regression trees more interpretable by getting insight into building behavior not attainable otherwise. The developed plug-ins will be added to the DR-Advisor toolbox.

VI. ACKNOWLEDGMENT

I would like to thank Madhur Behl, graduate student at the University of Pennsylvania, with whom I collaborated extensively with on this project. I would also like to thank Dr. Rahul Mangharam for allowing me to work as a part of his research team and for his help and guidance on this project throughout the summer.

REFERENCES

- [1] Behl, Madhur. “Sometimes, Money Does Grow On Trees: Data-Driven Demand Response with DR-Advisor”
- [2] C. Goldman. Coordination of energy efficiency and demand response. *Lawrence Berkeley National Laboratory*, 2010.
- [3] D. B. Crawley, L. K. Lawrie, *et al.*, “Energyplus: creating a new generation building energy simulation program,” *Energy and Buildings*, vol. 33, no. 4, pp. 319 – 331, 2001.
- [4] L. Breiman, “Random forests,” *Machine learning*, vol. 45, no. 1, pp. 5–32, 2001.
- [5] New-England ISO. (2013) Real-time maps and charts, archives.
- [6] P. Interconnection, “2014 demand response operations markets activity report,” 2014.

Hearing Loss: Piezo-polymers Nano-fibers for Bio-medical Applications

Mario Gutierrez (North Park University & Physics), SUNFEST Fellow

Dr. Jorge Santiago Aviles, Electrical Engineering Department

***ABSTRACT-* Hearing loss happens when hair cells inside the cochlea are damaged. About one third of the people in United States have some degree of hearing loss. This can possibly be solved by replacing those damaged hair cells with polyvinylidene fluoride (PVDF) nanofibers. PVDF is a highly non-reactive and pure thermoplastic fluoropolymer produced by the polymerization of vinylidene difluoride. PVDF have great piezoelectric properties, meaning that it has the ability to generate an electric charge in response to an applied mechanical stress. In this research, I used a computer program to simulate a cylindrical cantilever, which resembles a hair cell in the cochlea, and analyze the response of the frequencies by changing parameter values (length and diameter). Here, I report that I was able to analytically verify that the frequencies obtain from the computer program are similar with those obtain using an equation that I was able to derive. I also simulated two different conditions of the fiber to obtain the current that each fiber produce when stimulated in the audible frequency range of 250 – 2500 Hz.**

INTRODUCTION

On average, three of every one thousand people in the United States are functionally deaf. Though more than half became deaf relatively late in life; fewer than one out of every thousand people in the United States became deaf before 18 years of age [3]. There are many reasons for hearing loss, but the most common reason is known as “sensorineural” hearing loss, where hair cells in the cochlea are damage. Aging and prolonged exposure to loud noise may cause wear and tear on the hairs or nerve cells in the cochlea that send electrical signals to the brain. When these hair cells are damaged or missing, electrical signals are not transmitted as efficiently, and hearing loss occurs [2]. Currently there are no medical or surgical methods of replacing or repairing hair cells in the cochlea. However, hearing loss can be treated with hearing aids or cochlear

implants.

Unfortunately, cochlear implants are invasive, expensive, and its parts need to be replaced often. Advance research in nanotechnology can potentially be a solution to replace damage hair cells in the cochlea. My work consists of using COMSOL MultiPhysics version 5.1 to simulate a cylindrical cantilever, which resembles a hair cell in the cochlea.

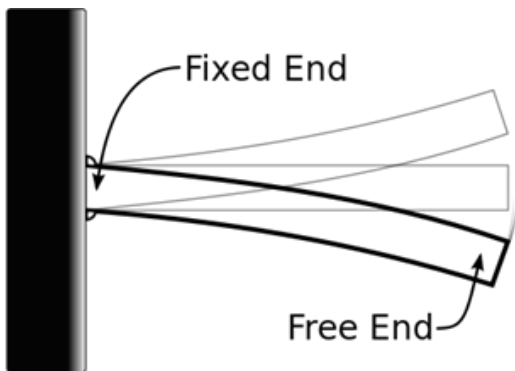


Figure 1 – This picture shows cantilever beam fixed at one end and free on the other end. This cantilever beam can be model in COMSOL as a hair cell.

Vladsinger, Oscillating cantilever beam, 2009, Cantilever Beam. Web. June 2015

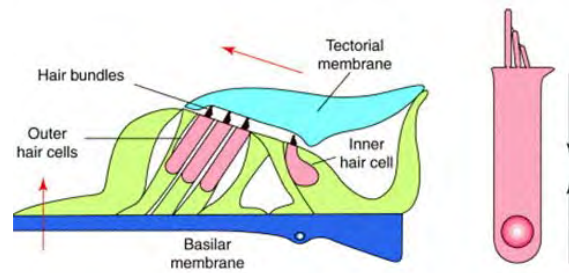


Figure 2 – This is how a human hair cell actually looks like. A cantilever beam is structurally similar to a human hair cell.

Fettiplace, Robert, Clues to the cochlear amplifier from the turtle ear, 2001, Science Direct. Web. June 2015

I'm using COMSOL to simulate a cylindrical cantilever because COMSOL is be able to account for coupled or multiphysics phenomena and you can further expand the simulation platform with dedicated physics interfaces and tools for electrical, mechanical, fluid flow, and chemical applications. The purpose of simulating a cylindrical cantilever in COMSOL is to analyze the response of the frequencies by changing parameter values (length and diameter) of the cantilever. We can also obtain the current of the fiber by stimulating the fiber in the audible frequency range of 250 – 2500 Hz. These results will help the rest of the group to spin nanofibers with specific dimensions

that can naturally respond to the audible frequency and send electrical signals to the brain.

BACKGROUND

A cochlear implant is a small, complex electronic device that can provide a sense of sound to a person who is profoundly deaf or severely hard-of-hearing. The implant consists of an external portion that sits behind the ear and a second portion that is surgically placed under the skin [4]. Cochlear implants bypass damaged portions of the ear and directly stimulate the auditory nerve. Signals generated by the implant are sent to the auditory nerve of the brain, which recognizes the signals as sound [4]. Unfortunately, cochlear implants are very expensive, and not a lot of people can afford a surgery. The total cost ranges from \$50,000 to \$100,000 for those without health insurance. Also, cochlear implants require continual maintenance, and some of its parts need to be replaced often, which at the time of replacement, the patient will need to go under surgery again.

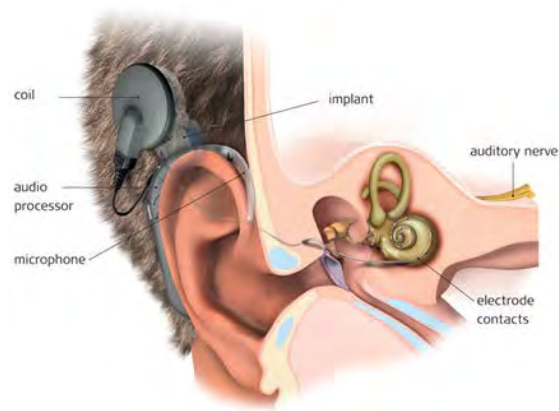


Figure 3 – This picture shows how a cochlear implant looks and how it works.

Cochlea implant, London Cochlear Implant Clinic, Web. June 2015

Nanoscience and nanotechnology are the study and application of extremely small things and can be used across all the other science fields, such as chemistry, biology, physics, materials science, and engineering [1]. This technology has allowed many researchers to experiment and improve technologies that are already being used. For nano-biomedical implants, this type of technology can potentially open new doors and create a solution for those expensive surgeries. The development of a polymer electrode based piezoelectric cochlear implant device with PVDF is the most sensitive piezoelectric polymer being used to create this nanofiber [5].

PVDF is a semi-crystalline polymer that consists of four crystalline phases. It is a non-reactive and pure thermoplastic fluoropolymer produced by the polymerization of vinylidene difluoride. PVDF is used in applications requiring highest purity, strength, and resistance to solvents, acids, bases, and heat. Furthermore, PVDF has a low density of where E is the Young's Modulus of $2.5974e^9$ GPa, ρ is density of $1.78g/cm^3$, d is the diameter, and L is the length.

well known that proper mechanical stretching and electrical poling are necessary to achieve good piezoelectricity. Piezoelectricity is important for this application because piezoelectric-effect is the ability to generate an electric charge in response to applied mechanical stress, and this charge can send an electrical signal to the brain. One way to create PVDF nanofibers is by electrospinning, a process that uses an electrical charge to draw very fine (micro or nano scale) fibers from the PVDF solution. During electrospinning, the diameters of the fibers could be controlled by adjusting various electrospinning parameters, such as PVDF concentration, electrospinning voltage, needle-to-collector distance, and x-y stage moving speed.

Increasing the stage-moving speed could produce thinner PVDF fibers, however higher speed (more than 90mm/s) would terminate the electrospinning process, making the fiber discontinuous.

The objective of this research is to simulate a cylindrical cantilever, which resembles a hair cell in the cochlea, and analyze the response of the frequencies by changing parameter values (length and diameter). In addition, analytically verify the frequencies obtained from COMSOL that will send an electrical signal to the brain in the audible frequency range of 250 – 2500Hz. Furthermore, measure the current of the fiber when stimulated in the audible frequency range.

EXPERIMENT

Using COMSOL I was able to simulate a cylindrical cantilever. This was accomplished by these procedures.

Procedures:

1. Open COMSOL from the desktop.
2. Select "Model Wizard" (which will guide you to select your geometry, physics, etc.)
3. Select "3D dimension model" and click next.

4. Under physics, select “Piezoelectric devices” which is under structural mechanics. After selecting the physics click add and then click on study.

5. In the study window select “Eigenfrequency”. This type of study corresponds to the natural frequencies of vibration. Then click done, this will bring you to the COMSOL desktop.

Once you reach the COMSOL desktop follow the next instructions:

6. In Model builder right-click in “Global Definition” and add Parameters.

7. Under Parameter settings add diameter (D) = 100 nm and length (L) = 100 μm .

8. Click on Geometry and set the units to μm .

9. To create a nanofiber right click in Geometry and select “cylinder”.

10. Under the cylinder settings, type D/2 for Radius and L for length then click Build All Objects.

11. Right-click on “materials” and under User-Defined Library selected “(PZT-5H)(Kynar 460)” this is the material that we created with similar PVDF properties.

12. Right-click on “Solid Mechanics” and select “Fixed Constraint” and manually select one side of the cylinder where you want it to be fixed.

13. Right-click on “Electrostatics” and select “Terminal” and under terminal settings in terminal type select Voltage and set the Voltage equal to zero.

14. Once again, right-click on “Electrostatics” and select “Floating potential” and under settings select all boundaries except the one side that is set as Terminal.

15. Next, right click in mesh and select Free Quad. Manually select top and bottom parts of the cylinder and set the minimum element size to D/3. After, right click in mesh again and select Swept and select Remaining, under element size select a finer swept and click Build All. I did this type of mesh because the default mesh, tetrahedral, has a lot of elements and the aspect ratio is big, therefore using a free quad and then a swept makes the mesh have less elements and it is faster for COMSOL to simulate.

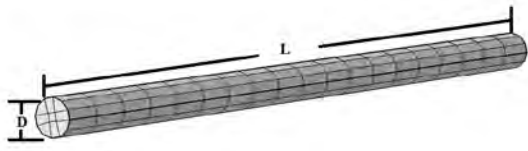


Figure 4 – This is how the cylindrical cantilever should look after the mesh is completed.

16. Under Study in Eigen-frequency, click compute and wait for the simulation to converge.

17. Under Results, click Mode Shape and you will see the results of the Eigen-Frequency.

1. Furthermore, to study the frequency in different dimensions go back up in the settings window and right-click in “study” and add a parametric sweep and add parameter values for diameter and length.

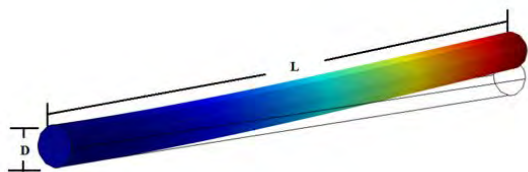


Figure 5 – Shows the displacement of the cylindrical cantilever at its first natural frequency.

After setting up different parameter values for the diameter and length, we were able to obtain the frequency output at different dimensions from COMSOL. To verify that we were obtaining the right frequencies at different dimensions we were also able to derive an equation for frequency for a cylindrical cantilever, where frequency is:

$$f = \frac{1.875^2}{8 * \pi} \left(\sqrt{\frac{E}{\rho}} \right) \left(\frac{d}{L^2} \right)$$

where E is the Young’s Modulus, ρ is density, d is the diameter of the cylinder, and L is the length of the cylinder.

I was able to derive this equation from the Free Vibration of a Cantilever Beam[11] a mathematical analysis for a cantilever beam with a rectangular cross section, where the frequency equation of a rectangular beam is:

$$f = \frac{1.875^2}{2 * \pi} \left(\sqrt{\frac{EI}{\rho AL^4}} \right)$$

where E is the Young’s Modulus, I is the moment of inertia of a rectangular cross section:

$$I = \frac{bd^3}{12}$$

where b and d are the breadth and width of the beam cross section, A is the area of a rectangle, and L is the length.

In the case of a cylindrical cantilever I was able to use this equation using the respective moment of inertia of a circular cross section and the area of a circle. That is to say that the frequency equation of a cylindrical cantilever is:

$$f = \frac{1.875^2}{2 * \pi} \left(\sqrt{\frac{EI}{\rho AL^4}} \right)$$

where E is the Young's Modulus, I is the moment of inertia of a circular cross section:

$$I = \frac{\pi}{64} d^4$$

where d is the diameter, A is the area of a circle, and L is the length. Plug in for I and A in the equation and that gives us:

$$f = \frac{1.875^2}{2 * \pi} \left(\sqrt{\frac{E \frac{\pi}{64} d^4}{\rho \frac{\pi}{4} d^2 L^4}} \right)$$

after deriving this equation we are able to obtain the frequency for a cylindrical cantilever which is:

$$f = \frac{1.875^2}{8 * \pi} \left(\sqrt{\frac{E}{\rho}} \right) \left(\frac{d}{L^2} \right)$$

Furthermore, to obtain the current from the fiber I simulated two different models. One model was fixed at the base of the cylinder and displaced at the top and the other model was only displaced at the base. I simulated these two models because that is how the hair cells behave in the cochlea. To obtain the current from the fiber, start from step 7. Under parameter settings add displacement values of .1, .3, .5 μm . Skip to step 12 and for one model leave step 12 the same but for the model delete this step. Proceed to step 16 and delete Eigen-frequency, right-click in study and add Frequency Domain. Under frequency domain settings, add the audible frequency range of 250 – 2500 Hz. Once again, right-click in study and add a parametric sweep and add the parameter values for length (L) = 10, 20 μm , diameter (d) = 100, 200 nm, and displacement (DP) = .1, .3, .5 μm . After setting up our parameter values click on study and wait for the simulation to converge. In results right-click in “Derived Values” and select “Surface Integration”. Under settings click on “Expression“ and write “abs(imag(es.JdZ))” which will calculate the absolute current at the base. After click on “Evaluate” and wait for the simulation to converge.

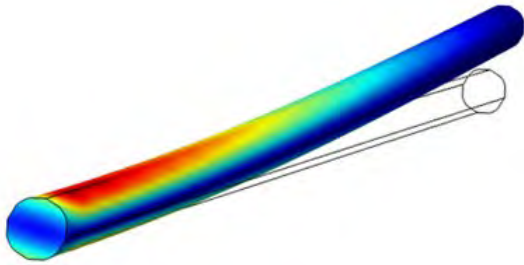


Figure 6 – Shows the nanofiber fixed at the base and displaced at the top when stimulated at the audible frequency range.

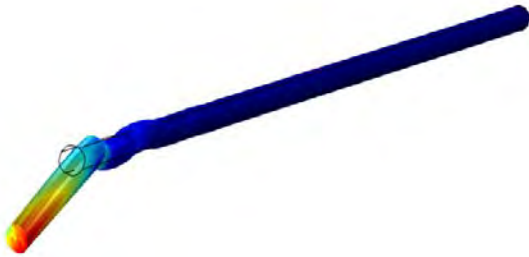


Figure 7 – Shows the nanofiber displaced at the base when stimulated at the audible frequency range.

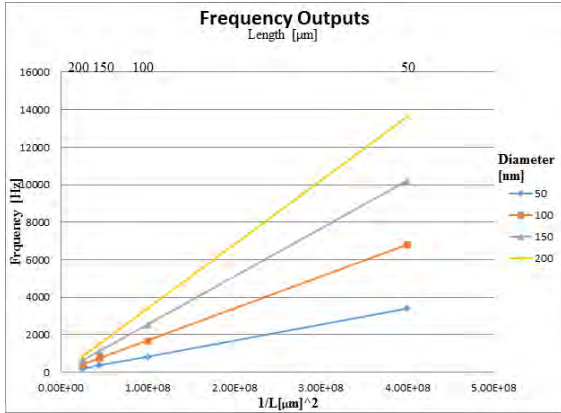
RESULTS AND DISCUSSION

Frequency output from COMSOL

I used COMSOL to simulate the cylindrical cantilever and I was able to obtain the frequencies at different dimensions.

Table 1 – This table shows the frequencies obtained from COMSOL at different dimensions.

3D Cylindrical Cantilever				
	Diameter [nm]			
Length [μm]	50	100	150	200
50	3403.2 Hz	6811.1 Hz	10221 Hz	13633 Hz
100	834.72 Hz	1701.7 Hz	2553.3 Hz	3405.5 Hz
150	379.74 Hz	755.18 Hz	1133.9 Hz	1512.6 Hz
200	182.06 Hz	415.93 Hz	635.99 Hz	850.89 Hz



Graph 1 – Shows the frequency output from COMSOL of the cylindrical cantilever with corresponding lengths and diameters.

Table 1 and Graph 1 show the different frequency outputs at different lengths and widths. Each solid line in the graph represent different diameters ranging from 50 to 200 nm. Each point belongs to its corresponding frequency with its respective length and diameter.

Frequency output from equation

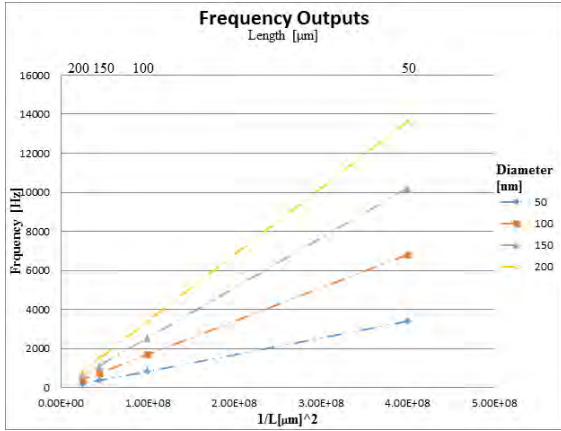
We were also able to derive an equation and use this equation to analytically verify the frequencies that were obtaining from COMSOL. The equation for frequency for a cylindrical cantilever is:

$$f = \frac{1.875^2}{8 * \pi} \left(\sqrt{\frac{E}{\rho}} \right) \left(\frac{d}{L^2} \right)$$

where E is the Young’s Modulus of $2.5974e^9$ GPa, ρ is density of $1.78g/cm^3$, d is the diameter, and L is the length.

Table 2 - This table shows the frequencies obtained from the equation at different dimensions.

Cylindrical Cantilever				
	Diameter [nm]			
Length [μm]	50	100	150	200
50	3404.9 Hz	6814.6 Hz	10226.2 Hz	13639.9 Hz
100	835.1 Hz	1702.6 Hz	2554.6 Hz	3407.2 Hz
150	379.9 Hz	755.6 Hz	1134.5 Hz	1513.4 Hz
200	182.2 Hz	416.1 Hz	636.3 Hz	851.3 Hz



Graph 2 – Shows the frequency output from the equation of the cylindrical cantilever with corresponding lengths and diameters.

Table 2 and Graph 2 show the different frequency outputs at different lengths and widths. Each dotted line in the graph represent different diameters ranging from 50 to 200 nm. Each point belongs to its corresponding frequency with its respective length and diameter.

Further work needs to be done in COMSOL to obtain the frequency when the fiber is submerged in a liquid and analyze how it reacts and how the frequency varies when it is not submerged and when it is.

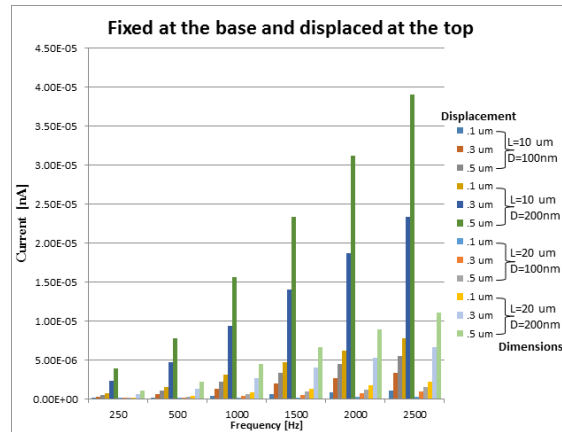
To obtain the current I simulated two different models. One model was fixed at the base and displaced at the top and the other model was just displaced at the base.

Each model was stimulated at the audible frequency range and displace at .1, .3, and .5 μm.

To obtain the current I simulated two different models. One model was fixed at the base and displaced at the top and the other model was just displaced at the base. Each model was stimulated at the audible frequency range and displace at .1, .3, and .5 μm.

Current output: Cylindrical cantilever fixed at the base and displaced at the top

By using COMSOL I was able to obtain the current from the fiber when stimulated at the audible frequency range of 250 – 2500 Hz.

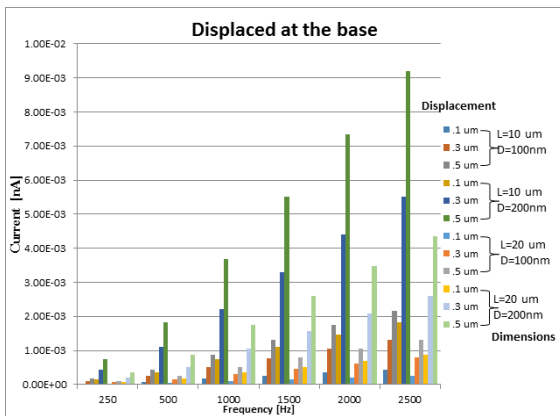


Graph 3 – Shows the current at different frequencies and we are able to see that the dimensions with high current are those with length of 10 μm and diameter of 200 nm. There is a high current when the

displacement is at $.5 \mu\text{m}$.

Current output: Cylindrical cantilever displaced at the base

By using COMSOL I was also able to obtain the current from the fiber when displaced at the base and stimulated at the audible frequency range of 250 – 2500 Hz.



Graph 4 – Shows the current at different frequencies and we are able to see that the dimensions with a significant high current are those with length of $10 \mu\text{m}$ and diameter of 200 nm. There is also a great increase in current when the displacement is at $.5 \mu\text{m}$.

CONCLUSION

After deriving the frequency equation of a cylindrical cross section to analytically verify the frequencies that I was obtaining from COMSOL, I am able to determine that the frequencies are correct. With this equation we are able to plug in

any diameter and length and get the frequency for each respective dimension.

That is to say, that instead of using COMSOL to simulate the response frequency for each dimension, we can now use the equation that I derived to estimate the frequency output that will send an electrical signal to the brain in the audible frequency range of 250 – 2500 Hz. Also after simulating two different models of the fiber, one which was only displaced at the base and the other fixed at the base and displaced at the top, I can conclude that the dimensions with the largest current response are those with a length of $10 \mu\text{m}$ and a diameter of 200 nm with a displacement of $.5 \mu\text{m}$.

ACKNOWLEDGEMENT

I would like to acknowledge Dr. Carlos R. Perez for helping me through the process of simulating using COMSOL and Dr. Santiago Aviles for the general supervision of the research group. Also this research was accomplished with the help of the SUNFEST REU program through the sponsorship of NSF.

Work Cited:

- 1) "Benefits and Applications." National Nanotechnology Initiative. NANO.gov, n.d. Web. 06 June 2015.
- 2) "Hearing Loss." Causes. Mayo Clinic Staff, 05 Sept. 2014. Web. 06 June 2015.
- 3) Reilly, Charles, and Sen Qi. "Snapshot of deaf and hard of hearing people, postsecondary attendance and unemployem." (2011): 6. Web. 27 June 2012.
- 4) "Cochlear Implants." National Institute of Deafness and Other Communication Disorders. U.S. Department of Health & Human Services, 01 Aug. 2014. Web. 27 June 2015.
- 5) Dwivedi, A. Conducting Polymer Electrodes on 'PVDF' Substrate for ElectroAcoustic Application in Cochlear Implants. (Thesis). (2003). Web. 27 June 2015
- 6) Frei, Walter. "Improving Your Meshing with Partitioning." COMSOL Blog Improving Your Meshing with Partitioning Comments. 27 Mar. 2015. Web. 20 July 2015. <<https://www.comsol.com/blogs/improving-your-meshing-with-partitioning/>>.
- 7) Griesmer, Andrew. "Automatic Meshing for Electromagnetic Simulations." COMSOL Blog Automatic Meshing for Electromagnetic Simulations Comments. 9 Dec. 2014. Web. 20 July 2015. <<https://www.comsol.com/blogs/automatic-meshing-for-electromagnetic-simulations/>>.
- 8) Frei, Walter. "Solutions to Linear Systems of Equations: Direct and Iterative Solvers." COMSOL. 11 Nov. 2013. Web. 20 July 2015. <<https://www.comsol.com/blogs/solutions-linear-systems-equations-direct-iterative-solvers/>>.
- 9) Gonzalez Sanchez, Juan. "Study of Nanofibers Formed by Magnetic Field Assisted Electrospinning Using Solutions Containing PVDF, DMF, Acetone and Fe3O4 Nanoparticles." (2015): 122. Print.
- 10) Lopez-Hallman, Raymond. "Electrospinning Process with a Moving Platform and PVDF as a Piezoelectric Transducer." (2014): 13. Print.
- 11) "Mechanical Engineering: IIT GUWAHATI Virtual Lab." Mechanical Engineering: IIT GUWAHATI Virtual Lab. 2015. Web. 5 July 2015. <<http://iitg.vlab.co.in/?sub=62&brch=175&sim=1080&cnt=1>>.

Graphene-BN Heterostructures: An In-Plane Transistor

Alexander Hunt IV (University of Pennsylvania and Material Science and Engineering),
SUNFEST Fellow

Professor A.T. Charlie Johnson, University of Pennsylvania Physics & Astronomy
Department

Abstract-- Graphene-Boron Nitride (G-BN) heterostructures can lead to the realization of nanoscale electronics that will be smaller than the dimensional limit—14 nanometers—of silicon transistors and provide higher mobilities. However, the graphene-boron nitride heterostructure although self-insulating, cannot function as a transistor alone due to not having a second conducting pathway. Thus, the utilization of the graphene-boron nitride heterostructure within a side gated FET would require two G-BN flakes to randomly nucleate together. In contrast, the growth of a graphene ribbon around the BN ribbon if fabricated, would allow for a single flake to act as a side gated FET. In order to grow such a G-BN-G heterostructure, the hydrogen etching of BN at high processing temperature must be overcome, which means the use of methane as a carbon precursor for graphene growth is no longer a viable option. As a result, benzoic acid will be studied in the following report as a potential carbon source to synthesize the outer graphene ribbon due to its low thermal breakdown temperature with present showing that hydrogen etching of BN has been reduced.

I. INTRODUCTION

The graphene field effect transistor (FET) has gained a lot of attention over the recent decade for its high carrier mobility—the ease with which electrons can flow through the crystalline lattice due to its honeycomb lattice, effectively reducing the collision and scattering rates between conducting electrons and fixed carbon atoms. This high mobility along with graphene being a two dimensional atomically thin material has led to the conclusion that graphene could replace the silicon transistor in future nanoscale sensors and circuits because lithographic patterning is reaching its miniaturization limit. However, in order for graphene to truly replace silicon as the transistor material of choice, graphene must be engineered in a way that converts the zero bandgap semiconductor into a true semiconductor with a distinct bandgap. This will allow graphene to have a distinct on and off state within its electronic structure, which is the basis for modern binary coding and memory storage.

Therefore, researchers have begun to look into graphene nanoribbons because theorists have shown that by using density functional analysis, graphene will develop a bandgap when the cross sectional width approaches length scales beneath ten nanometers [1]. At such small length scales, any charge traps at the interface between graphene and

silicon dioxide will greatly reduce the carrier mobility of the graphene ribbon therefore boron nitride—a 2-D atomically thin large bandgap dielectric—is currently being studied as an eventual replacement of silicon dioxide as the transistor gating material. Boron Nitride—a structurally and chemically compatible material to graphene—has a complete valence shell due to the ionic bonding between the boron and nitrogen atoms that make up its honeycomb lattice, which means that it has no charge traps [2] due to dangling bonds like silicon dioxide. This has led to the formation of the Graphene-Boron Nitride (G-BN) heterostructure that can serve as a template for the possible chemical vapor deposition (CVD) of a graphene ribbon around the boron nitride ribbon.

The main obstacle for the realization of this outer graphene ribbon is the hydrogen etching reaction of BN at temperatures exceeding 800°C [3]. This eliminates the most common carbon source for graphene growth, which is methane, because its thermal decomposition requires temperatures in excess of 1000°C at atmospheric pressure. Thus, the primary objective of my research is to design CVD growth parameters that test the viability of benzoic acid whose pyrolytic composition temperature is 550°C [4] as a potential carbon source that may allow the growth of the graphene ribbon without the adverse hydrogen etching of the boron nitride ribbon template.

II. Background

3.1 Graphene-Boron Nitride Interface:

The coupling of graphene to its isostructural insulator, boron nitride, results in an interfacial structure that has an equivalent electronic structure to that of the bandless semiconductor, graphene. This is the result of an edge potential that arises from

bonding the respective atoms of both structures together. In order to form the G-BN heterostructure, boron nitride's atoms at the interface have to exchange electrons with the carbon atoms of graphene either by accepting (forms stable bonding states) or donating (forms unstable antibonding states) electrons. This phenomena is determined by which atom the edge terminating carbon atoms of graphene bind to within boron nitride. If it is a boron to carbon terminating bond, then a full bonding state will occur, but if the terminating bond is carbon to nitrogen, then an antibonding state will appear [5]. This mix of bonding states at these interface produces the aforementioned edge potential that bends the discreet valence and conduction bands that initially arises within graphene from the quantum confinement of the G-BN edge states to a common point fixed at zero electrons volts, which is the Dirac point of pristine graphene with zigzag edges [6]. Therefore, the crystallographically aligned boron nitride ribbon with that of its graphene template cannot form a bandgap within graphene. The BNRs can however protect the sensitive edge states of graphene through passivation, which preserves the graphene edge states within its wide band gap.

3.2 Graphene Nanoribbon Bandgap Theory:

Due to the cross sectional width of graphene nanoribbons having to approach length scales beneath 10 nanometers in order for a bandgap to appear [1] within their electronic structure, their edge geometry—orders of magnitude larger—will dramatically affect both the mechanism by which the bandgap develops and the width of the resulting bandgap. Current theories on bandgap formation and size are based on density functional analysis, which utilizes the zigzag and armchair edge geometries of hexagonal graphene flakes and full graphene sheets

to center the computational calculations. The current model of zigzag graphene nanoribbons (ZGNRs) depicts bandgap formation as a result of the staggered sublattice potential that is created from the magnetic ordering of the electrons. In contrast, a nanoribbon of armchair edge geometry (AGNR) will develop a bandgap from the effects of quantum confinement and increased electron transfer between the edge atoms from atomic bonding length changes [6]. The important feature of such bandgap formation mechanisms is that the width of the bandgap is dependent upon the cross sectional width of the nanoribbon because of quantum confinement effects. For example, the bandgap increases and oscillates with a decrease in nanoribbon width for zigzag and armchair graphene nanoribbons respectively [7]. This allows for tunable bandgap transistors or diodes made of semiconducting graphene nanoribbons that could eventually lead to nanoscale circuitry and sensors.

3.3 Hydrogen Etching Reaction

Although both graphene and boron nitride prefer to attach to the edges of one another before nucleating on the exposed copper surface [5], both materials are highly susceptible to anisotropic—directional dependent—hydrogen etching at temperatures below their normal growth temperatures using methane and ammonium borane as their respective precursors. Anisotropic hydrogen etching occurs by reversing the growing reaction using residual atomic hydrogen to cleave the carbon-carbon bonds of graphene and the boron-nitrogen bonds of boron nitride to regenerate precursory compounds such as methane, BH_x and NH_x . For graphene, the most efficient hydrogen etching takes place at temperatures near 800°C with a steady decline in the percent area etch for temperatures that either exceed or fall beneath this optimal zone [8]. This drop off in

graphene etching efficiency at lower temperatures is the result of not having enough energy to overcome the activation barrier needed to break the carbon bonds of the zigzag edge while the exothermic nature of this hydrogen etching reaction would make exceedingly high temperatures unfavorable for this reaction.

In contrast, the hydrogen etching of boron nitride at temperatures lower than 900°C occurs mainly along crystal edges and grain boundaries. When temperature reaches above 950°C , a significant amount of anisotropic etching can now occur within the interior of boron nitride crystals, which results in the formation of triangular etched holes along the zigzag direction [3]. The hydrogen etching reaction that occurs in both materials is dependent upon the copper substrate because it allows for atomic hydrogen to adsorb and diffuse into the crystal centers and interfaces of the graphene-boron nitride heterostructure. Thus, the realization of a continuous graphene-boron nitride-graphene nanoribbon heterostructure will be unattainable if the growth substrate material and growth temperature do not reduce this hydrogen etching effect significantly.

IV. Materials and Methods

4.1 Atmospheric Pressure Chemical Vapor Deposition

Chemical vapor deposition (CVD) utilizes the pyrolytic decomposition of compounds to expose their constituent atoms to a metal substrate that catalyzes the reordering of the atoms into complex nanomaterials of various single crystalline geometries. These pyrolytic decomposition reactions often occur at temperatures in excess of 500°C in order to supply enough thermal energy to break the atomic bonds of the compounds within the precursor gas. Atmospheric pressure (760 torr) CVD is utilized

over low pressure (1 mtorr) CVD for single crystal growth of graphene and boron nitride due to highly reproducible hexagonal and triangular morphologies that are seen respectively when grown under atmospheric pressure compared to the irregular flowerlike shape grains associated with low pressure CVD growths [5]. The well aligned edge structure of both graphene and boron nitride individual grains will prove beneficial in their utilization as templates for growing boron nitride ribbons and graphene ribbons that will assume their crystallographic orientations. The general CVD setup used in the lab is a horizontal tube wall furnace that flows gases through a one inch quartz tube that can be heated up to 1100°C by external wall heaters. The gas flows are controlled by programmable flow controllers that release carrier gases—gases that facilitate the movement of sublimated solid or bubbled liquid precursory gases through the system—or precursor gases themselves at flow rates of standard cubic centimeter per minute (sccm). The unwanted byproducts of the thermal decomposition of the precursors are carried off into an external exhaust system in order to avoid exposure to harmful gas compounds such as carbon monoxide.

4.2 Methane

Methane will be used for the initial hexagonal graphene flake because its thermal breakdown at temperatures in excess of 1000°C is well defined within the field of chemical vapor deposition growth of 2-D atomic graphene. Methane (CH_4) decomposes as series of four dehydrogenation events on the surface of the copper substrate, which involves the cleavage of a single hydrogen by overcoming a one to two electron volt activation barrier each time. This requires a lot of thermal energy and is not energetically favorable

consequently the partially dehydrogenated species will reconnect with each other before complete dehydrogenation of methane to create intermediate hydrocarbon species such as C_2H_2 [9]. These intermediate hydrocarbon species require less energy to form on the copper surface compared to CH dissociation and act as the nucleating species for surface limiting graphene growth on the copper surface. Hence, the initial hexagonal graphene ring will be grown from a methane precursor in order to have a high crystallinity with sharply defined edge structure to ensure that the boron nitride will grow with a uniform crystallographic orientation from this graphene template.

4.3 Ammonia Borane

The boron nitride ribbon precursor will be ammonia borane (NH_3BH_3), which is an air stable solid derivative of borazine. Ammonia borane has a high BN content (80.4 wt. %) that upon thermal dehydropolymerization at temperatures exceeding 60°C reduces to borazine and aminoborane [10]. These compounds can then absorb on the copper surface where another thermally induced polymerization event takes place to generate polyborazylene at 600°C. Polyborazylene is then further dehydrogenated to form thin films of hexagonal-BN at temperatures greater than 700°C [10]. In the experimental CVD process, both the thermally activated polymerization and dehydrogenation occur at the same time since boron nitride is grown at either 1030°C or 1057°C, which can leave residues of non-reacted polyborazylene on the copper surface. However, the amount of polyborazylene on the copper surface will only be trace amounts since the boron nitride growth temperature far exceeds the limit to convert polyborazylene into crystalline hexagonal-BN that

take the form of triangles when grown via atmospheric pressure chemical vapor deposition (APCVD).

4.4 Benzoic Acid

Pyrolytic decomposition of organic compounds such as benzoic acid involves using thermal energy to break the bonds within their chemical structure to acquire smaller molecules such as CO₂ and shorter chained/ringed organic molecules such as benzene. Upon heating up benzoic acid past 550°C, a complete decarboxylation—removal of carbon dioxide—in vacuum occurs within ten minutes if the sample mass is approximately 3.6 mg [4] yielding one benzene molecule based on the stoichiometry of the proposed decarboxylation reaction. The now exposed benzene can be further broken down by dehydrogenation—removal of molecular hydrogen—reactions near the copper surface that acts as the catalysis for the surface limiting growth of graphene. However, the CO₂ secondary product of the pyrolytic decarboxylation of benzoic acid has been found [11] to etch away exposed boron nitride at process temperatures in excess of 900°C. This carbon dioxide etching reaction occurs due to the stronger electronegative oxygen ion pulling away the positively charged boron ion from its ionic bond with nitrogen in order to form boron trioxide, carbon monoxide, and molecular nitrogen. As a result, if graphene growth from benzoic acid can occur at temperatures below 800°C, then the boron nitride will not be etched away by either the carbon dioxide byproduct or by molecular hydrogen that is flown into the system in order to prevent the oxidation of the copper foil by trace oxygen impurities within the argon carrier gas.

4.5 APCVD Growth Recipes

In order to look at the interplay between the carbon dioxide etching reaction and the hydrogen etching reaction of the graphene-BN heterostructure during the growth of a possible third graphene ribbon grown from a benzoic acid precursor, a continuous and discontinuous growth of all three rings were designed and tested. A continuous growth without a cooling period between the formations of the boron nitride ribbon at temperatures exceeding 1000°C and the graphene ribbon around 800°C would be carbon dioxide etching dependent because the hydrogen would be used to facilitate the new graphene growth on the copper surface. However, a discontinuous growth with a cooling period in between boron nitride growth and the later graphene growth using benzoic acid will be hydrogen etching dependent since no carbon dioxide is being produced until the growth temperature is below the carbon dioxide etching temperature.

To test the nature of both growth mechanisms, the initial hexagonal graphene flake and boron nitride ribbon growths were kept constant while the cooling period—no benzoic acid flow into the system—was adjusted over a set of time intervals from 0 to 300 seconds as the system was cooled down to 800°C for a benzoic acid graphene growth period of ten minutes that started when benzoic acid was introduced into the system. The initial hexagonal graphene flakes were grown under a reduced nucleation environment due to exposing the copper foil to oxygen impurities within the 500 sccm (standard cubic centimeter per minute) argon gas flow up to 950°C without the presence of hydrogen gas [12]. This reduced nucleation in the graphene flakes will allow for the surface area needed to grow the boron nitride ribbon and possibly a subsequent

graphene ribbon from the exposed edges of the individual hexagonal graphene grains.

After reaching 950°C, the copper foil was annealed for 30 minutes at 1057°C under a flow of 500 sccm Ar and 30 sccm H₂, which prevented any further oxidation of the copper foil. Methane was then allowed to enter the CVD system at a minimal flow rate between 1.75 and 2 sccm for a ten minute growth period keeping both the hydrogen and argon flow rates fixed at 30 and 500 sccm respectively. Once the 10 minute methane graphene growth period was completed, a magnetic holder containing an ammonia borane pellet was slid to a heat zone—7.7 centimeters away from the furnace—from a cool zone—17.5 centimeters away from the furnace. This initiated the growth of hexagonal boron nitride by sublimating the ammonia borane pellet within the temperature range of 60°C to 70°C. The first two minutes of the five minute growth period involved preannealing the ammonia borane pellet under a flow of 1.75 sccm CH₄, 500 sccm Ar, and 30 sccm H₂ in order to ensure the formation of a sharp interface between the graphene flake and boron nitride ribbon [5]. After the two minute preanneal, the CH₄ was shut off and the hydrogen flow rate was reduced to 20 sccm for the final three minutes of the boron nitride ribbon growth period. The procedure at this point then changes based on the cooling down period described above to test the effects of the carbon dioxide etching reaction due to an early exposure of benzoic acid at temperatures above 900°C and the hydrogen etching reaction due to a late exposure of benzoic acid at temperatures below 900°C. The hydrogen flow rate remained fixed at 20 sccm till the benzoic acid growth period where it was then raised back to 30 sccm to facilitate graphene growth on the copper surface.

4.6 Microscopic Analysis

Once the growths used to test the generation of a graphene-boron nitride-graphene heterostructure by varying the temperature at exposure of benzoic acid into the CVD system were finished, the resulting product was analyzed using a combination of optical and atomic force microscopy on copper foil. Standard optical microscope images—micron resolution—were able to show if graphene and boron nitride had been produced due to the optical contrast that resulted from oxidizing the exposed copper foil regions on a hot plate set to 200°C. The regions that are not covered by either graphene or boron nitride would turn red under oxidizing conditions while the protected regions that are covered by one of the two aforementioned materials would appear white.

Atomic Force Microscopy (AFM)—nanometer resolution—was then utilized to check for the development of a third graphene ring by using the phase image that was produced by scanning over the surface of the G-BN-G heterostructure. The phase image monitors the phase lag between the signal that drives the cantilever within the AFM to oscillate and the cantilever output signal [13], which is effected by the elasticity, adhesion, and friction of the material surface. Graphene, boron nitride, and copper will produce different colors within the phase image based on the different phase lags that results when the cantilever scans over their respective rings within the G-BN-G heterostructure.

V. Experimental Results

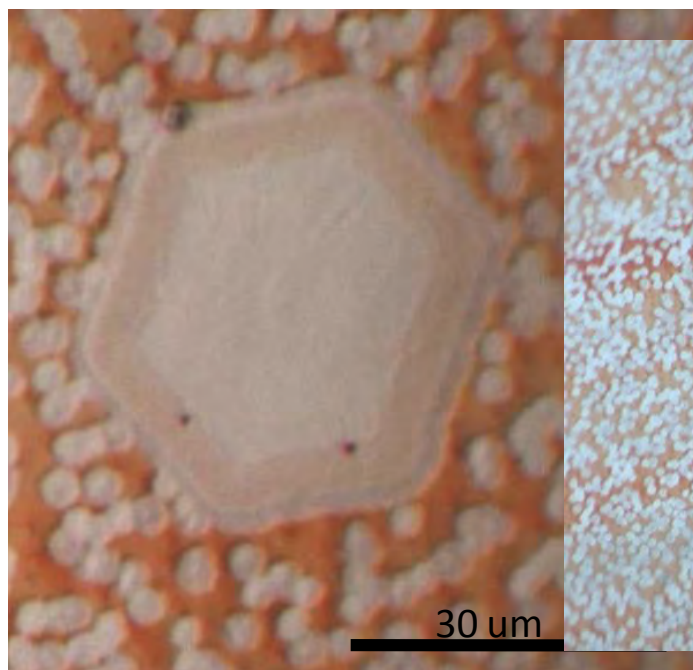


Figure 1: Optical Image of a Discontinuous Growth with a 300 second delay between Graphene Ribbon Growth and Boron Nitride Formation

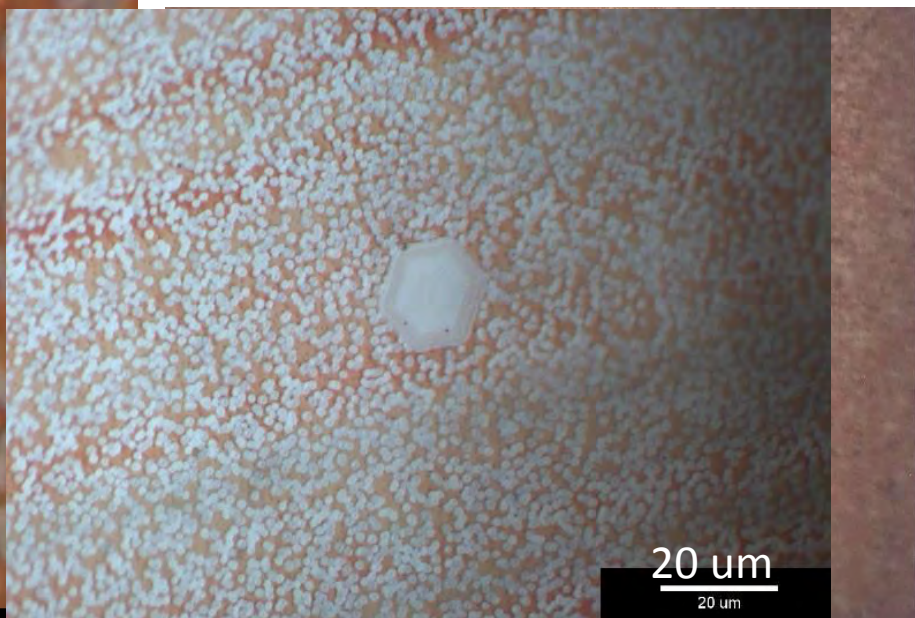


Figure 3: Optical Image at 20 μm zoom of a Continuous Growth with no delay between Graphene Ribbon Growth and Boron Nitride Formation

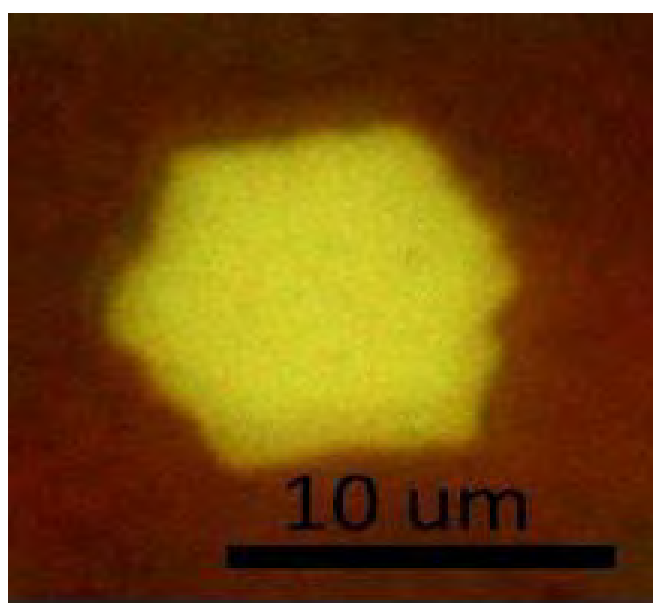
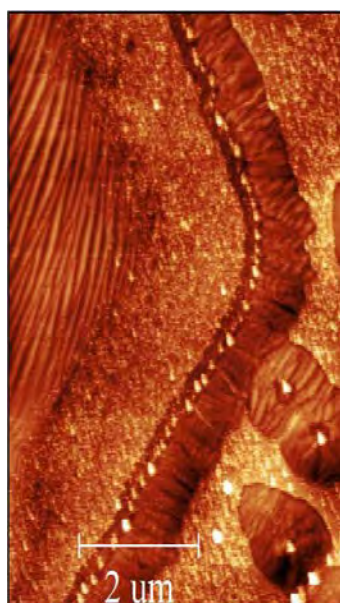
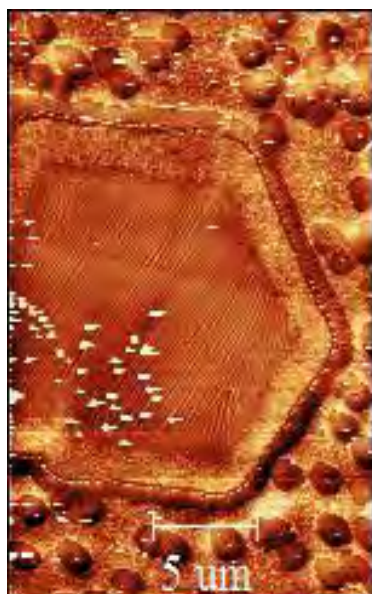


Figure 2a and 2b: AFM Z-Sensor (Height) Images of a Discontinuous Growth with a 300 second delay between Graphene Ribbon Growth and Boron Nitride Formation with the left image being a 30 um scan and right image being a zoomed in 8 um scan

Figure 4: Optical Image at 10 um zoom of a Benzoic Acid Precursor Grown Hexagonal Graphene Flake that occurred at a growth temperature of 875°C

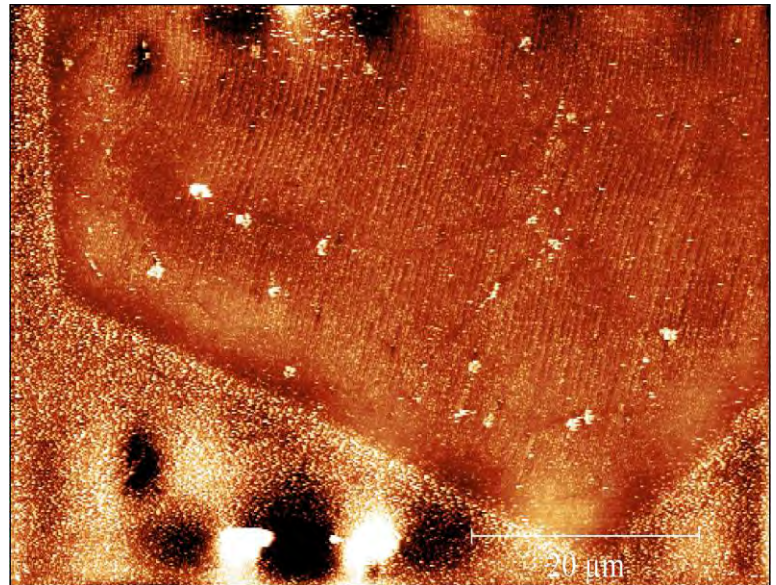
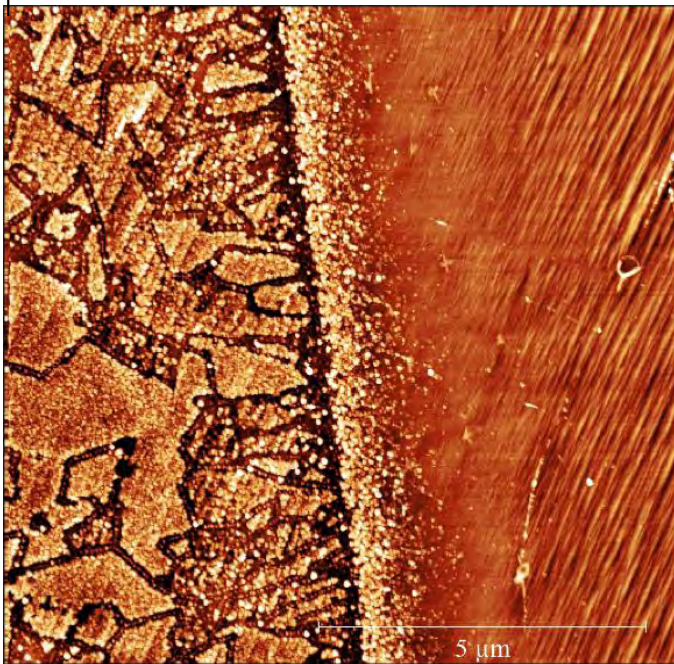
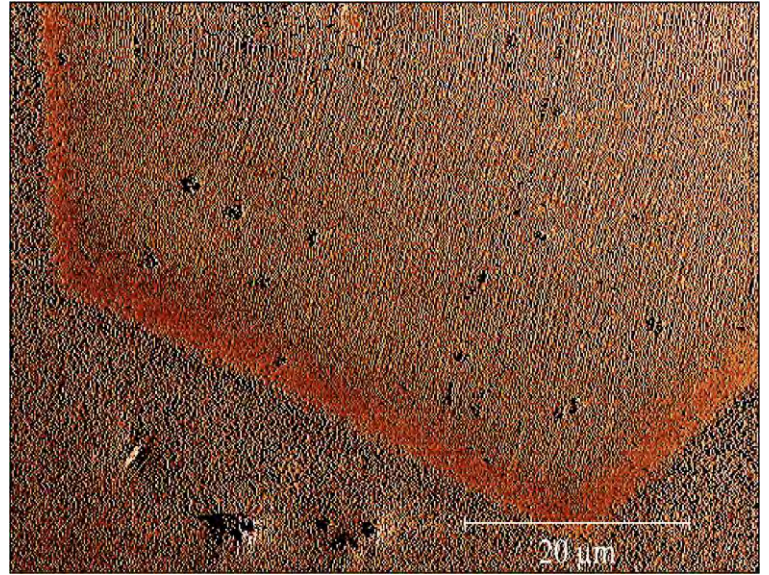
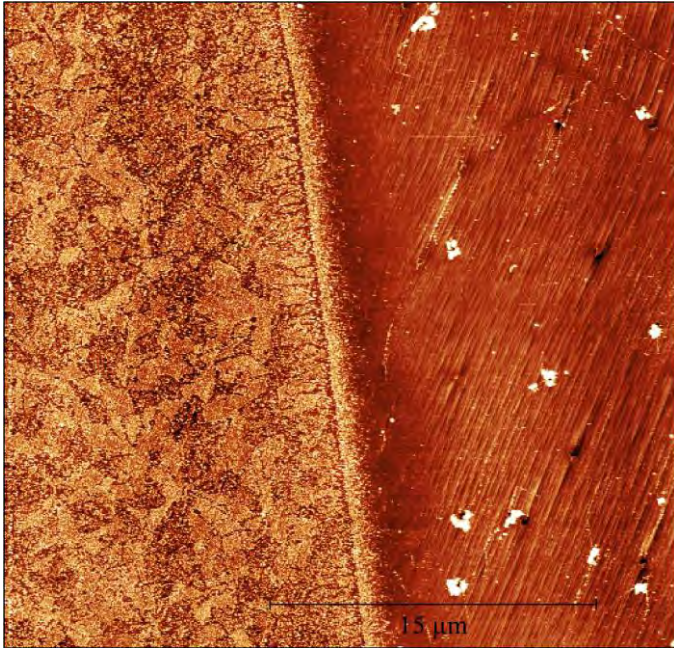


Figure 5a and 5b: AFM Z-Sensor (Height) Images of a Continuous Growth with no delay between Graphene Ribbon Growth and Boron Nitride Formation with the top image being a 30 um scan and the bottom image being a zoomed in 10 um scan

Figure 6a and 6b: AFM Images of a Continuous Growth grown from a second graphene flake with no delay between Graphene Ribbon Growth and Boron Nitride Formation with the top image being a 66 um Phase image and the bottom image being a 66 um Z-Sensor (Height) image

VI. Discussion and Conclusion

As we can see by the optical and AFM images, the discontinuous growth results in a discontinuity between the original graphene flake and the outer graphene ribbon while the continuous growth results in a nearly seamless transition between the rings without the loss of the boron nitride middle template. This could have been the result of the primary etching reaction in the discontinuous growth mechanism being hydrogen etching by molecular hydrogen that can diffuse more easily through the copper substrate and attack the original graphene-boron nitride interface. However, in the continuous growth the hydrogen gas is being used also to facilitate the growth of the benzoic acid graphene at high temperatures as a consequence, the primary etching reaction is now the carbon dioxide byproduct of the benzoic acid thermal decomposition. Carbon dioxide diffusion through the copper substrate is an order of magnitude lower than hydrogen, thus it is unlikely that enough CO_2 will be able to diffuse through the growing benzoic acid graphene and the boron nitride to the original boron nitride-methane graphene interface to attack it. The end result will be an intact graphene-boron nitride heterostructure with graphene grown on the expose substrate around it for the continuous growth of benzoic acid graphene after the boron nitride ribbon formation.

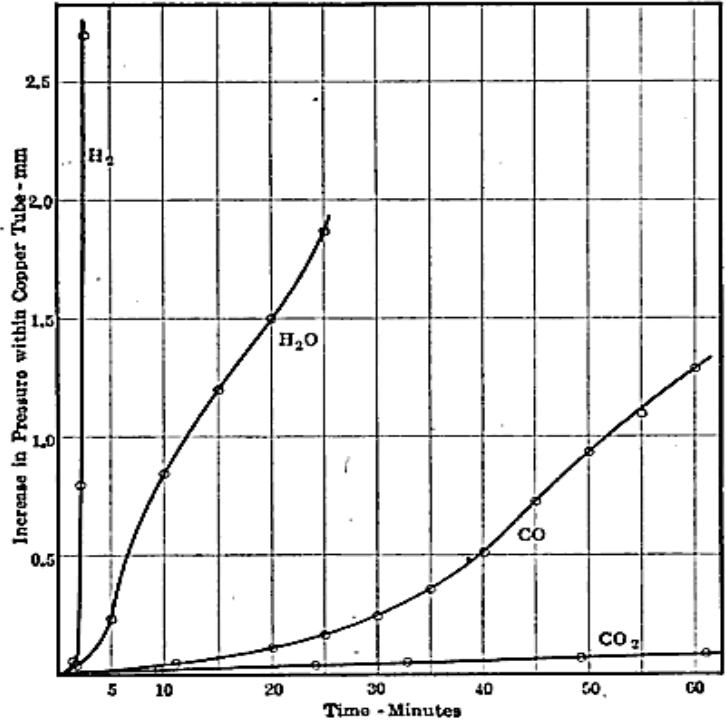


Figure 7: Diffusion of Hydrogen, Steam, Carbon Monoxide, and Carbon Dioxide through Copper at 700°C from Transactions of the American Institute of Mining and Metallurgical Engineers Copyrighted in 1919

VII. Acknowledgement

I would like to thank both Carl Naylor and Zhaoli Gao for their guidance throughout this project as well as the rest of the Johnson's lab members. I would also like to thank Professor A.T. Charlie Johnson for allowing me to work as a part of his research team this summer. In addition, I would like to acknowledge both Dr. Jan Van der Spiegel and Colleen Kennedy for their constant logistical support on upcoming events and preparation for the symposium. Finally, all the authors and I would like to acknowledge the support of the National Science Foundation, through NSF REU grant no. 1062672.

VIII. References

- 1) Jiao, Liying, Li Zhang, and Xinran Wang. "Narrow Graphene Nanoribbons from Carbon Nanotubes." *Nature* 458 (2009): 877-80. Print.
- 2) Dean, C. R., A. F. Young, and I. Meric. "Boron Nitride Substrates for High-Quality Graphene Electronics." *Nature Nanotechnology* 5 (2010): 722-26. Print.
- 3) Sharma, Subash, and Golap Kalita. "Opening of Triangular Hole in Triangular-Shaped Chemical Vapor Deposited Hexagonal Boron Nitride Crystal." *Nature: Scientific Reports* (2015): 1-9. Print.
- 4) Santrock, Jeffrey, and J. M. Hayes. "Pyrolytic Decarboxylation of Aromatic Acids as a Means of Isotopic Analysis." *Analytical Chemistry* 57.7 (1985): 1441-43. Print.
- 5) Han, Gang Hee, Nicholas J. Kybert, and Julio A. Rodriguez-Manzo. "Continuous Growth of Hexagonal Graphene and Boron Nitride In-Plane Heterostructures by Atmospheric Pressure Chemical Vapor Deposition." *ACS Nano* 7.11 (2013): 10129-38. Print.
- 6) Li, Xiaolin, et al. "Chemically Derived, Ultrasoft Graphene Nanoribbon Semiconductors." *Science* 29 Feb. 2008: 1229-31. Print.
- 7) Ilyasov, V. V., B. C. Meshi, and V. C. Nguyen. "Tuning the Band Structure, Magnetic, and Transport Properties of the Zigzag Graphene Nanoribbons/Hexagonal Boron Nitride Heterostructures by Transverse Electric Field." *Journal of Chemical Physics* 141 (2014): 1-5. Print.
- 8) Zhang, Yi, Zhen Li, and Pyojae Kim. "Anisotropic Hydrogen Etching of Chemical Vapor Deposited Graphene." *ACS Nano* 6.1 (2012): 126-32. Print.
- 9) Zhang, Wenhua, et al. "First-Principles Thermodynamics of Graphene Growth on Cu Surfaces." *Journal of Physical Chemistry* 115 (2011): 17782-87. Print.
- 10) Kim, Ki Kang, et al. "Synthesis and Characterization of Hexagonal Boron Nitride as a Dielectric Layer for Graphene Devices." *ACS Nano* 6.10 (2012): 8583-90. Print.
- 11) Gao, Teng, Xiuju Song, and Huiwen Du. "Temperature-Triggered Chemical Switching Growth of In-Plane and Vertically Stacked Graphene-Boron Nitride Heterostructures." *Nature Communications* 6 (2015): 1+. Print.
- 12) Gan, Lin, and Zhengtang Luo. "Turning off Hydrogen to Realize Seeded Growth of Subcentimeter Single-Crystal Graphene Grains on Copper." *ACS Nano* 7.10 (2013): 9480-88. Print.
- 13) Zang, Ling. "Basics of Atomic Force Microscopy (AFM)." U of Utah. Salt Lake City. 21 Oct. 2013. Lecture.

Design of a Wireless Power Transfer System for Wireless Sensor Networks in Biomedical Applications

Tim Kindervatter (TCNJ Electrical Engineering), *SUNFEST Fellow*

Jan Van der Spiegel, Electrical and Systems Engineering

Abstract—Analysis and design of a wireless power transfer system for application in a brain implant is presented. The design consists of three main stages: the power transfer stage, the power management stage, and the energy storage stage. RF energy harvesting and inductive charging are considered as viable alternatives for the power transfer stage. Quantitative analysis of each technique reveals that both solutions are viable, but energy harvesting sacrifices charging speed for mobility of the implantee during charge, and inductive charging does the opposite. The design for a power management system is shown, and two commercially available charge management chips available from Texas Instruments are compared. The surface mounted bq25100 chip is found to be the superior option.

Index Terms— Energy harvesting, Energy management, In vivo, Inductive charging, Implantable biomedical devices, RF signals

I. INTRODUCTION

Neural implants are a promising but nascent technology with many potential applications. They can detect and transmit signals produced by the brain or they can stimulate the brain by outputting electrical impulses. This allows researchers to study the brain in new ways. These neural implants require power to operate, but conventional wired power sources are not feasible for a number of reasons. The implantee would have wires coming out of their skull and they would be tethered to a power source whenever the implant needed to be recharged. Instead, researchers turn to a more elegant solution: wireless power.

Wireless power transfer (WPT) solves many of the aforementioned concerns regarding the neural implant. WPT systems are unobtrusive, and are able to constantly provide a small amount of power. This means that these systems are able to charge the implant continuously, so the implantee does not need to be conscious of setting time aside to recharge the implant. This is particularly useful for in-vivo experiments, because it allows the test subject to move freely while wearing a neural implant without worrying about the implant running out of power.

Researchers at the University of Pennsylvania desire a WPT solution for use in the Brain-Machine Interface project. One goal of this project is to stimulate the brain of a swimming rat to induce it to swim in a specific direction. This poses some unique design challenges to be considered in the design of a WPT system, such as size constraints and the need for waterproofing. This paper seeks to analyze several viable alternatives for wireless power transfer. Different systems will be compared quantitatively, and their strengths and weaknesses considered in the context of the Brain-Machine Interface.

II. BACKGROUND

This section covers the major components of a WPT system. Figure 1 shows a block diagram to help visualize the system.

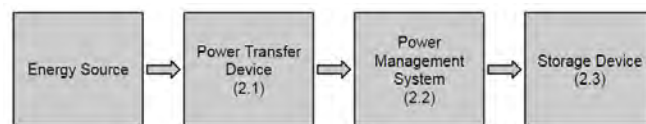


Figure 1: Block Diagram of Wireless Power Transfer System

2.1 Wireless Power Transfer Techniques

2.1.1 RF Energy Harvesting

Radio Frequency (RF) Energy Harvesting is accomplished by capturing RF radiation and converting it to DC power. RF signals are ubiquitous and plentiful in today's society [1]. Cell phones, WiFi routers, and radio stations are a few examples of RF sources. These sources emit RF signals in every direction, some of which are picked up by receivers and used to transmit information, and others which go unused, simply traveling and attenuating until they eventually disappear. RF energy harvesting seeks to capture these unused signals and harness their energy so it can be used to power devices.

An RF energy harvesting device consists of several components. In order to receive RF signals, an antenna must be used. Since these signals are sinusoidal in nature, they induce an alternating current. This alternating current is then passed through a rectifier, which converts it to direct current [1]. Additional circuit components may be included as well,

such as a voltage monitor, an amplifier, and matching circuits (circuits used to smoothly transition the signal from one component to the next). Commercially available hardware exists that includes many of these components on one small chip. This paper considers the Powercast P1110, an energy harvesting device designed for the 908 – 928 MHz range [2].

2.1.2 Inductive Charging

Inductive charging is based on the concept of electromagnetic induction. A coil of wire with current flowing through it will produce a magnetic field. Similarly, if a coil of wire is placed in a changing magnetic field, a current will begin to flow in the coil. A WPT system can be created using this concept by connecting one coil to a constant power source (such as a wall outlet or a DC power supply) and placing the second coil a short distance away from the first. The magnetic field created by the current in the first coil will in turn induce a current in the second coil, effectively transferring the power wirelessly [4]. Figure 2 demonstrates this phenomenon.

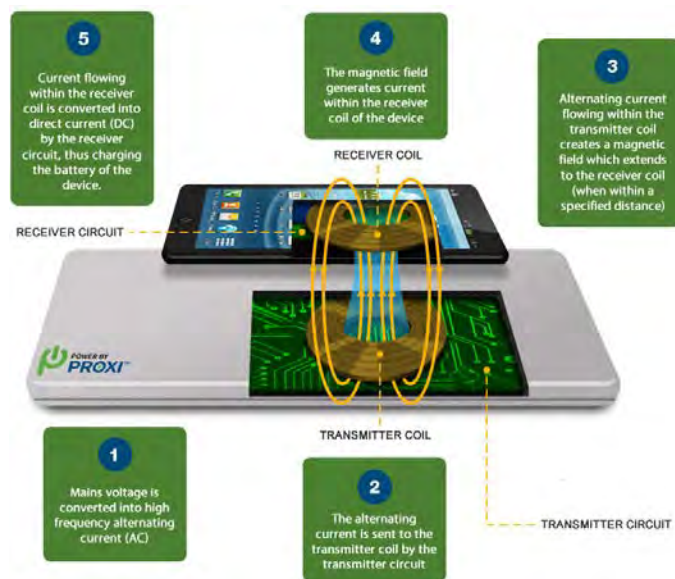


Figure 2: Diagram of an Inductive Charging System (adopted from [4])

As shown in figure 2, the current must be converted to alternating current (AC) before entering the coils. Once transferred to the second coil, the current must be rectified back to direct current (DC). Only a changing magnetic field can induce current in a coil; a static magnetic field is unable to do so [4]. Therefore, alternating current is used to induce a continuously changing magnetic field, which then creates an alternating current in the second coil, which must then be rectified before it can be used to power a device.

2.2 Power Management

A wireless power transfer system requires a power management stage to function properly. The purpose of power management is to automatically monitor and regulate the flow of power from the power transfer stage to the energy storage device. Without this stage in place, the power received by the

power transfer stage would be directly and perpetually provided to the energy storage device. Since energy storage technologies are very sensitive and can be easily damaged if not charged optimally, a power management system is designed with certain threshold values for parameters such as voltage, current, temperature, etc. If any of the parameters are outside an acceptable range, as defined by these threshold values, the power management system immediately terminates charging in order to prevent damage to the energy storage device.

2.3 Energy Storage Solution

It is rarely the case that the power received from an energy source will be exactly equal to the power consumed by a device at any given moment. Because of this mismatch, power ends up going to waste [5]. If less power is received than is demanded by the load, all of the received power goes to waste. If the power received exceeds the power consumed, the excess power goes unused, typically becoming heat, sound or vibrational energy. In these cases, a storage device is desirable for the unused energy, such as a battery. The energy stored in the battery can be accessed later, when it is required.

III. BENCH TEST SETUP

3.1 Powercast P1110 RF Energy Harvesting Chip

The P1110 chip was incorporated into a custom-designed Printable Circuit Board (PCB) with an SMA connector for RF input and six I/O pins for bench testing. Tests involving the P1110 were performed using a Fluke 6060A Synthesized RF Signal Generator. The signal generator was connected to the PCB via an 8" male to male SMA cable. This is solely for testing purposes. In the future, the signal generator will be replaced by an antenna, which will be incorporated into the final design.

3.2 Fluke 6060A Synthesized RF Signal Generator

This signal generator can be set to output at a given frequency and power. Output frequency can be set in the Hz, kHz or MHz ranges, with a maximum output frequency of 1050 MHz. The output power is measured in dBm and has a minimum step size of 0.1 dBm. The maximum power output is +13 dBm.

3.3 TDK WRM483245-15F5-5V-G Inductive Charging Coil

This is a commercially available inductive charging coil that includes a PCB that rectifies and conditions the output voltage. It accomplishes this through the use of a TI bq51013b wireless power receiver chip [6]. The output of the device is ~5V and 0.5 to 0.7A [7]. This is the receiver side coil of an inductive charging pair. A source coil is required to transmit the power. The source coil used in these experiments was a commercially available Qi compliant inductive charging mat. The charging mat was powered via USB connection.

3.4 TI Charge Management Chips

Two different Texas Instruments charge management

devices were considered for the power management stage of the wireless power transfer system. The bq2954 is a DIP package (through hole) device, and can be easily used with a breadboard for bench testing. The bq25100 is a surface mounted device with a much smaller profile, which is preferable for a final design. Both devices perform many of the same functions, with minor differences.

3.5 Lithium-Ion Battery

A lithium-ion battery is used as an energy storage device. Two batteries were used in tests, both with a maximum internal voltage of 4.2V. One battery had a capacity of 150mAh while the other had a capacity of 1200mAh. Wires were soldered onto the terminals of the battery, which allowed for easy attachment to different devices for charging and discharging.

IV. RESULTS AND DELIVERABLES

4.1 Energy Harvester vs. Inductive Charger

4.1.1 Charging Speed

Bench tests were performed with both the energy harvester as well as the inductive charging coils to see how long it took each of them to charge a lithium-ion battery. The energy harvester was given a 915 MHz signal at 10.0 dBm input power by a signal generator. The inductive charging coils were at minimum separation, with the receiver coil face down on the center of the power mat. A 1200mAh battery was used for both tests. The results of these tests are shown in Figure 3.

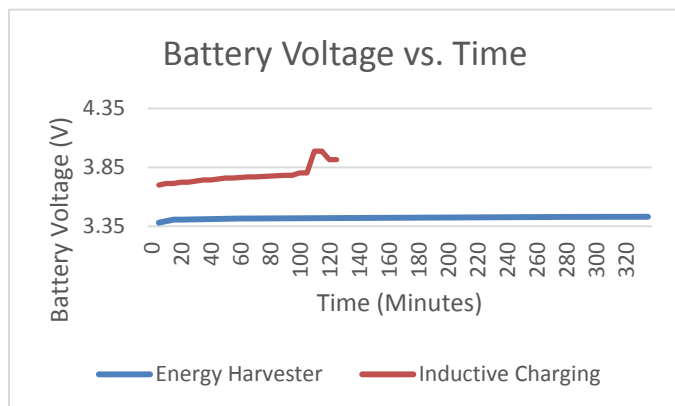


Figure 3: Charging Speed of Energy Harvesting vs. Inductive Charging

The inductive charging coils were found to charge the battery much faster than the energy harvester in this experiment. The inductive charger increased the voltage of the battery from 3.70 to 3.91V in 2 hours, a rate of about 0.105V/hr. The energy harvester increased the voltage of the battery from 3.38 to 3.43V in 5.58 hours, a rate of about

0.0089V/hr. These results are dependent on the charging current. The input power of the energy harvester is limited by the signal generator, so an antenna may be able to receive higher power signals that induce larger charging currents. Conversely, the inductive charging coils are operating at near-maximum performance due to their proximity. In practical applications, the coils may need to be farther apart, which would drastically reduce the amount of power they could transmit.

4.1.2 Mobility of Implantee

One of the most attractive aspects of wireless power transfer is the fact that it does not tether the implantee to a specific location during charging, which would restrict their movement and inhibit their daily activities. Not all wireless power transfer technologies have the same effective range, meaning that some will allow more freedom of movement for the implantee than others. Energy harvesting allows for nearly unlimited range of movement. An RF energy harvester can harness energy from tens of meters away [8]. One experiment tested the effective range of an RF energy harvester to be up to 1 mile away [9]. The only drawback to the energy harvester's range is that it is very sensitive to line-of-sight, meaning that it will not function well inside buildings, where there are many sharp angles and turns and few direct lines from one point to another.

In contrast to RF energy harvesting, inductive charging is very short-ranged. Power transfer drops off dramatically when the coils are separated by more than a few centimeters. This means that in terms of mobility, inductive charging offers almost no benefit over wires. This is especially problematic for testing of the brain implant, which is performed using animals like monkeys and rats. It will be very difficult to keep the animal stationary in a specific position in order to allow for effective charging using the inductive coils.

4.2 Power Management Stage

PCB designs were laid out in CadSoft Eagle PCB software.

4.2.1 bq2954 Circuit

Two designs were made; one included the TI bq2954 along with several through-hole components used for setting threshold values. The schematic is shown in Figure 4.

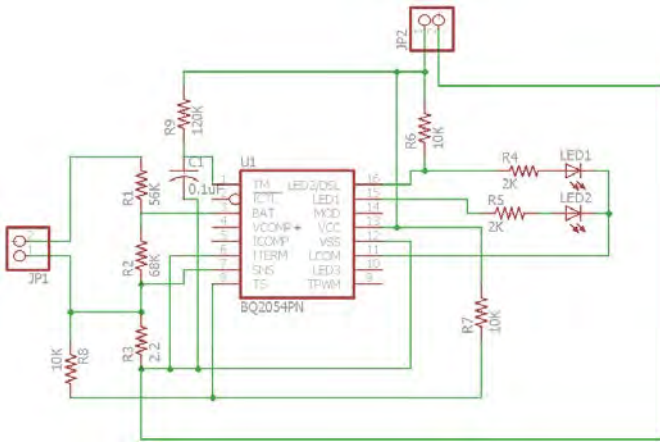


Figure 4: Power Management Stage Using Through-Hole Components

The bq2954 has an internal threshold value for maximum voltage set by the manufacturer. If this value is exceeded, the chip will terminate charging immediately. This internal threshold is set at 2.05V, but can be configured by the user to achieve a different threshold value. Resistors R1 and R2 form a voltage divider that can accomplish this. Equation 1 shows how values for R1 and R2 were obtained.

$$\frac{R1}{R2} = \frac{N * V_{cell}}{2.05} - 1 = \frac{1 * 3.7}{2.05} - 1 = 0.804 \approx \frac{4}{5}$$

$$R1 = \frac{4}{5} R2 \quad (1)$$

Similarly, the bq2954 has a maximum current threshold value. The chip will output this current to the battery during charging. The user can configure this current threshold by changing the value of R3. A charging current of 0.8 times the capacity of the battery is considered safe. This means that for a 150mAh battery, a charging current of 120mA is desired. Equation 2 shows how to achieve this using R3.

$$R3 = \frac{0.25V}{I_{max}} \quad (2)$$

R4, R5, R6, and the two LEDs form a charge indicator circuit, which indicates when the battery is charging, full, or disconnected. R7 and R8 are used to disable the temperature sensing function of the bq2954. R9 and C1 form a timeout circuit. This circuit sets an absolute maximum time for the charging cycle. This circuit results in a maximum timeout of 6 hours, as shown in equation 3.

$$t = 500 * R * C = 500 * (120K\Omega) * (0.1\mu F) \approx 6 \text{ hours}$$

4.2.2 bq25100 Circuit

The second PCB design incorporates the TI bq25100, which is roughly equivalent to the bq2954, but comes in a surface mounted package. This means that it is much smaller and more suitable for use in the BMI implant. The schematic for this design is shown in Figure 5. A custom library had to be created for the bq25100, since it was not included in the default Eagle libraries.

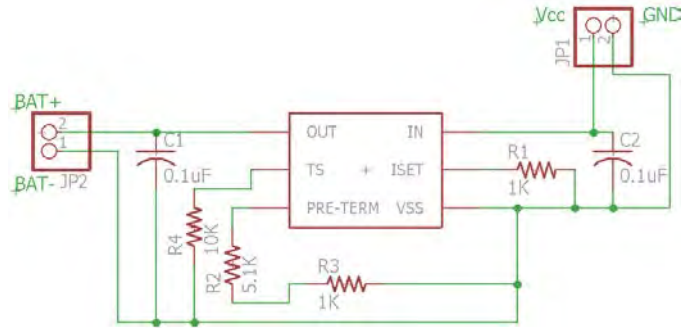


Figure 5: Power Management Stage Using Surface Mounted Components

R1 sets the charging current according to equation 4.

$$0.135V = R1 * I_{max}$$

Once the maximum voltage threshold (set to 4.2 in the bq25100) has been reached, the current will begin to drop. Once the current falls below a certain threshold, the battery is considered fully charged and current will terminate. R2 and R3 are used to set this termination current threshold. The expected range is 600Ω to 30kΩ. Values in this design were chosen based on availability of components in the lab.

R4 disables temperature sensing and C1 and C2 are bypass capacitors (also known as decoupling capacitors) used to isolate electrical noise and prevent it from affecting the operation of the rest of the circuit.

4.2.3 PCB Board Designs

The board layouts for the two designs are shown in Figures 6a and 6b.

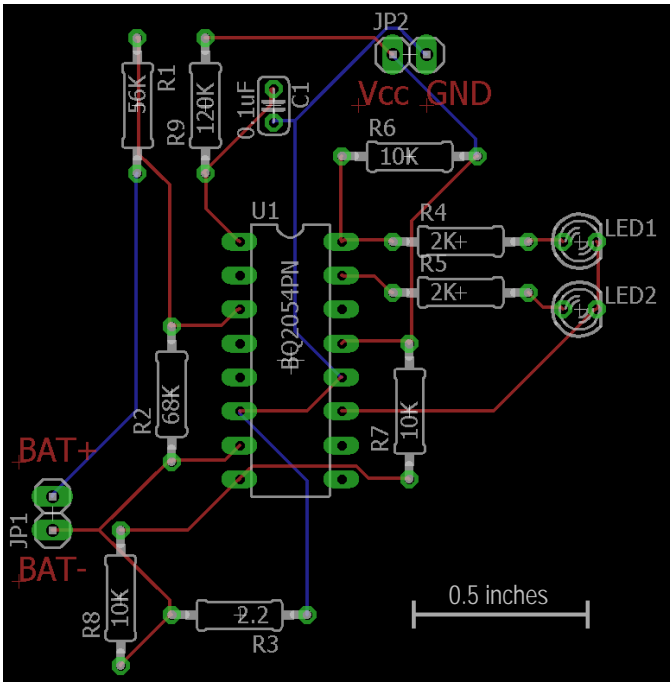


Figure 6a: Through-Hole Board Design

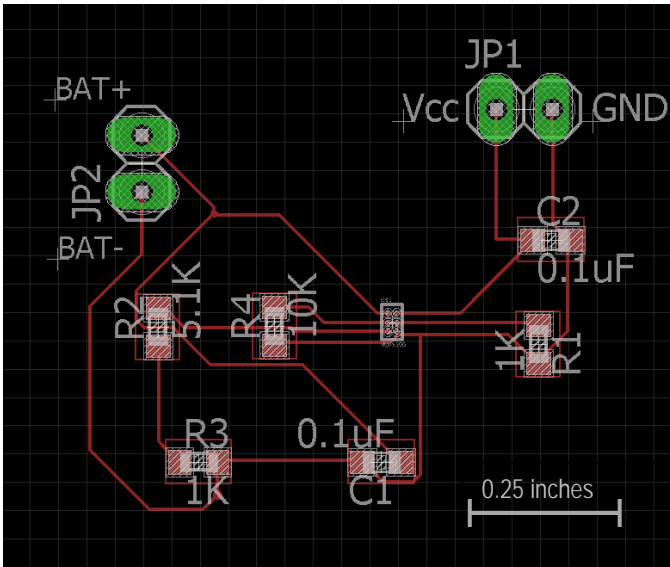


Figure 6b: Surface Mounted Board Design

V. CONCLUSION

RF Energy Harvesting and inductive charging both remain viable options for a wireless power transfer system. Energy harvesting does not require external hardware or time dedicated to charging, whereas inductive charging is dependent on proximity to an external coil. Both applications are very small and light, making them suitable for implant applications. In the experiment performed, the inductive coils charged the battery much more quickly than the energy harvester, but there are many factors that could affect this. Future testing should be performed under varying conditions to test the effectiveness of both methods.

The bq25100 is the most suitable solution for the power

management stage of the WPT system. It is very small, making it easily implantable, and there are fewer I/O pins, making it more streamlined and simpler to work with as compared to the bq2954.

ACKNOWLEDGMENTS

The author would like to acknowledge the support of the National Science Foundation, through NSF REU grant no. 1062672.

REFERENCES

- [1] Bouchouicha, D., et al. "Ambient RF Energy Harvesting." International Conf. on Renewable Energies and Power Quality (2010): n. pag. Print.
- [2] "Product Datasheet P1110 – 915 MHz RF Powerharvester™ Receiver." 2010. Digital file.
- [3] "Air Core Transformer." electrical4u.com. N.p., n.d. Web. 17 July 2015.
- [4] "Wireless Charging." powerbyproxi.com. N.p., n.d. Web. 17 July 2015 <<http://powerbyproxi.com/wireless-charging/>>.
- [5] Kansal, Aman, et al. "Power Management in Energy Harvesting Sensor Networks." ACM Transactions on Embedded Computing Systems (TECS) - Special Section LCTES'05 6.4 (2007): n. pag. Print.
- [6] "Highly Integrated Wireless Receiver Qi (WPC V1.1) Compliant Power Supply." Mar. 2013. File last modified on Oct. 2013. Digital file.
- [7] "Rx Modules WRM483245-15F5-5V-G." N.d. Digital file.
- [8] Le, Triet, Karti Mayaram, and Terri Fiez. "Efficient Far-Field Radio Frequency Energy Harvesting for Passively Powered Sensor Networks." IEEE Journal of Solid-State Circuits 43.5 (2008): 1301. Print.
- [9] Aminov, Parvizso, and Jai P. Agrawal. "RF Energy Harvesting." Electronic Components and Technology Conf. (ECTC) 64 (2014): 1. Print.

Cross-CUT Interference Present in Timing Extraction

Timothy Linscott (Seattle University, Computer Engineering), *SUNFEST Fellow*

André DeHon, Implementation of Computing Group

Abstract— Built-In Self Tests such as those developed by Wong, Sedcole, et al. [1] and Gojman [2] for measuring the internal path delays of a reprogrammable chip require maximizing isolation to eliminate interference between their components. This work demonstrates that placing anything more than a single measurement circuit on a chip at a time can influence the results of a measurement. The load placed on the clock by the measurement circuits is explored as a possible cause along with the ways that the different clock quadrants can be exploited to reduce the clock’s influence on the measurements. This work also begins characterizing the noise introduced by running Timing Extraction measurements in parallel and demonstrates how this noise can be minimized.

Index Terms— FPGA, Timing, Self-Measurement, Component-Specific Mapping, On-Chip Delay Measurement

I. INTRODUCTION

Field-Programmable Gate Arrays (FPGAs) are reconfigurable, general-purpose integrated circuits. They are divided up into Logic Array Blocks (LABs) that contain the basic components to create any given digital circuit. FPGAs are favored by many industries because the function of the hardware can be defined and then upgraded after it is installed. This eliminates the need for each new device to be custom-built in a lengthy and expensive fabrication process. FPGAs work by using only a fraction of the large numbers of paths in their LABs. As the number of components on an FPGA grows, the fitter software that maps the programmer’s circuit to the FPGA does not have enough information to do so optimally. When the logic is fitted poorly on an FPGA, excess heat is generated, path delays increase and the lifetime of the chip declines [3]. Additionally, the voltage transients from recently-used, nearby components, internal transistor leakage and electromagnetic interference from rapidly switching wires all contribute to timing delays in ways that simulation cannot accurately predict [4]. In order to provide the fitter with all the information needed to wire an FPGA optimally, we need to be able to both test the path delays in an FPGA and understand the effects that adjacent components have on each other’s speeds. Tools such as Timing Extraction help determine the effects of process variation and interference between circuits on an FPGA. However, these tools are themselves prone to interference since they are built from the very circuits they seek to measure. This work demonstrates the measurements taken in Timing Extraction are dependent on the number and relative location of timing circuits placed on a chip. It also describes configurations of multiple simultaneous experiments that have minimal effect on each other’s measurements.

II. BACKGROUND

A. Delay Built-in Self-Tests and Timing Extraction

Delay Built-In Self Tests (BIST) are techniques like those developed by Wong, Sedcole et al. [1] and further developed by Gojman [5] for finding delays on an FPGA. In Timing Extraction—the delay BIST developed by Gojman—the FPGA is decomposed into Discrete Units of Knowledge or DUKs—combinations of wires, logic and registers that make up paths on an FPGA. The Circuit Under Test (CUT) is a path defined by the chosen DUKs and is placed between a launch and a capture register driven by a clock signal. The components making up the path are then configured as buffers to allow the signal to pass unchanged, as shown in Figure 1.

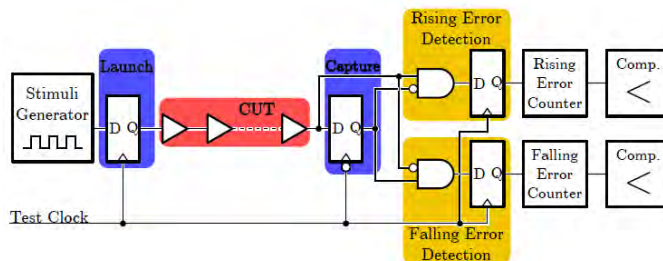


Figure 1. Diagram of a measurement circuit used in Timing Extraction.

When all of these components are fitted on the FPGA, they occupy three LABs in the Cyclone III architecture. When the BIST is run, the frequency of the clock is steadily increased until the contents of the launch and capture registers cease to match at the end of a clock tick half of the time. Half of the clock period—the amount of time the clock was at each voltage—is then said to be our path delay. In this way, we can find the path delay for both the rising clock transition and the falling transition [1]. When the path delays are known, they can be used to solve for the delays over each DUK to give us the chip’s delays at the finest possible granularity. To maximize precision, Timing Extraction is conducted in isolation. The FPGA controller is constrained to one side of the chip and the CUTs are kept as far apart as possible. Wong, Sedcole et al. ran the experiment with a 26x35 array of CUTs as well as with 52 sets of 16 CUTs [1] and Gojman placed 10 CUTs on the chip at a time [5]. Because measuring every path on an FPGA can be time consuming, Wong, Sedcole et al. and Gojman both recommended developing a parallel implementation of the BIST [1] [5].

B. Ring Oscillators

The ring oscillator is conceptually similar to the launch-and-capture model of Timing Extraction except that the ring oscillator follows a path of inverters rather buffers. Thus, it creates its own clock rather than needing to be supplied with

one. The oscillator is simply an odd number of inverters connected in a loop so that the output toggles between high and low at a predictable frequency. As with Timing Extraction, it can measure delays through internal logic and wires, but ring oscillators cannot measure over registers. These can be used as temperature sensors when the oscillator is primarily composed of transistors instead of wires. As the temperature rises, the transistor delay increases as given by Equation 2 and the frequency of the oscillator slows. Detection circuits can pick up the frequency changes and infer the temperature increase [4]. Because they are often implemented with a high number of inverters, the oscillator spans multiple LABs and makes for a good test of the overall temperature of an FPGA [6].

C. Self-Heating Effects

Whenever a path in an FPGA is used, it generates heat. The energy dissipated in a toggling wire is given by the equation:

$$E = \frac{\alpha_k}{2} V_{dd}^2 L C_k \quad (1)$$

Where α_k is the toggle rate, L is the wire length and C_k is the capacitance of the channel. We expect that this heat will spread over the chip proportionate to $1/r^2$ in accordance with basic physics. The current through the drain of a transistor I_d is proportionate to $e^{1/T}$ where T is the temperature in Kelvin. Since the drain current decreases with temperature, charge flows across the transistor slower. Because the transistor has a capacitance C , reaching a new voltage level V has a time delay T_d given by the following:

$$T_d = CV/I_d \quad (2)$$

Use of the wires and transistors in the FPGA generates heat which in turn decreases the amount of current that can flow through the transistors. Because less current can flow, the delays through the circuit increase since more time is needed to transition between voltage levels.

D. Thermal-Aware CAD

Thermal-Aware CAD attempts to incorporate these ideas of self-heating-induced delays into the routing and placement of components on FPGAs. Because using longer wires increases energy use, fitting software tends to place components as close together as possible. Because of the proximity, the components heat up and delays increase. Thermal-Aware CAD looks for a golden mean between energy use and heat control. Recent Thermal-Aware CAD has been able to reduce on-chip temperatures by 10-14°C using only mathematical approximations of the heat generation in a component [7].

III. SET-UP AND PROCESS

A. Cyclone III Architecture

The experiments were conducted on a set of fourteen Arrow BeMicro FPGA Evaluation Kits with Cyclone III FPGAs model EP3C16F256C8N. The Cyclone III architecture uses a 65nm process technology and is optimized to minimize power

consumption. The chip is laid out as a 40 by 28 grid of LABs with two columns reserved as memory and another two as multipliers. Each LAB has 16 Logic Elements made up of up of a 4-input Look-up Table and a register. At each of the corners of the FPGA is a Phase-Locked Loop (PLL) which is used to drive the clocks in the experiment. Because of the granularity of the PLLs, the resolution of the clocks is limited to ± 1.6 ps. Figure 2 shows a diagram of a Cyclone III FPGA.

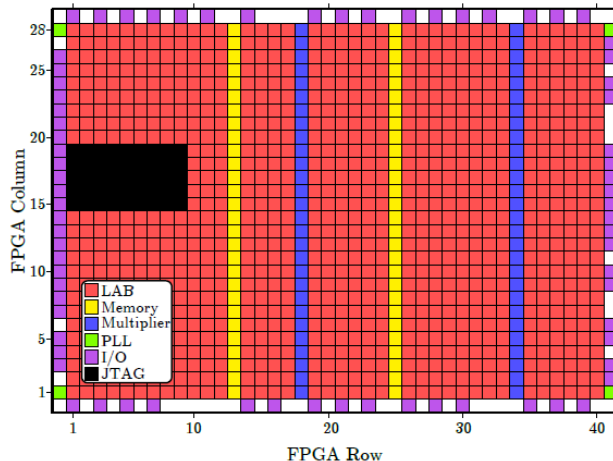


Figure 2. Resource diagram of the Cyclone III model EP3C16F256C8N FPGA.

The clock network of the Cyclone III is driven by a set of 20 global clocks. [8] These clocks drive the local clocks in the chip's four quadrants which in turn drive clocks that connect to the LABs along each row. Although the exact schematics of the clock network are not disseminated by Altera, experimental evidence implies that the four quadrants are four rectangles at the chip's corners with vertices at the chip's center. When the first component is added to a clock domain, a new local clock needs to be activated. When a new clock is activated, the activity in the local clock network increases because the local clock driver needs to expend additional energy on more clocks.

B. Experimental Process

The experiments conducted for this report were primarily studies into the relative locations of the CUTs. By changing the arrangement of the measurement circuits during Timing Extraction, we sought to influence the outcome in predictable ways. Thus, additional CUTs could act as both data collection devices and white noise generators. The complexity of the measurement circuit gave us several forms of noise, including clock loading, rapidly toggling wires and heat.

Paths were measured in three different ways: in isolation, in serial and in parallel. First, paths were isolated by forgoing placing other CUTs on the chip and measured to give a baseline for the path delay. As with Wong, Sedcole et al. and Gojman, the paths were measured in serial with other CUTs placed but only one active at a time. Paths were also measured in parallel so that multiple CUTs were active and generating noise all at once.

IV. EXPERIMENTAL RESULTS

A. Interaction between CUTs

Running experiments in parallel is desirable because of the increase in speed, but doing so will also generate additional activity on the chip. This activity will lead to self-heating which will in turn slow down the paths tested. The magnitude of this effect will determine whether parallel experiments produce worthwhile results. To test the viability of running experiments in parallel, a set of paths were chosen and tested over a set of experiments. In one trial 15 CUTs were placed on the FPGA per experiment, then 7 and 8 CUTs, 5 CUTs and 3 CUTs. These same configurations were run both in serial and in parallel, and the objective path delays are given in Figure 3.

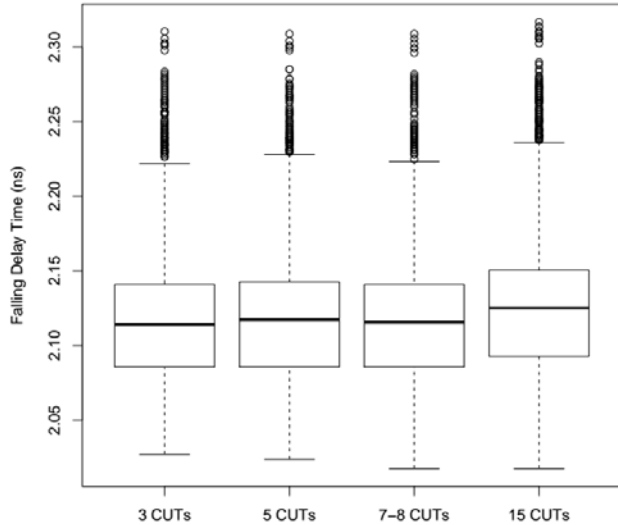


Figure 3. Box plot showing the delays recorded in experiments with different numbers of CUTs on the chip.

The mean rising delay for the 5 CUT and 7-8 CUT cases is ~ 1 ps higher than that of the 3 CUT case. But the 15 CUT data is on average 11ps higher than the 3 CUT data, meaning that parallel activation of this many CUTs causes a measurable slowdown in the tested paths.

Because the distance between the CUTs varied along with the number of CUTs placed, a set of paths were chosen from the top right corner of the FPGA by the only unused PLL and a noise generating CUT was placed near the path. The CUTs were run in parallel so that the second CUT would be generating noise. Distances between 2 and 12 LABs away were chosen and the noise generator was placed both on the same row and on the same column, while keeping both CUTs in the same clock quadrant. The path delays with the noise generator in each position were correlated and are given in Figure 4. Cases where the noise generator was on the row are shown in blue and cases where it was on the column are in red.

When the noise generator is placed on the column, its distance to the CUT has little effect. But when it is placed on the same row, the effects are Gaussian tending towards higher delays when the noise generator is placed 12 LABs away. Rather than demonstrating the assumed behavior where added heat causes delay increases proportional to $1/r^2$, the results depended on some other factor.

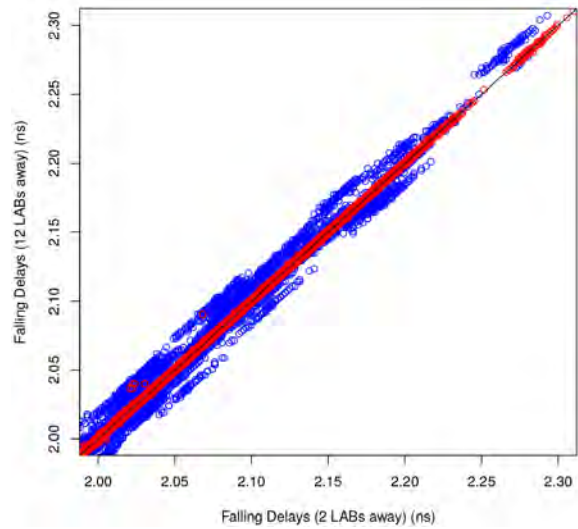


Figure 4. Relative timing delays when a noise generator is placed 12 LABs away versus 2 LABs away.

B. Clock Loading Effects

In order to reduce the effects that CUTs have on each other, the relative location between two CUTs was changed over a series experiments so that the delay of one could be found based on the position of another. The CUT to be tested was placed in the center of a clock quadrant at (30, 9) and the second was moved to positions within and surrounding the quadrant. These experiments were run both in serial and parallel. The falling delays of the CUT as a function of the second CUT's position are given in Figure 5 for the parallel experiment and in Figure 6 for the serial trial.

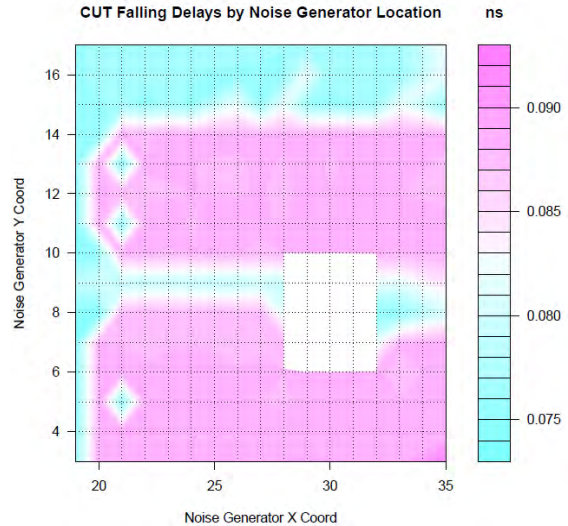


Figure 5. Falling delays over a CUT at (30,8) as a function of the position of a noise generator running in parallel, in ns. Note that there are no data points at $x=25$ or $x=34$ because of the memory and multiplier columns at those positions.

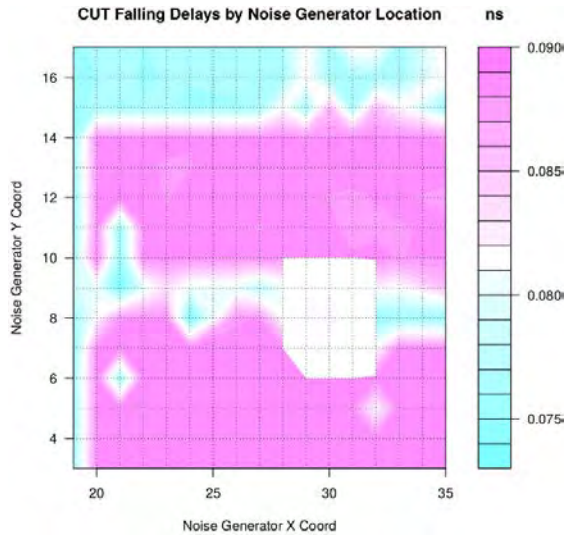


Figure 6. Falling delays over a CUT as a function of a noise generator running in series.

When the two CUTs are within the same quadrant, but occupying different rows, the path delays tended to be higher. When the CUTs are in different quadrants, the path delay drops. Note that although activating new clocks in different quadrants loads the global clock, it will not increase the activity on the clock local to the first CUT. However, when the two CUTs share a row or nearly share a row, the delays are almost as low as the out-of-quadrant case. If no new clock needs to be activated by this placement, the activity in the local clock remains roughly constant and little additional energy is introduced.

C. Viability of Parallelism

If the delays are lowest when the clock is not loaded by additional CUTs, can accurate results be taken in parallel so long as the CUTs are in different quadrants? Or does the addition of even a single CUT running in serial influence the measurement's accuracy?

Pairs of CUTs were placed on the FPGA so that in each experiment one CUT was placed on the lower half of the chip and the second was placed in a similar position in the same column in the quadrant above the first. In this way, a path from every LAB was measured both in serial and parallel. A baseline was created by measuring each path in complete isolation twice. The delta percent delays (DPD) were found for each path by finding the percentage that the isolated measurement increased or decreased when noise was introduced by the serial and parallel trials. These were compared with a control group consisting of the two identical isolated trials compared to each other. Figure 7 presents this data.

The DPDs are +0.04% on average and tend to stay between 0 and 0.08% in both trials, but may range up to $\pm 1.5\%$. For an average path, a 0.08% change is 1.6ps, which is the size of a single clock step. Placing a second CUT in a different quadrant has a modest impact on performance. Turning this CUT on to run the experiment in parallel has no further impact on the outcome of the measurement.

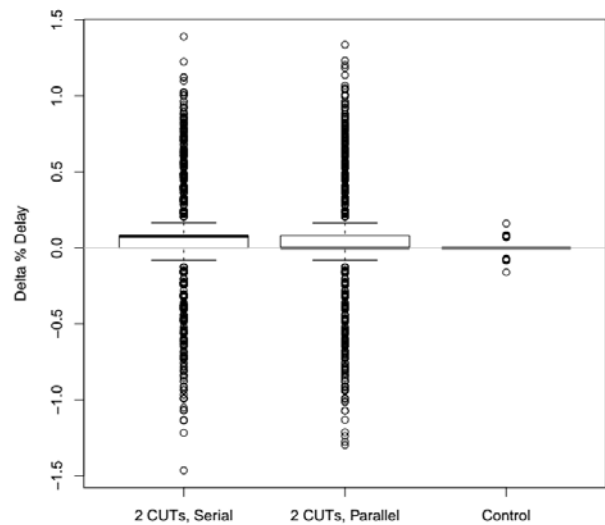


Figure 7. Delta Percent Delays comparing an isolated measurement to measurements in parallel and serial with a second CUT in a different quadrant.

To demonstrate the effects of testing multiple CUTs in the same quadrant, pairs of CUTs with equal relative distances were chosen, avoiding pairs that fell along the same row. Likewise, sets of twelve CUTs were chosen, with each set occupying a three-by-eleven block of LABs. These sets were run in serial and in parallel and the DPD was found with respect to the isolated case. Figure 8 compares these data.

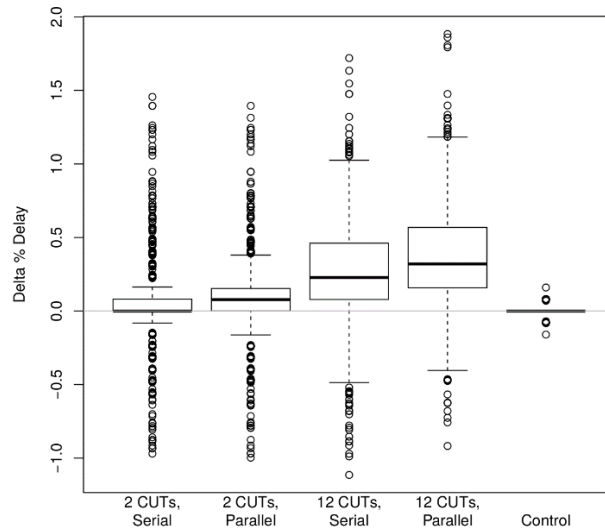


Figure 8. Delta Percent Delay for sets of two and twelve CUTs in the same quadrant both in serial and parallel.

Adding a second CUT even in serial usually has a modest effect, increasing the path delays by a small percentage. Turning this CUT on increases the delay by an average of 0.08%. Placing 12 CUTs rather than one increases the delays by 0.24% when they are run in serial and 0.38% when they are run in parallel, up to a maximum measured increase of 1.88%.

These experiments were continued by placing 4, 6, 12 and 24 CUTs into a single clock quadrant in one experiment. The mean delta percent delay was found when the CUTs were run in serial and parallel as compared to the isolated case. Figure 9 shows these delay increases as a function of the number of CUTs placed on the FPGA.

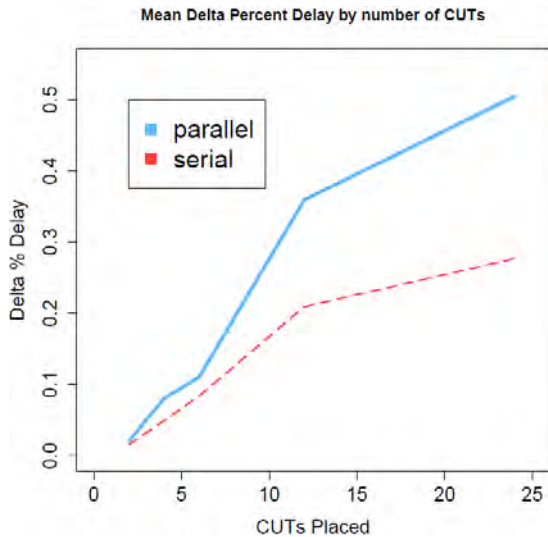


Figure 9. DPD of a CUT as a function of the number of other CUTs placed during the experiment. Serial trials are in orange and parallel trials are in blue.

As additional CUTs are placed into the experiment, the paths they measure will be slowed by each other's presence. However, when these CUTs are activated and the experiment is run in parallel, the effect they have increases by between 32% and 82%. While the effects of placing CUTs is lower when they are run in serial, the delays they induce can become substantial when too many of them are placed in a single quadrant.

V. DISCUSSION AND CONCLUSION

The measurement circuits used in Timing Extraction are prone to variation. Changing the configuration of the experiment by adding additional CUTs—even inactive CUTs in a different clock quadrant—changes the measured path delays by as much as 1.5% to 2%. Choosing the location of the CUTs by placing them in different quadrants or possibly in the same rows as each other can reduce, but not eliminate, this variation. Running the CUTs in parallel will always increase the noise on the measurements and often increase the path delays above the serial and isolated cases.

Whether these variations of 1.5% to 2% are a concern to the user depends on the application. In most practical applications, no path is run in maximum isolation, but will experience noise from nearby LABs. Further, running a complete timing analysis on the Cyclone III would require 2,736,556 distinct bitstreams to test each path individually and in complete isolation. [5] Such a process would be very time consuming, and may not be worth the increased accuracy of measurement.

VI. FURTHER QUESTIONS

This work focused only on the interaction between CUTs used in Timing Extraction and depended on them for noise generation. To increase the precision in choosing clock resources, more finely controlled circuits could be developed to selectively activate individual clocks. Thus the effects of turning on new row-specific clocks could be studied. Likewise, because the CUTs are tied to the clocks, other effects including self-heating and crosstalk from toggling

wires were not explored. These effects certainly can influence delays and could be characterized in further research.

The advantages to placing two CUTs in the same row have not been characterized. Doing so does mitigate clock loading, but less so than placing the CUT in a separate quadrant. Whether this can be used to increase parallelism is unclear.

ACKNOWLEDGMENT

The authors would like to acknowledge the support of the National Science Foundation, through NSF REU grant no. 1062672.

REFERENCES

- [1] J. S. J. Wong, P. Sedcole and P. Y. K. Cheung, "Self-Measurement of Combinatorial Circuit Delays in FPGAs," *ACM Transactions on Reconfigurable Technology and Systems (TRETs)*, vol. 2, no. 2, June 2009.
- [2] B. Gojman and A. DeHon, "GROK-INT: Generating Real On-Chip Knowledge for Interconnect Delays Using Timing Extraction," 2014 IEEE 22nd Annual International Symposium on Field-Programmable Custom Computing Machines (FCCM), pp. 88-95, 11-13 May 2014.
- [3] E. Stott, J. Wong, P. Sedcole and P. Cheung, "Degradation in FPGAs: measurement and modelling," *FPGA '10 Proceedings of the 18th annual ACM/SIGDA international symposium on Field programmable gate arrays*, pp. 229-238, February 2010.
- [4] K. Zick and J. Hayes, "Low-Cost Sensing with Ring Oscillator Arrays for Healthier Reconfigurable Systems," *ACM Transactions on Reconfigurable Technology and Systems*, vol. 5, no. 1, March 2012.
- [5] B. Gojman, "GROK-FPGA: Generating Real On-Chip Knowledge for FPGA Fine-Grain Delays using Timing Extraction," 2014.
- [6] J. J. L. Franco, E. Boemo, E. Castillo and L. Parrilla, "Ring oscillators as thermal sensors in FPGAs: Experiments in low voltage," *Programmable Logic Conference (SPL), 2010 VI Southern*, pp. 133,137, 24-26 March 2010.
- [7] S. Bhoj, "Thermal aware FPGA architectures and CAD," *International Conference on Field Programmable Logic and Applications*, pp. 701-702, 8-10 September 2008.
- [8] Altera Corporation, *Cyclone III Device Handbook*, 12 ed., vol. 1, San Jose, CA, 2012.

Photo-Actuation: Determining the Effect of Blue Light on the Actuation of Micro-Beads by *Serratia marcescens*

Erica Sadler (Cornell University – Biomedical Engineering), *SUNFEST Fellow*

Dr. Vijay Kumar – Departments of Mechanical Engineering and Applied Mechanics, Computer and Information Science, and Electrical and Systems Engineering

Abstract—MicroBioRobots (MBRs) are robotic systems with both an animate and inanimate component. The animate, or biological, component of MBRs acts as an actuator, providing the source of power for the MBR's movement. Since this biological component is, in fact, a living organism, it is generally very responsive to external stimuli. For this reason, microorganisms, such as bacteria, act as sensors in addition to actuators. In order to utilize the innate sensing of microorganisms effectively, their response to particular stimuli must be understood in a way that is both measurable and predictable.

Light is a stimulus known to affect the motility of bacteria. I developed a 2D tracking algorithm in MATLAB in order to analyze the motion of MBRs made up of micro-beads actuated by *Serratia marcescens*. I report on the effect of blue light on this motion, finding that a high intensity of blue light leads to an increase in the tumbling of bacteria and an overall decrease in the movement of MBRs, sometimes working strongly against a current.

Through my attempts to obtain accurate and useful data, I also examine the effectiveness of several techniques for creating functional MBRs and acquiring successful video data. This is a complex process of its own and does not yet have a generally agreed upon protocol. I take into account the pros and cons of several techniques, finding that the smaller bead size I observed (3 μm) was easier for the bacteria to move and control than the 6.8 μm beads. I also found that washing the micro-beads using sonication did appear to promote the natural attachment of the bacteria to the micro-beads. Due to the adhesion of both beads and bacteria to surrounding surfaces, it was best to use Percoll to give the MBRs buoyancy and then observe them on some plane other than the top or bottom to prevent any beads or bacteria that had become stuck in place from affecting the data. Drift

is another common problem when observing objects of this size, and the best way I found to control it was through the use of a sealed chamber.

Even with these improvements, future research is necessary to find the optimal way of collecting and analyzing data on MBRs. Future studies should also be conducted with MBRs using lower intensities of blue light to determine if different light intensities will affect the MBRs' motion differently. It would also be useful to conduct further research on how bacteria move beads of varying sizes so that the use of bacteria as an actuation technique is not limited solely to beads with diameters of 3 μm .

I. INTRODUCTION

Recent advancements have transformed robotic technology, once considered farfetched and futuristic, into an important aspect of many people's daily lives. From communication to medicine, robots are used in all manner of fields. As researchers continue to make enhancements, many robots are being created on a smaller and smaller scale. Microscopic devices have the potential of making an extremely large impact on society. However, objects of this size are not yet capable of their own, controlled motion without the presence of an external force, such as a magnetic field.

By utilizing the natural movement of flagellated bacteria such as *Escherichia coli* and *Serratia marcescens*, an external force is no longer necessary. The combined efforts of many individual bacteria cells can be used to power the movement of a larger device [1]. This process of providing the power behind motion is termed "actuation," and the source of the power, in this

case flagellated bacteria, is an “actuator.” In order for this technology to be implemented in any sort of useful way, researchers must be able to control the direction and speed with which the bacteria move these micro-robots. Possible methods for obtaining this control include the use of outside stimuli or the physical alteration of the micro-robots themselves. However, it is necessary to know the effects these methods will have on the bacteria and micro-robots, together making up an MBR, before they can be properly implemented.

II. BACKGROUND

A. Running and Tumbling of Flagellated Bacteria

The flagella of flagellated bacteria allow them to move and swim in fluid environments. The helical movement of each of the bacteria’s flagella is irreversible, and therefore allows the bacteria to move despite their low Reynolds number. These bacteria are constantly either “running” or “tumbling” depending on the direction in which their flagella are rotating. When all of the flagella are rotating counterclockwise, the bacterium is in a running state. In this state, the flagella bundle together and propel the bacterium forward in a single direction. If even one of the bacterium’s flagella begins to rotate clockwise, the bacterium will go into a tumbling state. When this occurs, the bacterium rotates in place, allowing it to change direction but resulting in little to no linear movement. By constantly switching back and forth between these two states, a bacterium develops what is sometimes referred to as a “random walk.” Without any significant environmental stimuli, a bacterium will generally spend more time in its running mode and tumble approximately once a second [2].

B. Effect of Blue Light

Blue light has been shown to produce a repellent response in *E. coli* cells [3]. Due to their similar structure, it is possible that this same response may also be observed in *S. marcescens*. However, it is not clear that the application of blue light always acts as a repellent to the bacteria. Since the response in *E. coli* cells is caused by several photoreceptors, factors such as the intensity of the light are believed to have slightly different effects on each of the receptors and could therefore change the cells’ behavior. It is also important to recognize

that blue light could act as a short-term repellent while having a different effect in the long-term or vice versa, as bacteria commonly adapt to their environment [3].

C. pH-Taxis with Bacteria-Driven Micro-Beads

Micro-beads actuated by *S. marcescens* have been previously researched in a microfluidic channel with a stable pH gradient. The cells formed attachments with the micro-beads and moved them to an area with a more desirable pH for the bacteria [4]. Thus, it is reasonable to conclude that the ability of *S. marcescens* to stick to, push, and pull micro-beads is not affected by the desirability of pH. Instead, the creation of a pH gradient primarily affects the direction of the bacteria’s motion.

D. Phototaxis with Bacteria-Driven Micro-Beads

The effect of UV light on microstructures actuated by swarming *S. marcescens* has also been observed. Phototaxis may be preferable to chemotaxis because light can quickly and easily be added or removed from an area and is visually detectable. Light also tends to create less of a gradient than its chemical stimuli counterparts, allowing for a more uniform response from the cells. Initial experimentation suggested UV light could be used to halt the motion of microbiorobots [5]. Later research attempted to use UV light to prevent rotational motion while electric fields were used to produce linear motion. In this case, UV light stopped rotational motion completely for only one to two seconds, but the long-term effect was a reduced rotational velocity with each exposure to the light [1].

E. Motility Buffers and Other Techniques for Successful Video Data

Certain chemicals and techniques are commonly used when observing the motion of MBRs, but the key to their successful implementation is balance. While it is necessary that the bacteria and micro-beads attach to one another, any additional attachment they have to surfaces or themselves could impact the data, resulting in inaccurate conclusions with respect to the motion of MBRs. Tween, Bovine Serum Albumin (BSA), Polydimethylsiloxane (PDMS) coating, Percoll, and chambers have all been previously used to prevent unwanted attachments, settling, or drift in a microscopic environment. However, because we are working on a scale where our vision is very limited, it is often difficult to predict the full effect these

techniques will have on the MBRs' motion. It is thus important for different "solutions" to be tested and their effect observed before determining if they should be used in final experimentation.

III. MATERIALS AND METHODS

A. Bacteria

The flagellated bacteria *S. marcescens* were used for all experiments. Cells were prepared by inoculating a 10ml solution of Luria-Burtani (LB) broth with 10 μ l of *S. marcescens*. This solution was then incubated for four hours at 34 degrees Celsius. During this incubation period, the solution was moved repeatedly in a circular motion at 180rpm. The *S. marcescens* were used for experiments immediately after their incubation period was complete.

B. Micro-Beads

We used red fluorescent beads with a radius of 3 μ m. We sonicated and centrifuged the beads five times, alternating between water and IPA, before re-suspending them in motility buffer. This sonication process has been done in previous studies [4], and its purpose was to remove any surfactant on the outside of the micro-beads in order to promote natural attachment between the beads and bacteria.

C. MicroBioRobots

The bacteria and bead solutions were combined on the slide and pipetted back and forth several times to promote attachments between the *S. marcescens* and micro-beads. While BSA and Tween were both tested as methods to prevent the sticking of bacteria and beads to surrounding surfaces, it was eventually decided that using Percoll to suspend bacteria and beads before observing them in a central plane was the best option. Unlike BSA and Tween, Percoll did not appear to have an effect on the attachments of the bacteria and beads to one another.

D. Microscopy and Imaging

I took videos using a RETIGA EXi FAST Cooled Mono 12-bit camera by QImaging. I connected the camera to an Axioplan 2 imaging microscope to observe the MBRs using both a 40x water immersion lens and a 10x oil immersion lens. Neither of these lenses was immersed in the fluid sample because the chamber used included a coverslip separating the

sample and the lens. Despite this, the lenses still focused properly and were able to provide good images. The videos were taken and put into Audio Video Interleaved (AVI) format with the program Image-Pro Plus 7.0.

E. Tracking

I wrote a MATLAB tracking code to follow and record the paths of objects from frame to frame. The code uses MATLAB's built in function object finder and compares the objects found in each frame as well as their distances from one another to determine how the objects move over time. I then expanded upon this using the Hough transform to track only circular objects. This allowed me to track only micro-beads in videos where both bacteria and micro-beads were present and visible. Using the paths found through this tracking code, I was able to obtain quantitative data from the videos including the mean squared displacements of moving bacteria and/or beads, the direction of their motion, their speeds with relation to each other, and other relevant pieces of information.

IV. EXPERIMENTAL RESULTS

When determining the change in movement of tracked objects, the mean squared displacement (MSD) proved to be a useful statistic. In early experimentation, when only *S. marcescens* were being observed, the average MSD for all bacteria tracked was approximately the same whether or not the blue light was turned on. However, when methods to prevent bacteria from sticking to the slide were implemented, the MSD proved to be significantly smaller when the blue light was turned on. This suggests that the application of blue light increases the rate at which *S. marcescens* tumble. This result was not seen when bacteria were sticking to the slide because such a large portion of *S. marcescens* remained in place regardless of light, leading the average MSD to be so similar that the underlying trend could not be seen. The best solution found for this problem of sticking was to use Percoll to give beads and bacteria additional buoyancy and then observe them on some horizontal plane toward the middle of the sample. When these MBRs were observed, it was clear that they moved significantly less when exposed to blue light. This reaction remained true for all intensities of blue light tested, though stronger intensities did have a stronger impact. It appeared that in this case, where light is shown

on a particular area without creating a gradient to build up to the point of focus, blue light has little impact on the direction of movement but a large impact on the speed and amount of movement.

V. DISCUSSION AND CONCLUSION

After exposing MBRs to blue light, we can conclude that at high intensities, blue light causes an increase in the frequency with which *S. marcescens* tumble and a nearly complete halt in the movement of the MBRs throughout the duration of the blue light exposure. While it did not appear that MBRs outside the scope of the light source were any more likely to move toward the lit area than they had been previously, MBRs that were directly illuminated by the blue light looked almost as if they were becoming “stuck” in place. It seems unlikely that the blue light created this effect solely by increasing the frequency of tumbling in *S. marcescens*. If this were the case, it would be expected that the MBRs would decrease in their movement but still continue to move along with any drift present. Further research is necessary to know how the blue light may have altered the MBRs or the surrounding environment in such a way that would cause the MBRs to halt almost entirely. Once it is better understood why blue light has this effect on MBRs and if it can be reproduced in other environments, blue light may become a useful tool in controlling the motion of MBRs collectively without an outside source of power. Future studies should also look into lower intensities of blue light to determine if they have similar effects.

VI. ACKNOWLEDGMENT

I would like to thank Dr. Vijay Kumar of the University of Pennsylvania for allowing me the opportunity to work in his lab and for his mentorship throughout this summer. I would like to give a special thanks to Denise Wong and Dr. Edward Steager for their continuous help and guidance every step of the way. I would also like to thank everyone involved in the SUNFEST program including Dr. Van der Spiegel, Colleen Kennedy, Joshua Taton, and Jessica Leon for their investment in every aspect of the Summer Undergraduate Fellowships in Sensor Technologies program. Lastly, I would like to thank the NSF for their funding and support of this program.

REFERENCES

- [1] Steager EB, Sakar MS, Kim DH, Kumar V, Pappas GJ, Kim MJ. 2011. Electrokinetic and optical control of bacterial microrobots. *Journal of Micromechanics and Microengineering* (21). [accessed 2011 Jan 2] doi:10.1088/0960-1317/21/3/035001
- [2] Alberts B, Johnson A, Lewis J, Raff M, Roberts K, Walter P. 2008. *Molecular Biology of the Cell*. 5th ed. New York (NY): Garland Science. p. 941-943.
- [3] Wright S, Walia B, Parkinson JS, Shahid K. 2006. Differential Activation of *Escherichia coli* Chemoreceptors by Blue-Light Stimuli. *American Society for Microbiology* (188). doi:10.1128/JB.00149-06
- [4] Zhuang J, Carlsen RW, Sitti M. 2015. pH-Taxis of Biohybrid Microsystems. *Scientific Reports*. doi:10.1038/srep11403
- [5] Steager E, Chang-Beom K, Jigarkumar P, Socheth B, Chandan N, Reber L, Kim MJ. 2007. Control of microfabricated structures powered by flagellated bacteria using phototaxis. *Applied Physics Letters* (90). doi:10.1063/1.2752721

Geometric Stereo Increases Accuracy of Depth Estimations for an Unmanned Air Vehicle with a Small Baseline Stereo System

Eleanor Tursman (Grinnell College, Physics), *SUNFEST Fellow*

Camillo Jose Taylor, CIS

Abstract— A small stereo camera is a light and economical solution for obstacle detection and avoidance for unmanned air vehicles (UAVs). It is possible to create depth maps of a scene given a pair of stereo frames from such a camera. However, the smaller and lighter the stereo camera, the smaller its baseline, which in turn limits its ability to discriminate objects that are farther away. Maximizing the effective range of the stereo setup is essential for real-time applications, where quick decisions need to be made to avoid obstacles approaching the UAV. To overcome this difficulty, we use knowledge of the camera’s position over time to mimic large baseline disparity calculations, a technique we have dubbed “geometric stereo.” This paper outlines a simulation that shows that this technique is able to obtain better results for depth estimation with smaller confidence intervals than those obtained by simply averaging discrete depth maps over time.

Index Terms— Geometric stereo, Obstacle detection, Robotics, Simulation, Small baseline stereo, Stereo vision UAV

I. INTRODUCTION

Unmanned air vehicles (UAVs) are used in both military and civilian contexts, aiding in tasks from search and rescue missions to structural inspections of power lines and bridges [1][2]. In order to effectively accomplish these tasks, UAVs must be able to adapt their flight paths in 3D space in order to avoid detected obstacles in both static and dynamic environments. To meet real-time application goals, it is necessary for the UAV to meet size, weight, and power (SWAP) constraints. Both laser sensors (LiDAR) and cameras have been used by UAVs capable of working in real-time. However, while obstacle detection using LiDAR has proved successful for both ground and air based vehicles [4], LiDAR cannot meet SWAP constraints. One example

of a small commercially available LiDAR which could be mounted on a UAV is the Hokuyo UTM-30LX. It weighs 370 grams, consumes 12V at 0.7amps, and is 60x60x87mm. Though the laser is precise, using LiDAR for real-time applications on a small UAV cannot be ideal due to these limitations. On the other hand, stereo cameras are smaller, lighter, and consume much less power, making them more attractive for this task.

Computer vision is a field that focuses on enabling machines to mimic the high-level perceptive power of humans. A stereo camera, paired with computer vision algorithms, can therefore provide a sensor that better meets SWAP constraints while accomplishing real-time tasks. Through the combination of stereo and visual odometry, two vision techniques, we hope to maximize how quickly a UAV can move while accurately avoiding obstacles. Since we wish to minimize SWAP constraints, our stereo camera must be as small as possible. This caveat means that the baseline, or the distance between the two lenses, limits the distance the camera can “see.” There is an inherent trade-off between the baseline and accuracy of a stereo camera. To make depth measurements of a scene, a stereo algorithm must correctly match points between the left and right views from each lens. While a larger baseline stereo camera can detect objects farther away, it also makes it more difficult to match points correctly, which lowers the accuracy of depth results. We therefore use a stereo camera with a small baseline, for its greater accuracy, lighter weight, smaller size, and smaller power consumption.

We show through simulation that it is possible to compensate for the short range of a small baseline stereo camera by integrating knowledge of camera pose with our images to mimic the results of a larger-baseline stereo system. By then integrating this system onto an onboard graphics processing unit (GPU) for parallel processing of stereo feature matching, we can produce a UAV that better meets SWAP constraints, and is also able to more effectively build an accurate 3D representation of the



Figure 1– From left to right: a small quadcopter UAV (DJI F450), the Jetson TK1, and the DUO-MLX. The DUO-MLX has a small 30mm baseline, and a 2.0mm focal length.

world around it. This UAV can then be purposed towards accomplishing tasks such as search and rescue with improved speed and accuracy.

To accomplish this goal, we choose to use the DUO-MLX stereo camera, pictured in Figure 1. The simulation's parameters are based upon the specifications of this small stereo camera. This specific camera was chosen for being light at 12.5g, small at 52.02x25.40x13.30mm, for featuring a wide field of view (FOV) at 170 degrees, for only consuming 5V at 0.5amps, and for having a built-in inertial measurement unit (IMU). We will integrate the DUO-MLX with the small Jetson TK1 board, which has GPU processing capabilities, for speed.

II. BACKGROUND

2.1 Stereo Vision

Stereo vision is a tool used to gather depth information from a pair of left and right images, mimicking the binocular system of human vision. Once the camera is calibrated, the left and right images are rectified, a process that simplifies the geometry of the scene, and places matching features across the left and right images along the same horizontal lines. It is then possible to determine the physical depth of pixels in an image by calculating each pixel's disparity, the difference between the location of the pixel in the left image and the right image. To obtain disparity measurements, it is necessary to correctly match pixels between the left and right images. This hard problem has typically been solved using feature or featureless methods. For example, some researchers have employed the Small Vision System (SVS) stereo engine, which uses feature matching to generate depth maps [3]. Others have forgone features and instead use dense or semi-dense methods that make use of most or all of the pixels in each image [6][7][8]. In [8], researchers suggest comparing temporal and spatial gradients to quickly discern disparity measurements. These featureless methods typically rely upon exploiting camera motion to estimate where pixels have moved across image frames.

A sufficiently accurate depth map allows the UAV to determine which points are closest to the stereo camera in the scene, and therefore what obstacles must immediately be avoided. Stereo cameras have been used for obstacle detection in [1][2][3][4]. In section three, we will explore some of the basic mathematical details of stereo.

2.2 Visual Odometry

Visual odometry is the process of estimating the orientation and location of a camera based on the camera's video feed. With this tool, it is possible to determine the relative 3D locations of both points in images and the location of the camera, and therefore help an autonomous robot navigate through an unknown environment. Visual odometry typically locates and tracks features across image frames, and then uses their motion to calculate the essential or fundamental matrices, which through standard value decomposition (SVD) will produce the rotation matrix and translation vector that describe how the camera has shifted from one frame to the next. The essential matrix uses calibrated camera information to determine the rotation and translation information between frames. The fundamental matrix, which can be used with uncalibrated cameras, uses projective geometry to determine a line along which one point in the first image may be found in the second image [9]. However, more recent literature details a method for visual odometry that bypasses feature extraction entirely [6][7].

2.3 UAV Obstacle Detection

Several different methods have already been applied to UAV obstacle detection and avoidance, which use both monocular (single camera) and stereo (dual camera) systems. In [1], objects close to the stereo camera are isolated by segmenting depth maps. Another group combines frontal stereo vision with two side-facing fisheye cameras using optical flow to avoid both objects in front of and walls to the sides of the UAV [3].

Simpler monocular systems detect and track features in image frames from video feed, relying on

optical flow to situate a sparse number of these features in 3D space. The features are then clustered based on their relative distance from one another, determining the areas for the UAV to avoid [5]. However, the current state-of-the-art in robotic obstacle avoidance arguably lies with SLAM (simultaneous localization and mapping), where a robot builds and navigates within a map of its unknown surroundings using monocular vision [6][7]. In [6], LSD-SLAM (large-scale direct monocular SLAM) sidesteps feature extraction, which can be a time-consuming process, and instead uses every pixel in every frame, performing optimization on actual images. The goal of this system is to construct a large-scale depth map over time by tracking the camera's position and estimating its current pose through a series of frames, then using these frames to imitate a stereo system and calculate depth maps. These depth maps are refined, and then integrated into the large-scale depth map, which is finally optimized. The camera's pose in 3D space is estimated by referencing the dense depth map. The system is capable of running in real-time, however, since it is ultimately based on monocular input, it will only be able to build a 3D model up to a scale factor. By using a stereo camera, we can mitigate this limitation, leading to accurately scaled representations of the 3D world.

Unlike the previous literature, we will implement geometric stereo in order to improve upon monocular SLAM. We will be integrating scaled stereo depth maps from a small baseline camera with visual odometry information in order to mimic large

baseline stereo results while achieving real-time performance.

III. GEOMETRIC STEREO ALGORITHM

3.1 The Problem

We need to be able to compensate for the limited range of a small baseline camera, because its small size, weight, and power consumption is integral for optimizing our UAV. The equation to model a stereo setup can be determined by exploiting properties of similar triangles (see Fig. 2):

$$Z = \frac{Bf}{d} \quad (1)$$

where Z is the depth of the point in space, B is the baseline of the stereo system, d is the disparity, and f is the focal length of the cameras. We then add a

pixel error δ to this disparity calculation, resulting in

$$Z = \frac{f}{\frac{d}{B} \pm \delta} \quad (2)$$

Based on (1) and (2), there is an inherent trade-off between accuracy and baseline. As the baseline increases, the depth at which we are able to discriminate objects with a disparity of one pixel increases. Also, as the baseline increases, the error

term δ decreases relative to the constantly scaling signal term. However, there are limitations imposed by large-baseline stereo. The number of points shared by the left and right views decreases as the baseline increases, limiting the field of view of the system. In addition, the larger the baseline, the larger the range of disparities that must be searched through per pixel, which can drastically slow down the generation of depth maps.

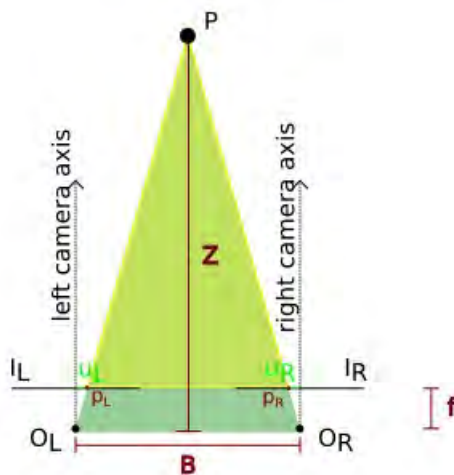


Figure 2– Similar triangle stereo setup. By using the properties of similar triangles, comparing the yellow and green triangles, we are able to derive the standard stereo equation. I_L and I_R are the left and right image planes, O_L and O_R are the left and right optical centers, B is the baseline, f is the focal length, P is the point in 3D space, Z is the depth, and u_L and u_R mark the pixel difference between where the ray to point P intersects each image plane and the camera axis. To set up the equation, simply let $d = u_R - u_L$.

$$Z = \frac{f}{\frac{d}{B} \pm \delta}$$

$$L \quad R$$

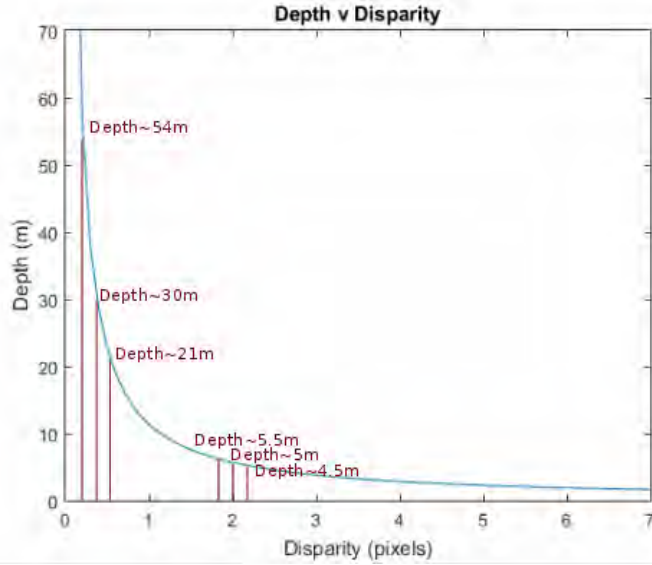


Figure 3– Depth v. disparity prediction for the DUO-MLX. The groups of three red lines represent a true depth measurement, and its possible disparity error to the left and right. Because of the small baseline, a sub-pixel disparity error could mean the difference between thinking a point is 30m away or 54m away.

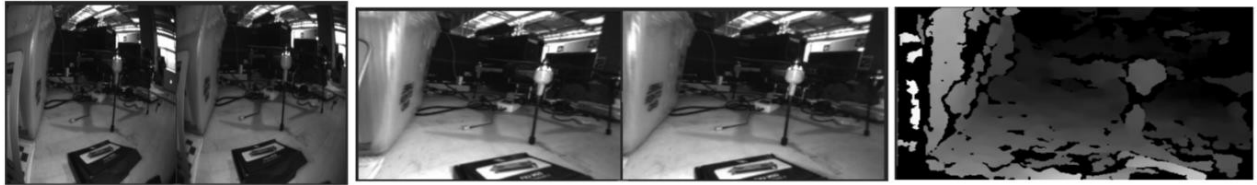


Figure 4– From left to right, the raw images of the DUO-MLX, the rectified images, and the disparity map. The images were captured with the SDK and dashboard provided with the DUO-MLX. The disparity map illustrates the good capabilities of the camera at ranges under one meter.

With the DUO-MLX, our small baseline stereo camera, measurements of points beyond approximately ten meters become very unreliable, since their accuracy heavily relies upon exact disparity calculations, which simply isn't realistic (see Fig. 3). In practice the stereo imagery we are able to obtain is displayed in Figure 4.

3.2 The Simulation

We propose circumventing these small baseline limitations by using our knowledge of camera translation over time in order to imitate large baseline stereo results using our small baseline images. The simulation we use to demonstrate this plan implements a simple stereo scenario, adds noise and bias to measurements to better imitate real-world data, then compares the accuracy of depth calculations and the size of confidence intervals, for both averaging and geometric stereo methods.

For the purposes of this paper, the term “averaging stereo” refers to taking the average of two

small-baseline depth maps to crudely obtain a more accurate depth estimation of a given scene. Averaging stereo does not integrate camera position data into its depth estimations. In turn, the term “geometric stereo” refers to using knowledge of camera position to mimic large-baseline stereo with a small-baseline system by taking one image from one position and one image from the second position to calculate a more accurate depth map (see Fig. 5). We will show that geometric stereo provides superior depth estimation results.

3.3 Depth Error

We create a simple scenario where two stereo cameras are separated by a purely horizontal translation and both focus on one point in 2D x-z space. The points u_L and u_R where the point will be projected on the left and right image planes of each stereo system will be determined using

$$u_L = f \frac{x_p - x_c}{z}, u_R = f \frac{x_p - x_c - B}{z} \quad (3)$$

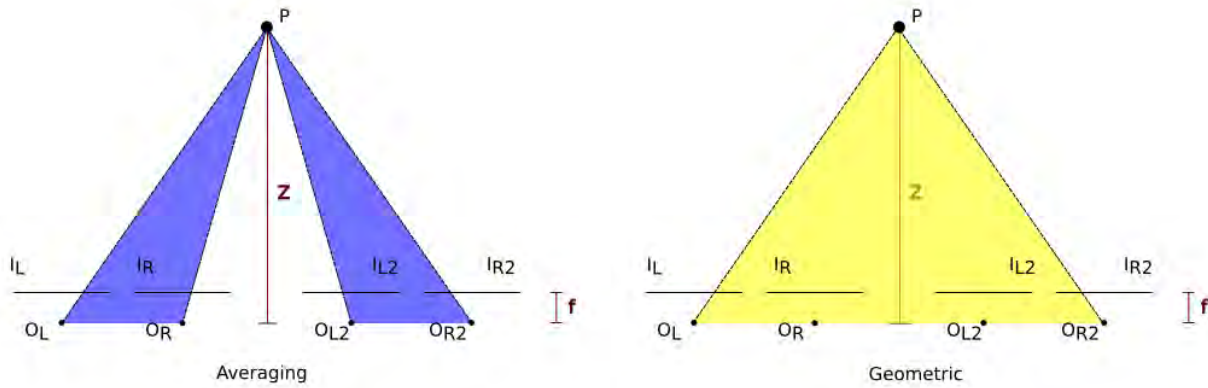


Figure 5– Averaging stereo takes two depth measurements from a stereo camera in two separate positions, while geometric stereo uses the outer image planes to mimic one large baseline stereo setup.

where (x_p, Z) is the location of the point in space, $(x_{\diamond}, 0)$ is the location of the optical center of the left camera, $(x_{\diamond} + B, 0)$ is the location of the optical center of the right camera, and f is the focal length of the cameras (see Fig. 6). We then add a noise term and a bias term to both u_L and u_R , to get

$$\tilde{u} = u_L + \diamond + \diamond, \tilde{u}_R = u_R + \diamond + \diamond \quad (4)$$

We add a random amount of noise \diamond between negative one and one pixel to each projection onto the image plane to better simulate pixel matching in a stereo matching algorithm. We also add a random bias \diamond between zero and one pixel to each calculation

in order to avoid the unrealistic zero-means scenario, where we would theoretically be able to remove noise from our calculations by taking a large number of images of the same scene.

To simulate the averaging technique, we calculate depth value error by taking the depths calculated by (1) for the left and right lenses, subtracting the true depth from each calculated depth to get the error of each calculation, then averaging these error results together. To simulate the geometric technique, we use the far left and far right image planes to get our first depth estimate, then we subtract the true depth from our estimate to get our error. Because of the noise and bias, each resulting depth error will change for every iteration of the simulation, so we run the algorithm 1000 times, and then produce histograms of our results.

3.4 Confidence Intervals

Stereo depth confidence intervals stipulate a range of values that should contain the true depth for

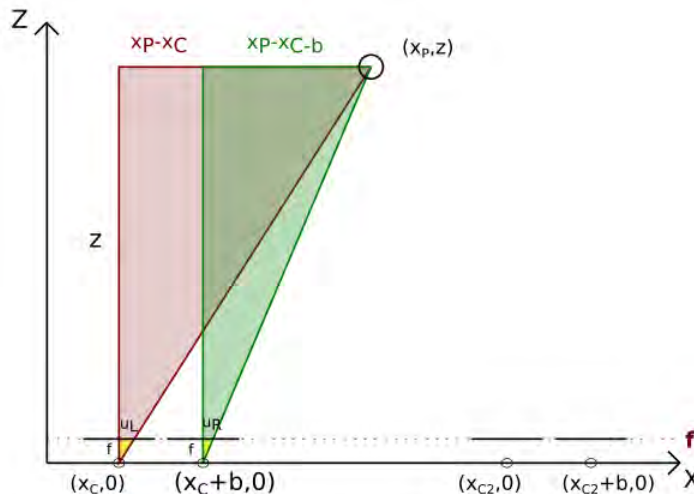


Figure 6– Simulation setup. We obtain (3) by once again comparing similar triangles. The red and yellow triangles can be used to solve for u_L , and the green and yellow triangles can be used to solve for u_R .

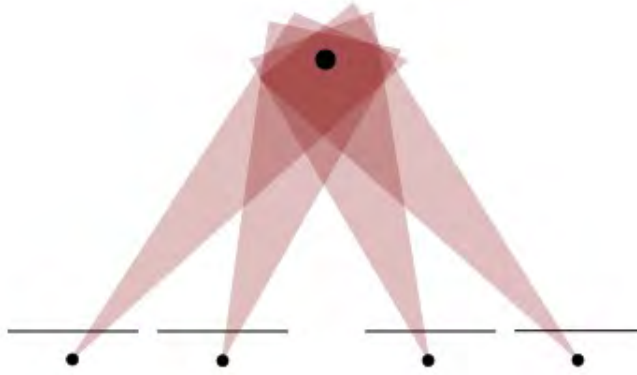


Figure 7– Confidence intervals with our setup. Given each cone coming from each optical center describes the confidence interval for that lens’ depth calculation, the dark area where all of the cones intersect is the overall confidence interval.

a given point in space. The smaller the interval, the more certain we can be about the accuracy of the calculated depth. To determine confidence intervals in the simulation, we obtain intervals for each depth calculation, then overlap them to get the overall confidence interval. Each B_j interval is determined by the δ term from (2), or $[-\delta, \delta]$. Because

depth would put the point behind the camera, if part of the calculated interval is negative, it is set to zero. We take the intersection of the intervals for the averaging technique, and the solitary interval for the geometric technique. We then compare the average size of these intervals over 1000 trials.

IV. EXPERIMENTAL RESULTS

4.1 Depth Error Results

As pictured in Figure 8, we see that while for a small true depth of one meter, the averaging and geometric techniques return error on the same scale, as the true depth increases to five and ten meters, the geometric results maintain error of around a meter or less, and the averaging results quickly become

sporadic and widespread. The geometric results maintain high counts around the zero error area, but the averaging results quickly drop to low counts that in the depth ten scenario ranged from -1884.0 meters to 586.2657 meters. As we predicted, the geometric results provide better depth estimates than the averaging results as the point in space moves away from the camera.

4.2 Confidence Interval Results

Our confidence interval results mirror our depth error results. In Table I, it is apparent that the average size of our confidence intervals increases much more rapidly for depths calculated using the averaging technique than for depths calculated using the geometric technique. The standard deviations of the intervals from the averaging technique also increase rapidly as true depth increases, making the depth calculations increasingly unreliable, especially at a true depth of ten meters. Our results indicate that our geometric results are much more accurate than our averaging results.

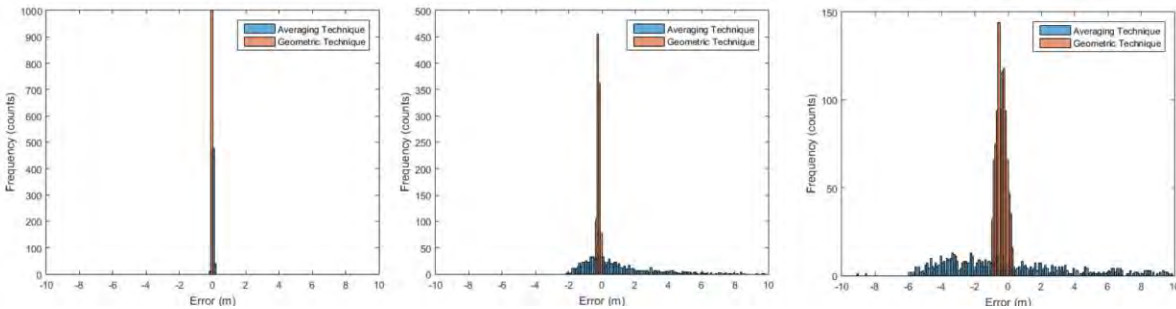


Figure 8– Error of averaging and geometric techniques for varying depths, where error is depth minus the true depth. Plots are set to a [-10,10] range for clearer visual comparison. For $Z = 1\text{m}$, the averaging technique has a range of [-0.1410m,0.1487m] and the geometric technique has a range of [-0.0477m,-0.0345m]. For $Z = 5\text{m}$, the averaging technique has a range of [-2.1288m,18.4689m] and the geometric technique has a range of [-0.3676m,-0.0307m]. For $Z = 10\text{m}$, the averaging technique has a range of [-1884.0m,586.2657m] and the geometric technique has a range of [-1.0136m,0.3156]. The pixel error is ± 1 pixel, the focal length is 380 pixels, the baseline is 0.03m, and the bias is between zero and one pixels. Notice that the spread of error values greatly increases for the averaging technique as the true depth of the point increases, while the spread of error values remains comparatively small for the geometric technique.

Depth (m)	Mean Averaging Interval Size (m) \pm one standard deviation	Mean Geometric Interval Size (m) \pm one standard deviation
1	0.0961 \pm 0.0617	0.0069 \pm 4.0129e-5
2	0.4003 \pm 0.2793	0.0277 \pm 3.2261e-4
3	1.0031 \pm 0.7848	0.0623 \pm 0.0011
4	2.0353 \pm 2.1785	0.1107 \pm 0.0026
5	3.4811 \pm 4.8566	0.1731 \pm 0.0049
10	8.5002 \pm 23.0214	0.6944 \pm 0.0412

Table 1– Average confidence interval size for varying depths. If the minimum of the interval predicted negative depth, it was replaced with a zero. Notice that the averaging technique intervals not only drastically increase as the true depth increases, but their standard deviations also drastically increase. The geometric technique intervals remain under a meter, with small standard deviations for every true depth value in this table.

V. DISCUSSION AND CONCLUSION

We are able to show through simulation that using knowledge of camera motion through time to mimic large baseline stereo using a small baseline camera provides more accurate depth calculations than averaging small baseline depth calculations over time. Not only does geometric stereo provide depth calculations for large true depth results with consistently small error, but its calculations also have steadily small confidence intervals. The results of this simulation motivate tracking camera motion over time to generate more accurate stereo depth data, with the ultimate goal of building a system that will give a confidence interval for each depth measurement, so it is easy to throw out or minimize the value of unreliable points. By implementing geometric stereo on the DUO-MLX camera, we will be able to mirror results from a camera with a larger baseline without its extra weight and power consumption, therefore meeting our SWAP constraints without sacrificing the accuracy and range of a larger system.

ACKNOWLEDGEMENT

The author would like to acknowledge the support of the National Science Foundation, through NSF REU grant no. 1062672, and the support of Professor Taylor and Professor Van der Spiegel throughout the summer.

REFERENCES

- [1] J. Byrne, M. Cosgrove, and R. Mehra, "Stereo Based Obstacle Detection for an Unmanned Air Vehicle," in *Proceedings of the 2006 IEEE International Conference on Robotics and Automation*, May 2006.
- [2] S. Hrabar, "3D Path Planning and Stereo-based Obstacle Avoidance for Rotorcraft UAVs," in *2008 IEEE/RSJ International Conference on Intelligent Robots and Systems*, September 2008.
- [3] S. Hrabar, G. Sukhatme, P. Corke, K. Usher, and J. Roberts, "Combined Optic-Flow and Stereo-Based Navigation of Urban Canyons for a UAV," in *2005 IEEE/RSJ International Conference on Intelligent Robots and Systems*, August 2005.
- [4] S. Hrabar, "An Evaluation of Stereo and Laser-Based Range Sensing for Rotorcraft Unmanned Aerial Vehicle Obstacle Avoidance," *Journal of Field Robotics* 29 (2012): 215–239, doi: 10.1002/rob.21404.
- [5] B. Call, R. Beard, C. Taylor, and B. Barber, "Obstacle Avoidance For Unmanned Air Vehicles Using Image Feature Tracking," in *AIAA Guidance, Navigation, and Control Conference and Exhibit*, August 2006.
- [6] J. Engel, T. Schops, and D. Cremers, "LSD-SLAM: Large-Scale Direct Monocular SLAM," in *European Conference on Computer Vision (ECCV)*, 2014.
- [7] R. A. Newcombe, S. J. Lovegrove, and A. J. Davison, "DTAM: Dense Tracking and Mapping in Real-Time," in *International Conference on Computer Vision (ICCV)*, November 2011.
- [8] K. Skifstad and R. Jain, "Range Estimation from Intensity Gradient Analysis," *Machine Vision and Applications* 2 (1989): 81-102, doi: 10.1007/BF01212370.
- [9] R. Szeliski, *Computer Vision: Algorithms and Applications* (Springer, 2010), <http://szeliski.org/Book/>, 348-354.

Preparation of Electrospun Piezoelectric Polyvinylidene Fluoride Nanofibers

Jerrell Walker, Electrical Engineering student at the University of Pennsylvania, *SUNFEST Fellow*

Dr. Jorge J. Santiago - Aviles, Electrical Engineering

A. Abstract—This work focuses on electrospinning nanofibers for use as an alternative solution to cochlear implants to address a loss of hearing. The required diameter for self-poled piezoelectric nanofibers is 100 nm. Experiments used solutions of Polyvinylidene Fluoride (PVDF) dissolved in combinations of dimethylformamide, acetone, and a light-emitting polymer F8BT. Average fiber diameters were larger than desired. Two notable solutions yielded average diameters of 180 nm to 200 nm. High resolution scanning electron microscopy was used to characterize the fiber's diameter. Further work will have to be done to modify the electrospinning parameters to obtain the proper diameter for this application.

Index Terms— Electrospinning, Nanofiber, PVDF, Self-poled

INTRODUCTION

Hearing loss is a significant problem that is most commonly caused by chronic and sustained exposure to high sound levels, birth defects, and/or disease. At present, hearing aids and cochlear implants are two well-developed solutions for hearing loss. Hearing aids are a valuable solution that augments the normal sense of hearing for their user. Hearing aids are based on the principle of amplification. A microphone is used to record sounds as electrical signals, which are then processed within the hearing aid. After the processing, a speaker converts the electrical signals into amplified sound waves that are directed into the user's ear. This solution is applicable when patients have mild to moderate hearing loss. This method does require that the structures of the inner ear and cochlea can still perform their normal functions despite being impaired. This impairment commonly manifests as damaged or dead hair cells within the cochlea. There must be a considerable number of surviving hair cells spread along the cochlea to allow hearing aids to compensate for some lacking hair cells. Those with severe or total hearing loss may pursue cochlear implants to provide a semblance of our natural hearing sense. These implants require electrodes to be surgically implanted within the patient's ear to provide direct stimulation to the auditory nerves. These electrodes effectively replace the cochlea and the hair cells that are used to transduce sound and convey the information to the brain. Instead the electrodes directly stimulate auditory neurons and provide a different sense of hearing. Cochlear implants also need to have

a microphone for receiving sounds and a larger speech processing unit that will control the stimuli provided by the electrodes. The main complaint against cochlear implants that we wish to address is the invasive nature of the implanting process. The nanofiber based solution that my research group is working on aims to provide a minimally invasive alternative to the cochlear implant. The fibers produced will be used as replacements for the inner hair cells of the cochlea. This means our solution will be applicable when the hair cells are dead or missing but will require the rest of the inner ear to be functional.

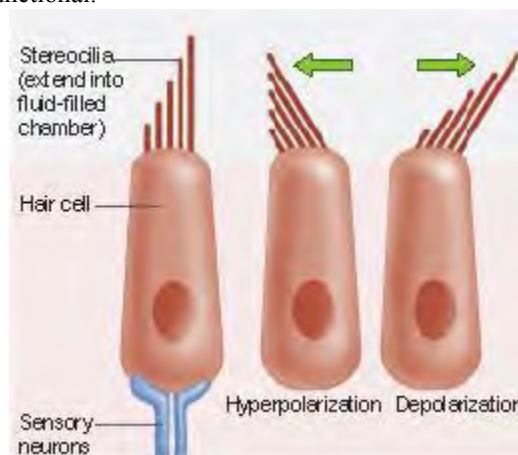


Figure 1: An image of an inner hair cell that may be replaced by the nanofiber.

Our approach will utilize piezoelectric Polyvinylidene Fluoride (PVDF) nanofibers. The nanofibers will deform due to sound wave stimuli, and transduce a current to auditory neurons. These nanofibers will replace natural inner hair cells. The stereocilia are fibers that resemble single strands of hair aligned in rows and stacked on the top of a hair cell. An image is provided in Figure 1. The stereocilia are an important part of the hair cells because their motion in the fluid of the inner ear is vital to how we naturally perceive sound. The stereocilia transduce an acoustic input into an electrical output. When the stereocilia bend they open ion channels into the hair cell which allow potassium and calcium ions into the cell body. This flow of ions is what mediates the hair cells' interaction with the auditory neuron. The neurons then communicate with the brain and provide the auditory information. It should be noted that frequency for sounds is inherently encoded by the varying lengths of the stereocilia that exist within the cochlea.

Our approach replaces the whole hair cell with a fiber or group of fibers that are piezoelectric. Piezoelectricity is a property of materials that relates to how mechanical deformations lead to the generation of an electric charge separation. The reverse is also true and is deemed the reverse piezoelectric effect. We expect to use this property to convert the movements of the fiber into an electric current to stimulate the auditory neuron.

II. BACKGROUND

PVDF normally exists in the alpha phase which is not piezoelectric. In order to create fibers that are piezoelectric, the fibers must be grown or transformed into the beta phase. Electrospinning will convert PVDF stored as a powder into a fiber. The fibers may also become self-poled by the electrospinning process. Self-poled PVDF will be piezoelectric. This work is concerned with specifically conventional electrospinning. Electrospinning, as a fiber or mat fabrication technique, has been described in various ways in recent literature. Bhardwaj and Kundu [1] provide a review of recent work with electrospinning and outline the significance of electrospinning parameters. Electrospinning creates micro or nanometer scale solid fibers from a liquid solution. For many relevant applications the solution is made from a polymer dissolved in a solvent. The end goal is to obtain a fiber of the polymer without retaining the solvent. This process is accomplished by providing a solution in a syringe and ejecting the solution from a needle while simultaneously applying a large voltage to the needle.

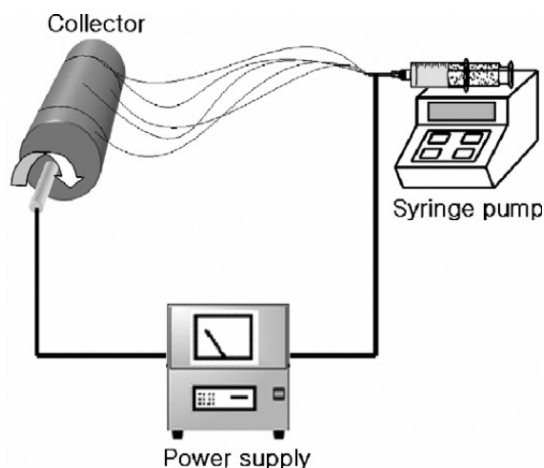


Figure 2a: Basic schematic diagram of electrospinning..

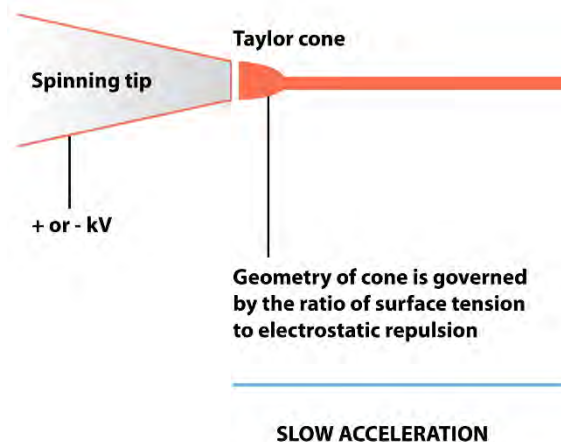


Figure 2b: Illustration of Taylor cone at the tip of a needle

A collector surface is used to obtain the fibers after the solution is subjected to a high voltage generally of the order of 10 kilovolts. Figure 2a displays a schematic of the system. The choice of collector shape and whether or not it rotates are parameters that affect the morphology of the electrospun fibers. For applications where small diameter size for fibers is desirable, a rotating cylinder is often employed to allow for some additional stretching. Rotating collectors may also produce aligned fibers rather than randomly deposited fibers. The key feature of electrospinning is the Taylor cone. If we imagine a drop of solution at the tip of a needle, the liquid will be pulled in the direction of the collector and a small jet of liquid will be constantly pulled from the solution. The initiation of this jet is dependent on the Taylor cone, which is depicted in Figure 2b. The Taylor cone itself is formed by interactions between the electrostatic forces acting on the solution and the surface tension of the solution. Charges on the liquid's surface repel each other and act against the surface tension of the solution. When a large enough voltage is applied, the electrostatic repulsions are strong enough to cause the Taylor cone to form and a charged jet of the polymer to be discharged. This jet directs the solution in the direction of a lower voltage source. Generally a grounded collector is used in tandem with a high voltage supply. While the solution is charged and moving towards the collector the solvent evaporates quickly depositing the solid polymer. The motion of induced dipoles in the non-homogeneous electric field may also affect the deposition. The electrospinning process has various parameters that may be altered. These are placed in broader categories. Namely, solution, processing and ambient parameters.

The present application will require fibers that range in diameter from 50-100 nanometers. This size requirement is based on the need for self-poled fibers. The phase of the PVDF will also be converted to the beta phase from the alpha phase. These self-poled fibers will be piezoelectric. The size requirement is a major factor in determining the parameters for the spinning process. One challenge that will complicate

this work is the need to include fluorophores into the polymer solutions. This will aid in a demonstration where the fibers are implanted within test mice. The fluorophore will act as a method to track the location of these fibers to ensure their successful delivery into the inner ear. The progress of the fibers inside a mouse's inner ear will be checked inside an in vivo molecular imager made by Bruker. The fluorophore is excited by a specific wavelength and will re-emit light when stimulated by that wavelength.

III. EXPERIMENTAL SETUP

IV. 3 Experimental Details:

For this project, PVDF with a molecular weight of 534,000 was purchased from Sigma-Aldrich. The solvents used include N, N- dimethylformamide (DMF, D4551), acetone (534064) and chloroform (C2432) from Sigma-Aldrich as well as reagent grade toluene from Fisher Science Education (S25611). The fluorophores tested were F8BT and MDMO-PPV both purchased from Sigma-Aldrich. The diameter of PVDF fibers was measured in a Jeol 7500F high resolution scanning electron microscope (HRSEM). The microtome used was a Leica RM2125 rotary microtome.

The preparation of nanofibers was accomplished with conventional electrospinning. Our electrospinning setup was slightly modified from the aforementioned system by the addition of a stepper motor which moved the syringe pump during the spinning process. The syringe pump had a horizontal translational motion that spread the fibers across a wider area of the collection cylinder. The rotating cylinder collector was always covered by a sheet of aluminum foil to act as a substrate for the deposited fibers.

A few different solutions were prepared in order to test if they could be electrospun and to determine the associated average diameter for the fibers. The solutions that were most thoroughly examined were solutions made from 18 weight percent (wt. %) PVDF dissolved in DMF and Acetone in a 3:1 volume to volume ratio with the inclusion of F8BT as well as, 16 wt. % PVDF dissolved in DMF. When preparing the solutions, PVDF was always added to a vial first, then DMF was added followed by the acetone if it was needed. This procedure was chosen to help limit the evaporation of acetone. In order to incorporate the fluorophore into the polymer solution it was dissolved in one of the solvents. This was accomplished by dissolving a small amount of F8BT in chloroform then putting that solution in a mixture with acetone.

Both solutions were placed on a hot plate around 50°C and set to stir before being used to electrospin. The PVDF and DMF samples stirred for an hour to allow for the PVDF to fully dissolve and a homogenous solution to be obtained. The solutions with acetone were left stirring overnight before being used for electrospinning.

Samples of 18 wt. % PVDF dissolved in DMF and acetone with F8BT were electrospun with a needle-to-collector distance of 10 centimeters, at 13 kilovolts, with a solution flow rate of 0.5 milliliters per hour. Samples of 16 wt. %

PVDF dissolved in DMF were spun at 15 centimeters, at 15 kilovolts, with a solution flow rate of 0.70 milliliters per hour.

The diameter of electrospun samples was investigated through the use of scanning electron microscopy (SEM). Only samples that seemed to form a stable or periodic jet were investigated by SEM. Samples that electrospayed or drew droplets from the solution instead of a jet were not pursued. The samples were characterized either as a mat deposited on aluminum foil or as fibers drop cast onto a stainless steel puck.

V. EXPERIMENTAL RESULTS

Figures 3 and 4 are SEM images for the 18 wt. % solution with the fluorophore and the 16 wt. % PVDF solution respectively. Several images of both samples were captured in order to measure the diameter of fibers present. Data for the fiber diameter measurements from each sample are provided in Figure 5.

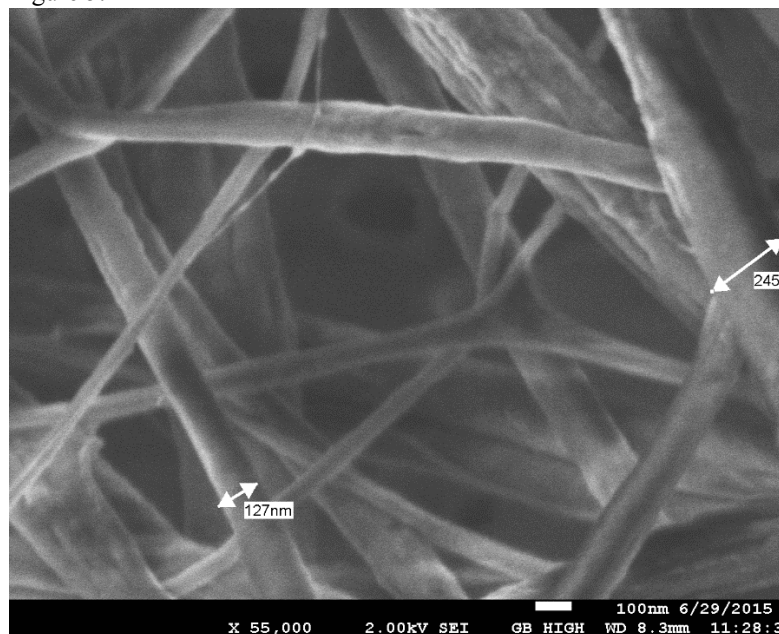


Figure 3 shows the 18 wt. % DMF and acetone solution with F8BT.

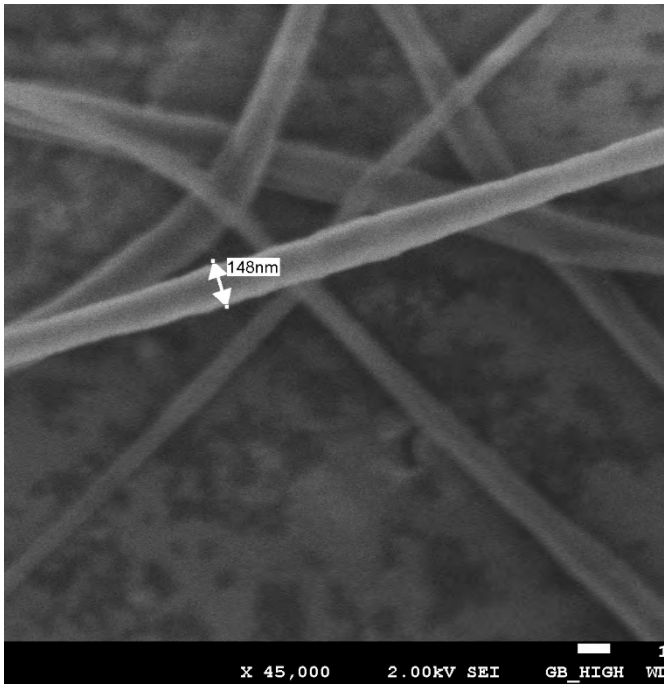


Figure 4 depicts the 16 wt. % PVDF in DMF.

Distribution of Fiber Diameter 16% PVDF DMF

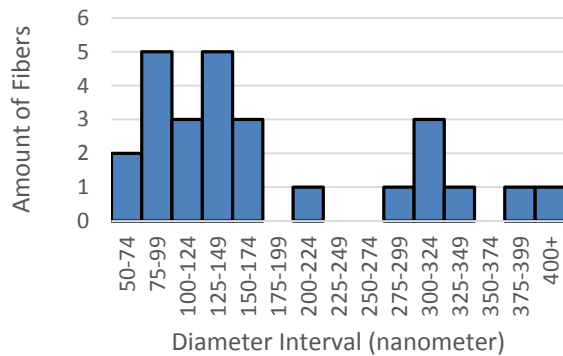


Figure 5a: is a histogram of the frequency of different diameters for the PVDF dissolved in only DMF.

Distribution of Fiber Diameter 18% PVDF, 3:1 DMF:Acetone, F8BT in Acetone

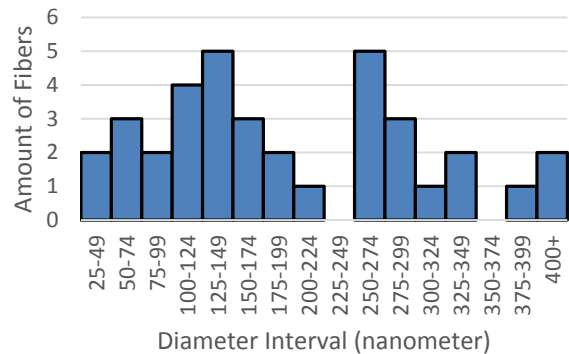


Figure 5b is a histogram of the frequency of different diameters for fibers with F8BT.

Average diameters and standard deviations measured were 200 nm for the diameter and 110 nm for the standard deviation of the solution with the fluorophore. The solution of 16 wt. % PVDF and DMF had an average diameter of 180 nm, and a standard deviation of 118 nm. The previous values were obtained through measurements of fibers present in SEM images. Three pictures of different locations were taken for each solution. We expect that the electrospinning process should generate a log-normal distribution in terms of the diameters of the fibers.

VI. DISCUSSION AND CONCLUSION

The wide distribution of sizes for the nanofibers is an issue that will reduce the yield of the electrospinning process. One factor encouraging such a large distribution is the inconsistent nature of the polymer jets being formed. The jet should form from a drop of the solution and stay consistent in the direction it points, the length of the jet and flow rate of the jet. However, while spinning these solutions the jet would change in periodic fashions. For the fluorophore sample this would include behavior where the jet appears and then grows larger as more of the solution is pulled in an instant and then the jet shrinks back down to its original size. One problem unique to the fluorophore enhanced samples was the requirement of adding trace amounts of chloroform to dissolve the fluorophore. The poor mixing between chloroform, acetone and DMF may have led to the aforementioned problem with the consistency of electrospinning. The PVDF and DMF sample had a different problem. For those samples the jet would change direction and length constantly during the process but would seem to be spinning a steady amount of the solution at any time.

The average diameters presented were too high for our desired application but there are some options to shrink the diameter in future studies. One choice is to increase the rotational speed of the collector. At present the collector rotated at about 140 rotations per minute. Other papers that

looked into similar solutions used 550 rotations per minute for their electrospinning. It should be noted that the size of the collector is also important when it comes to considering the rotational speed needed. Modifying the applied voltage, needle-to-collector distance and solvent choice are also options that may shrink the diameter.

ACKNOWLEDGMENT

The authors would like to acknowledge the support of the National Science Foundation, through NSF REU grant no. 1062672.

REFERENCES

- [1] Nidcd.nih.gov, 'Hearing Aids [NIDCD Health Information]', 2014. [Online]. Available: http://www.nidcd.nih.gov/health/hearing/pages/hearingaid.aspx#hearingaid_05. [Accessed: 05- Jun- 2015].
- [2] Nidcd.nih.gov, 'Cochlear Implants', 2014. [Online]. Available: <http://www.nidcd.nih.gov/health/hearing/pages/coch.aspx>. [Accessed: 05- Jun- 2015].
- [3] N. Bhardwaj and S. Kundu (2010), Electrospinning: A fascinating fiber fabrication technique, *Biotechnology Advances*, vol. 28, no. 3, pp. 325-347.
- [4] Prentice Hall, Inc., Stereocilia Polarization. 2003. Available: http://wps.prenhall.com/wps/media/objects/489/500888/images/FG43_04.JPG
- [5] Young-Seak Lee and Ji Sun Im (2010). Preparation of Functionalized Nanofibers and Their Applications, Nanofibers, Ashok Kumar (Ed.), ISBN: 978-953-7619-86-2, InTech, DOI: 10.5772/8150. Available from: <http://www.intechopen.com/books/nanofibers/preparation-of-functionalized-nanofibers-and-their-applications>
- [6] Wu Aik Yee, Masaya Kotaki, Ye Liu, Xuehong Lu (2007 January), Morphology, polymorphism behavior and molecular orientation of electrospun poly(vinylidene fluoride) fibers, *Polymer, Volume 48(Issue 2)*, Pages 512-521, ISSN0032-3861, <http://dx.doi.org/10.1016/j.polymer.2006.11.036>. (<http://www.sciencedirect.com/science/article/pii/S0032386106012924>)
- [7] Wu Aik Yee, Anh Chien Nguyen, Pooi See Lee, Masaya Kotaki, Ye Liu, Boon Teoh Tan, Subodh Mhaisalkar, Xuehong Lu (2008 September), Stress-induced structural changes in electrospun polyvinylidene difluoride nanofibers collected using a modified rotating disk, *Polymer, Volume 49 (Issue 19)*, Pages 4196-4203, ISSN 0032-3861, <http://dx.doi.org/10.1016/j.polymer.2008.07.032>. (<http://www.sciencedirect.com/science/article/pii/S0032386108006150>)
- [8] Kai Wei, Han-Ki Kim, Naotaka Kimura, Hiroaki Suzuki, Hidekazu Satou, Ki-Hoon Lee, Young-Hwan Park, and Ick-Soo Kim (2013 April), Effects of Organic Solvent and Solution Temperature on Electrospun Polyvinylidene Fluoride Nanofibers, *J Nanosci Nanotechnol*. 13(4):2708-13
- [9] Ankit R. Chaudhary, Dr. B. B. Ahuja, "Characterization and Optimization of Electrospun Polyacrylonitrile (PAN) and Polyvinylidene Fluoride (PVDF) Nanofibers", *5th International & 26th All India Manufacturing Technology, Design and Research Conference (AIMTDR 2014)* IIT Guwahati, Assam, India, December 12th–14th, 2014
- [10] E. Zussman, D. Rittel, and A. L. Yarin, Failure modes of electrospun nanofibers (*June 2003*), *Applied Physics Letters Volume 82, Number 22*
- [11] Raymond J. López-Hallman, Porscha Baines (August 2014), Electrospinning Process with a Moving Platform and PVDF as a Piezoelectric Transducer, Unpublished.